Doklady Physics, Vol. 49, No. 3, 2004, pp. 139–142. Translated from Doklady Akademii Nauk, Vol. 395, No. 1, 2004, pp. 36–39.

PHYSICS

Properties of the Representation of the Fokker–Planck Equation in the Basis of Hermite Functions

P. A. Zakharchenko and E. V. Radkevich

Presented by Academician A.M. Dykhne July 17, 2003

Received September 11, 2003

INTRODUCTION

An analysis of the asymptotic stability of the solutions to the Cauchy problem for the system of the Grad moments of the Fokker–Planck master equation [1–3], i.e., the system of partial differential equations with constant coefficients

$$L\left(\frac{\partial}{\partial t}, \frac{\partial}{\partial x}, B\right)M(t, x) := I\frac{\partial M(t, x)}{\partial t} + \sum A^{(j)}\frac{\partial M(t, x)}{\partial x} + BS_G M(t, x) = 0$$

leads to the problem of stability of polynomial bundles of the order (m, N) [4–8] of their dispersion equations

$$\mathcal{P}(\tau, \xi) - i\mathcal{Q}(\tau, \xi) = 0,$$

$$\mathcal{P}(\tau, \xi) = P_0(\tau, \xi) + \sum_{j \geq 1,\, N \geq 2j} (-1)^j \gamma_{2j} P_{2j}(\tau, \xi), \quad (1)$$

$$\mathcal{Q}(\tau, \xi) = \gamma_1 P_1(\tau, \xi) + \sum_{j \geq 1,\, N \geq 2j+1} (-1)^j \gamma_{2j+1} P_{2j+1}(\tau, \xi).$$

Here, $P_j(\tau, \xi)$ are homogeneous polynomials of the order $m - j$ with the leading coefficients in τ equal to unity; $x = (x_1, x_2, \ldots, x_n) \in R^n$, $\frac{\partial}{\partial x} = \left(\frac{\partial}{\partial x_1}, \frac{\partial}{\partial x_2}, \ldots, \frac{\partial}{\partial x_n}\right)$, $S_G, A^{(1)}, A^{(2)}, \ldots, A^{(n)}$ are real $m \times m$ matrices; I is the identity $m \times m$ matrix, and B is a large parameter.

If a vector function $M(t, x)$ is a solution to the system, then its arbitrary component $m_\alpha(t, x)$ is a solution to the scalar equation

$$R\left(\frac{\partial}{\partial t}, \frac{\partial}{\partial x}, B\right)m_\alpha(t, x) := \det\left(L\left(\frac{\partial}{\partial t}, \frac{\partial}{\partial x}, B\right)\right)m_\alpha(t, x) = 0. \quad (2)$$

Thus, analysis of the asymptotic stability of the Cauchy problem for the system $L\left(\frac{\partial}{\partial t}, \frac{\partial}{\partial x}, B\right)$ is reduced to the analogous problem for the scalar operator $R\left(\frac{\partial}{\partial t}, \frac{\partial}{\partial x}, B\right)$. It is well known that an arbitrary solution to a scalar equation can be represented in the form of the Fourier integral

$$(2\pi)^{-\frac{n}{e}} \int_{R^n} \hat{u}(t, \xi, B)\exp(i(\xi x + \tau(\xi, B)t))d\xi,$$

where $\tau = \tau(\xi, B)$ is a root of dispersion equation (1) of the form

$$\mathcal{R}(\tau, \xi, B) := i^{-m}R(i\tau, i\xi, B) = R(\tau, \xi, -iB) = 0.$$

The polynomial bundle (1) is called stable if all its roots lie in the open upper half-plane of the complex plane, i.e.,

$$\mathcal{R}(\tau, \xi, B) \neq 0, \quad \mathrm{Im}\,\tau \leq 0, \quad |\tau| + |\xi| > 0. \quad (3)$$

Stability condition (3) is equivalent to the asymptotic stability of the Cauchy problem for the original system.

POLYNOMIAL BUNDLES OF THE GRAD MOMENT SYSTEM

Analysis of polynomial bundles (1) of the dispersion equations of the Grad moment systems for the Boltzmann equation [4–7] and Fokker–Planck master equations [8] has shown that their structures are

Moscow State University,
Vorob'evy gory, Moscow, 119899 Russia
e-mail: hekex@mail.ru; evrad@land.ru

1028-3358/04/4903-0139$26.00

extremely rigid, namely, the constants γ_j satisfy the Routh–Hurwitz conditions [9] and the homogeneous polynomials $P_j(\tau, \xi)$ are hyperbolic in τ, the roots of successive polynomials not strictly separating each other.

PROBLEMS

Even in the preliminary analysis of the dispersion equations for the Grad moment systems, we meet the following problems.

What is the reason for the reproduction at each step of the Grad moment method of a sequence of hyperbolic homogeneous polynomials of the dispersion equation with the roots of successive polynomials not strictly separating each other?

How do the imaginary parts of the roots $\omega_j^N(\xi) = \mathrm{Im}\,\tau_j(\xi)$ vary as $N \to \infty$ and j is fixed? How do the minima of the imaginary parts of the so-called boundary-layer roots ($\mathrm{Im}\,\tau_j(\xi) = O(1)$ as $\xi \to 0$) responsible for the rate at which nonequilibrium variables approach the equilibrium state vary as the number of equations in the moment system $N \to \infty$?

For an arbitrary N, the following statements are true.

Lemma 1. *Let the highest-order polynomial P_0 of bundle* (1) *have real, constant-multiplicity roots, and the matrix $\sum_{j=1}^{d} \xi A_j$ of the original system have only first-degree primary divisors* (*these are the conditions of the Petrovskiĭ theorem* [10] *on the reduction of a matrix to the canonical form*). *The relaxation matrix $\mathcal{B}_N = -\mathcal{S}_N$ is diagonal; here, $\mathcal{S}_N$ is the diagonal representation matrix of the collision operator in the basis of the first N Hermite functions. Its diagonal coefficients are the following*:

$$b_{jj} = 0, \quad j = 1, 2, \ldots, N_b,$$
$$b_{jj} > 0, \quad j = N_b + 1, \ldots, N.$$

Here, N_b is the number of the base equilibrium variables. Then, we have the following.

The polynomials P_0 and P_1 of polynomial bundle (1) *of the dispersion equation of the Grad moment system constitute a regular hyperbolic polynomial pair; i.e., they are hyperbolic, have common roots, the multiplicity of which is smaller by one for P_1, and do not strictly separate each other.*

The polynomial P_N, where $N = m - N_b$, is strictly hyperbolic, the polynomials P_{N-1} and P_N of polynomial bundle (1) *constitute a strictly hyperbolic polynomial pair, i.e., they are strictly hyperbolic, and their roots strictly separate each other.*

If the polynomial P_N is not strictly hyperbolic, then the polynomials P_{N-1} and P_N form a regular, not strictly hyperbolic pair. In this case, all the polynomials P_j, $j = 0, 1, \ldots, N$, of the sequence have a common real root.

EXAMPLE

In the two-dimensional case ($n = 2$), using the Grad method for the first six moments, we seek the approximation of the solution to the Fokker–Planck master equation

$$(\partial_t + c_k\partial_{x_k}) f(t, x, c) = \partial_{c_k}(c_k + \partial_{c_k}) f(t, x, c)$$

over first six Hermite functions in the form

$$f_2(x, t, c) = m_0(x, t)\Psi_0(c) + m_{10}(x, t)\Psi_{10}(c) + m_{01}(x, t)\Psi_{01}(c) + \frac{1}{2}m_{20}(x, t)\Psi_{20}(c) + m_{11}(x, t)\Psi_{11}(c) + \frac{1}{2}m_{02}(x, t)\Psi_{02}(c), \qquad (4)$$

where $\Psi_\alpha(c)$ are the Hermite functions [9].

As a result, we obtain a system of six equations with constant coefficients

$$(E\partial_t + \partial_{x_1}A_1 + \partial_{x_2}A_2 + B)M_6(x, t) = 0, \qquad (5)$$
$$M_6 = (m_0, m_{10}, m_{01}, m_{20}, m_{11}, m_{02})^T$$

for the first six moments. Here, E is the identity matrix and

$$A_1 := \begin{bmatrix} 0&1&0&0&0&0 \\ 1&0&0&1&0&0 \\ 0&0&0&0&0&1 \\ 0&2&0&0&0&0 \\ 0&0&0&0&0&0 \\ 0&0&1&0&0&0 \end{bmatrix}, \quad A_2 := \begin{bmatrix} 0&0&1&0&0&0 \\ 0&0&0&0&0&1 \\ 1&0&0&0&1&0 \\ 0&0&0&0&0&0 \\ 0&0&2&0&0&0 \\ 0&1&0&0&0&0 \end{bmatrix},$$

$$B := \begin{bmatrix} 0&0&0&0&0&0 \\ 0&1&0&0&0&0 \\ 0&0&1&0&0&0 \\ 0&0&0&2&0&0 \\ 0&0&0&0&2&0 \\ 0&0&0&0&0&2 \end{bmatrix}, \quad E := \begin{bmatrix} 1&0&0&0&0&0 \\ 0&1&0&0&0&0 \\ 0&0&1&0&0&0 \\ 0&0&0&1&0&0 \\ 0&0&0&0&1&0 \\ 0&0&0&0&0&1 \end{bmatrix}.$$

The solution of the plane-wave type

$$M_6 = R_6\exp(i(t\tau + \xi_1x_1 + \xi_2x_2)),$$

where R_6 is a constant eigenvector, leads to the dispersion equation

$$\det(E\tau + \xi_1 A_1 + \xi_2 A_2 - iB)$$
$$= P_0 - \gamma_2 P_2 + \gamma_4 P_4 - i(\gamma_1 P_1 - \gamma_3 P_3 + \gamma_5 P_5),$$

$$\gamma_1 = 8, \quad \gamma_2 = 25, \quad \gamma_3 = 38, \quad \gamma_4 = 28, \quad \gamma_5 = 1,$$

$$P_0(\tau, \xi_1, \xi_2) = \tau^2(\tau^4 - 4(\xi_1^2 + \xi_2^2)\tau^2 + 3(\xi_2^2 + \xi_1^2)^2),$$

$$P_1(\tau, \xi_1, \xi_2) = \tau\left(\tau^4 - \frac{11}{4}(\xi_1^2 + \xi_2^2)\tau^2 + (\xi_2^2 + \xi_1^2)^2\right),$$

$$P_2(\tau, \xi_1, \xi_2) = \tau^4 - \frac{42}{25}(\xi_1^2 + \xi_2^2)\tau^2 + \frac{4}{25}(\xi_1^2 + \xi_2^2)^2,$$

$$P_3(\tau, \xi_1, \xi_2) = \tau\left(\tau^2 - \frac{16}{19}(\xi_1^2 + \xi_2^2)\right),$$

$$P_4(\tau, \xi_1, \xi_2) = \tau^2 - \frac{2}{7}(\xi_1^2 + \xi_2^2), \quad P_5 = \tau.$$

Thus, we have obtained a not strictly hyperbolic bundle of six polynomials; the polynomials P_j of the bundle are not strictly hyperbolic, and the roots of successive polynomials do not strictly separate each other:

$$[P_0, P_1](\tau, \xi) = \tau^2\left(\tau^8 - \frac{29}{4}\tau^6(\xi_1^2 + \xi_2^2)\right.$$
$$\left. + \frac{39}{4}\tau^4(\xi_1^2 + \xi_2^2)^2 - \frac{11}{4}\tau^2(\xi_1^2 + \xi_2^2)^3 + 3(\xi_1^2 + \xi_2^2)^4\right),$$

$$\min_{\tau^2 + |\xi|^2 = 1}\left(\tau^8 - \frac{29}{4}\tau^6(\xi_1^2 + \xi_2^2) + \frac{39}{4}\tau^4(\xi_1^2 + \xi_2^2)^2\right.$$
$$\left. - \frac{11}{4}\tau^2(\xi_1^2 + \xi_2^2)^3 + 3(\xi_1^2 + \xi_2^2)^4\right) = 0.63046179,$$

$$\min_{\tau^2 + |\xi|^2 = 1}[P_0, P_1] = 3, \quad \min_{\tau^2 + |\xi|^2 = 1}[P_1, P_2] = \frac{33}{20},$$

$$\min_{\tau^2 + |\xi|^2 = 1}[P_2, P_3] = \frac{581}{475}, \quad \min_{\tau^2 + |\xi|^2 = 1}[P_3, P_4] = \frac{163}{133},$$

$$\min_{\tau^2 + |\xi|^2 = 1}[P_4, P_5] = \frac{2}{7}.$$

ROUTH ALGORITHM FOR A PARAMETRIC BUNDLE

Definition of the Grad bundle. A polynomial bundle

$$\mathcal{P}(\tau, \xi) - i\mathcal{Q}(\tau, \xi) = 0,$$

$$\mathcal{P}(\tau, \xi) = \sum_{0 \le 2j \le N}(-1)^j \gamma_{2j} P_{2j}(\tau, \xi), \qquad (6)$$

$$\mathcal{Q}(\tau, \xi) = \sum_{0 \le 2j+1 \le N}(-1)^j \gamma_{2j+1} P_{2j+1}(\tau, \xi),$$

of the homogeneous polynomials P_j on the order of $m - j$ with real coefficients we call the connected bundle (or Grad bundle) on the order of (m, N) if

(i) the polynomials P_{2j}, $j \ge 0$ and P_{2j+1}, $j \ge 0$ are of the same evenness, i.e.,

$$P_{2j}(\tau, \xi) = \begin{cases} g_j(\tau^2, \xi), & (m - 2j) \text{ even} \\ \tau f_i(\tau^2, \xi), & (m - 2j) \text{ odd} \end{cases}$$

and

$$P_{2j+1}(\tau, \xi) = \begin{cases} g_j(\tau^2, \xi), & (m - 2j - 1) \text{ even} \\ \tau f_i(\tau^2, \xi), & (m - 2j - 1) \text{ odd;} \end{cases}$$

(ii) the Routh–Hurwitz rule holds for the coefficients γ_j;

(iii) the Poisson bracket is

$$[P_0, \partial_\tau(P_0)](\tau, \xi) \ge 0 \quad \forall(\tau, \xi) \in R^{d+1};$$

(iv) the Poisson brackets of successive polynomials are

$$[P_j, P_{j+1}](\tau, \xi) \ge 0 \quad \forall(\tau, \xi) \in R^{d+1},$$
$$j = 0, 1, \ldots, N - 1.$$

Thus, the polynomials P_j, $j = 0, 1, \ldots, N$ are not strictly hyperbolic and the roots of the successive polynomials P_j and P_{j+1} do not strictly separate each other.

We now demonstrate that properties (i)–(iv) of the Grad bundle make it possible to transfer the classical Routh procedure [10] to parametric bundles (6).

Lemma 2. *For an arbitrary homogeneous, strictly hyperbolic polynomial*

$$p(\tau, \xi) = \tau f(\tau^2, \xi)$$

on the order of $m = 2j + 1$ and for an arbitrary homogeneous hyperbolic polynomial

$$q(\tau, \xi) = g(\tau^2, \xi)$$

on the order of $2j$ whose roots do not strictly separate the roots $p(\tau, \xi)$,

$$[p, q](\tau, \xi) \ge 0, \quad (\tau, \xi) \ne 0$$

and such that, at any arbitrary point $\xi \in R^d$, the polynomial p is not a multiple of q, the following representation holds:

$$p(\tau, \xi) = \mu_{p,q}\tau q(\tau, \xi) - \gamma_{p,q}(\xi)b_{p,q}(\tau, \xi). \quad (7)$$

Here, $\gamma_{p,q}(\xi)$ is a positive homogeneous function of the second order, the constant $\mu_{p,q} = \frac{p_0}{q_0}$ is equal to the ratio of the leading coefficients of the polynomials p and q, and the function $b_{p,q}(\tau, \xi) \in \mathbb{C}\mathcal{P}_G^{2j-1}$ has the leading coefficient in τ equal to unity.

Representation (7) *is also valid for an arbitrary homogeneous, strictly hyperbolic polynomial*

$$p(\tau, \xi) = f(\tau^2, \xi)$$

on the order of $m = 2(j + 1)$ and for an arbitrary homogeneous hyperbolic polynomial

$$q(\tau, \xi) = \tau g(\tau^2, \xi)$$

on the order of $2j + 1$ whose roots do not strictly separate the roots of $p(\tau, \xi)$ if the polynomial p is a not multiple of q at an arbitrary point $\xi \in R^d$.

Theorem 1. *Grad bundle* (6) *satisfying the inequality*

$$[P_{N-1}, P_N](\tau, \xi) > 0 \quad \forall (\tau, \xi) \in R^{d+1}, \quad (\tau, \xi) \neq 0$$

is stable.

The basic stage in proving the theorem is the following lemma.

Lemma 3. *For an arbitrary Grad bundle, there exists an analogue of the Routh algorithm for constructing a family of positive continuous functions $\rho_j(\xi)$, $j = 1, 2, \ldots, m$ and the polynomials*

$$\pi_j(\tau, \xi) = \begin{cases} \sum_{k=0}^{[(m-j)/2]} a_{kj}(\xi)\tau^{2k}, & m - j \text{ even} \\ \tau \sum_{k=0}^{[(m-j-1)/2]} a_{kj}(\xi)\tau^{2k}, & m - j \text{ odd}, \end{cases}$$
$$j = 1, 2, \ldots, m,$$

with continuous coefficients such that

$$[\mathcal{P}, \mathcal{Q}](\tau, \xi) = \sum_{j=1}^{m} \rho_j(\xi)\pi_j^2(\tau, \xi).$$

CONCLUSIONS

Thus, we have succeeded in distinguishing a class of stable polynomial bundles that we call the Grad bundles. As was shown by direct calculations, these bundles are reproduced in the hierarchy of the Grad moment systems for the Boltzmann and Fokker–Planck master equations.

It was established that the second condition in the definition of the Grad bundle, namely, the fulfillment of the Routh–Hurwitz conditions for the leading coefficients of the bundle polynomials P_j, is a result of the dissipativity of the representation matrix for the collision operator in the basis of the Hermite function.

The second result of the dissipativity of the representation matrix for the collision operator in the basis of the Hermite function is the nonnegativity of the Poisson brackets for the limiting pairs of the successive polynomials of the dispersion equation bundle.

Still unsolved is the problem of reproduction of reasons for the nonnegativity of the Poisson brackets of all the pairs of successive polynomials in the bundle at each step of constructing the master equation approximation by the Grad moment system, which takes place in all the examples calculated by us.

REFERENCES

1. H. Grad, Commun. Pure Appl. Math. **2**, 23 (1949).
2. C. D. Levermore, J. Stat. Phys. **83**, 1021 (1996).
3. I. Muller and T. Ruggeri, *Extended Thermodynamics* (Springer, Berlin, 1993), p. 148.
4. L. R. Volevich and E. V. Radkevich, Differ. Uravneniya **39** (4), 1 (2003).
5. E. V. Radkevich, Contemp. Math., Fundam. Direct. **3**, 1 (2003).
6. P. A. Zakharchenko and E. V. Radkevich, Tr. Seminar im. I.G. Petrovskiĭ **24**, 12 (2003).
7. L. R. Volevich and E. V. Radkevich, Trudy MMO **64**, 15 (2003).
8. Ch. Hermite, *Oeuvres de Charles Hermite* (Gauthier-Villars, Paris, 1905), pp. 397–414.
9. S. K. Godunov, *Ordinary Differential Equations with Constant Coefficients* (Novosibirsk. Gos. Univ., Novosibirsk, 1994) [in Russian], p. 210.
10. I. G. Petrovskiĭ, *Selected Papers: Systems of Equations in Partial Derivatives, Algebraic Geometry* (Nauka, Moscow, 1986) [in Russian], pp. 152–154.

Translated by M. Lebedev

Doklady Physics, Vol. 49, No. 3, 2004, pp. 143–145. Translated from Doklady Akademii Nauk, Vol. 395, No. 1, 2004, pp. 40–42.

PHYSICS

On the Mechanism of the Breakdown of Complete Chaotic Synchronization

A. A. Koronovskiĭ*, Corresponding Member of the RAS D. I. Trubetskov, and A. E. Hramov*****

Received November 4, 2003

With the example of coupled Rössler systems, we consider the mechanism responsible for the breakdown of the complete chaotic synchronization of two coupled chaotic dynamical systems when varying the coupling parameter. A new method of introducing the phase of a chaotic signal is proposed on the basis of the continuous wavelet transform.

The phenomenon of synchronization of self-oscillatory systems often occurs in nature [1–3]. In recent years, researchers have placed particular emphasis on the chaotic synchronization of dynamical systems, including complete synchronization [4, 5], lag synchronization [6], global synchronization [7, 8], and phase synchronization [9, 10]. Complete synchronization implies that the states of interacting chaotic subsystems either coincide ($\mathbf{r}_1 = \mathbf{r}_2$) if these systems are identical or are close to each other ($|\mathbf{r}_1 - \mathbf{r}_2| \approx 0$) if the control parameters of the systems are slightly different. Phase synchronization means that the phase locking of chaotic signals $|m\phi_1 - n\phi_2| < \text{const}$ ($m, n \in \mathbb{R}$) is observed. The phase of a chaotic signal can be introduced in various ways [3, 10] with certain restrictions [3, 11]. The amplitudes of chaotic signals are uncorrelated in the phase synchronization mode.

In coupled slightly different chaotic oscillators, phase synchronization is observed even for weak coupling. For strong coupling, complete synchronization is realized. For intermediate coupling, lag synchronization is established when the states of two subsystems become nearly identical if one of them is shifted by a certain time lag τ: $\mathbf{r}_1(t) \approx \mathbf{r}_2(t - \tau)$. Thus, decreasing the coupling strength between two different chaotic systems, we can change complete synchronization to phase synchronization.

The purpose of this study is to reveal the mechanism responsible for the transition from one type of synchronization to another as the coupling strength between the chaotic subsystems increases (decreases). We investigate two different coupled Rössler systems:

$$\begin{aligned} \dot{x}_{1,2} &= -\omega_{1,2}y_{1,2} - z_{1,2} + \varepsilon(x_{2,1} - x_{1,2}), \\ \dot{y}_{1,2} &= \omega_{1,2}x_{1,2} + ay_{1,2}, \\ \dot{z}_{1,2} &= f + z_{1,2}(x_{1,2} - c). \end{aligned} \tag{1}$$

Here, the control parameters are chosen as $a = 0.165$, $f = 0.2$, and $c = 10$ by analogy with [6]. The control parameter $\omega_{1,2} = \omega_0 \pm \Delta$ specifies the slight difference between the subsystems under consideration ($\omega_0 = 0.97$ and $\Delta = 0.02$), and ε is the coupling parameter. For $\varepsilon = \varepsilon_p \simeq 0.036$, phase synchronization is established in the coupled Rössler systems. For $\varepsilon = \varepsilon_l \simeq 0.14$, the transition to lag synchronization takes place. If the coupling parameter ε increases further, the time shift τ tends to zero, which corresponds to complete synchronization [6].

Chaotic synchronization is usually studied by calculating the Lyapunov exponents, finding the phases of chaotic signals for every subsystem and the relation between them, determining similarity functions [6], etc. Although all these methods make it possible to determine the existence of a certain type of chaotic synchronization, they do not reveal the mechanism of its initiation and the change of one type of synchronization to another. In this study, we apply the continuous wavelet transform [12] for this purpose and, on its basis, introduce the family of chaotic-signal phases.

The continuous wavelet transform is represented by the convolution

$$W(s, t_0) = \int_{-\infty}^{+\infty} f(t)\psi^*_{s,t_0}(t)dt \tag{2}$$

where the asterisk denotes complex conjugation, $f(t)$ is the function under analysis, and the two-parameter wavelet function $\psi_{s,t_0}(t)$ is derived from the mother wavelet $\psi_0(t)$as

$$\psi_{s,t_0}(t) = \frac{1}{\sqrt{s}}\psi\left(\frac{t - t_0}{s}\right). \tag{3}$$

Saratov State University,
ul. Astrakhanskaya 83, Saratov, 410026 Russia
** e-mail: alkor@cas.ssu.runnet.ru*
*** e-mail: true@cas.ssu.runet.ru*
**** e-mail: aeh@cas.ssu.runet.ru*

1028-3358/04/4903-0143$26.00 © 2004 MAIK “Nauka/Interperiodica”

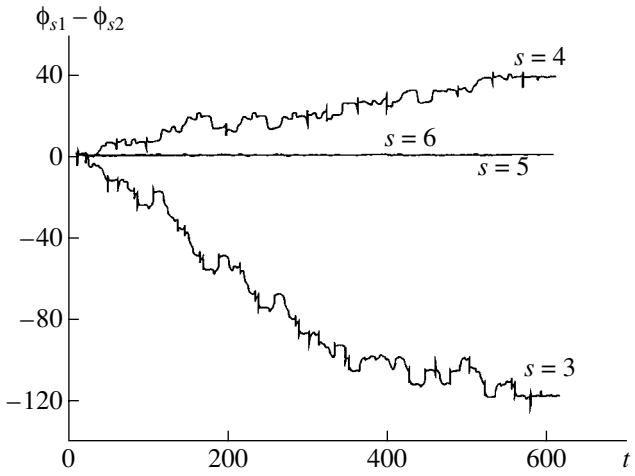

Time dependence of the phase difference $\phi_{s1} - \phi_{s2}$ for various time scales s. The time scales $s = 3$ and 4 are desynchronized, while the time scales $s = 5$ and 6, carrying a considerable part of the energy, are synchronized.

The width parameter $s \in \mathbb{R}^+$ is called the time scale of the wavelet transform, and t_0 is the shift parameter determining the position of the wavelet on the time axis t. We used the Morlet wavelet

$$\psi_0(\eta) = \frac{1}{\sqrt[4]{\pi}} \exp(j\omega_0\eta) \exp\left(\frac{-\eta^2}{2}\right) \qquad (4)$$

with the parameter $\omega_0 = 6$. For this wavelet parameter, the time scale s corresponds to the frequency component $f \simeq \frac{1}{s}$ in the Fourier spectrum of the time realization under analysis.

The complex function $W(s, t_0)$ determined by transform (2) characterizes the dynamics of the system for the time scale s at the current time t_0. The absolute value $|W(s, t_0)|$ characterizes the contribution of the given time scale s to the time realization of the system at the current time t_0. The Morlet wavelet conditionally represents the spectral components $f \simeq \frac{1}{s}$ in the Fourier spectrum at the time t_0 and its intensity [12].

Simultaneously, the phase $\phi_s(t_0) = \arg W(s, t_0)$ is naturally specified for each time scale s. The set of such phases forms the family of chaotic-signal phases. This approach enables us, first, to determine the phase dynamics of the system for all the time scales and, second, to avoid the difficulties [3, 11] arising in conventional methods of determining the phase (based on the Hilbert transform, the Poincaré section method, etc.).

Now, we consider variations in the wavelet surfaces $W_1(s, t)$ and $W_2(s, t)$ [obtained for the time realizations $y_1(t)$ and $y_2(t)$, respectively] with a decrease in the coupling parameter ε in system (1).

For large coupling parameters, the behaviors of both systems (1) are virtually identical ($\mathbf{r}_1 \approx \mathbf{r}_2$), which is evidence of complete synchronization.[1] Correspondingly, the wavelet surfaces for complete synchronization are also identical $\{W_1(s, t) \approx W_2(s, t)\}$. It is clear that the dynamics of phases is the same for all the time scales; i.e., $\phi_{s1}(t) \approx \phi_{s2}(t)$.

When the coupling parameter ε decreases and lag synchronization arises in the system, the time realizations created by dynamical systems (1) are shifted relative to each other by a time lag τ, which increases with a decrease in the coupling parameter ε. Since $\mathbf{r}_1(t - \tau) \approx \mathbf{r}_2(t)$ and due to the definition of wavelet transform (2), the wavelet surfaces $W_1(s, t)$ and $W_2(s, t)$ are related as $W_1(s, t - \tau) \approx W_2(s, t)$. Similarly, the phases are shifted relative to each other for all time scales s; i.e., $\phi_{s1}(t - \tau) \approx \phi_{s2}(t)$. In other words, phase locking takes place for each time scale in the lag-synchronization mode; i.e., all time scales remain synchronized in the coupled systems.

With the further decrease in the coupling parameter ε, the system passes from the lag-synchronization mode to the phase-synchronization mode. In this case, the scales s, whose role in the dynamics of the system is significant, are still synchronized; in other words, phase locking remains for these scales. At the same time, certain time scales ϕ_s go out of synchronization; i.e., the phase difference for these scales increases with time.

The figure shows the time dependence of the phase difference $\phi_{s1} - \phi_{s2}$ for various time scales s. The time scales $s = 5$ and 6 carry the greatest share of the wavelet spectral density $\int |W(s, t)|^2 dt$. As is seen in the figure, the dynamics of the phases $\phi_{1,2}$ is synchronous for these scales; i.e., phase locking is observed. At the same time, the time scales carrying a small share of the wavelet spectral density (figure shows the dependences for the time scales $s = 3$ and 4) are desynchronized, and the phase difference for these scales increases with time.

With the subsequent decrease in the coupling parameter ε, phase synchronization breaks down, and the systems pass into an asynchronous mode. In this mode, all time scales s behave asynchronously, and there is no phase locking for any of them.

Thus, the phenomenon of phase synchronization can be treated as follows. A certain part of the basic time (or frequency) scales of vibrations that carry the greatest share of energy are synchronized, whereas the remaining time scales (or frequencies) have already left the synchronization mode. Therefore, the dynamics of the systems is no longer completely synchronous, although the most important time scales are still synchronized.

[1] The vectors $\mathbf{r}_{1,2} = (x_{1,2}, y_{1,2}, z_{1,2})^T$ represent the states of first and second systems (1), respectively.

The chaotic-signal phase introduced in a certain way [3, 10] for phase synchronization is properly a phase corresponding to the fundamental frequency ω_0 in the Fourier spectrum of the signal. Therefore, phase locking and, correspondingly, phase synchronization are observed until the frequencies of vibrations carrying the greatest share of energy in the spectrum are synchronous. Furthermore, as was shown in [11], inappropriate introduction of the chaotic-signal phase for which the average frequency

$$\bar{\omega} = \left\langle \frac{d\phi(t)}{dt} \right\rangle \quad (5)$$

differs from the fundamental frequency ω_0 of the Fourier spectrum leads to incorrect results. In this connection, it is efficient and informative to analyze synchronization by using the wavelet transform and introducing a family of phases ϕ_s corresponding to various time scales s for a chaotic process.

ACKNOWLEDGMENTS

This work was supported by the Russian Foundation for Basic Research, the Council of the President of the Russian Federation for Support of Young Russian Scientists and Leading Scientific Schools, the Research and Education Center "Nonlinear Dynamics and Biophysics" at Saratov State University, and the US Civilian Research and Development Foundation for the Independent States of the Former Soviet Union (grant no. REC-006).

REFERENCES

1. I. I. Blekhman, *Synchronization in Nature and Engineering* (Nauka, Moscow, 1981).
2. V. S. Anshchenko, V. Astakhov, A. Neiman, *et al.*, *Nonlinear Dynamics of Chaotic and Stochastic Systems: Tutorial and Modern Developments* (Springer, Heidelberg, 2001).
3. A. Pikovsky, M. Rosenblum, and J. Kurths, *Synchronization: A Universal Concept in Nonlinear Sciences* (Cambridge Univ. Press, Cambridge, 2002; Tekhnosfera, Moscow, 2003).
4. L. M. Pecora and T. L. Carroll, Phys. Rev. A **44**, 2374 (1991).
5. K. Murali and M. Lakshmanan, Phys. Rev. E **48**, R1624 (1993).
6. M. G. Rosenblum, A. S. Pikovsky, and J. Kurths, Phys. Rev. Lett. **78**, 4193 (1997).
7. N. F. Rulkov, M. M. Sushchik, L. S. Tsimring, and H. D. I. Abarbanel, Phys. Rev. E **51**, 980 (1995).
8. H. D. I. Abarbanel, N. F. Rulkov, and M. Sushchik, Phys. Rev. E **53**, 4528 (1996).
9. M. G. Rosenblum, A. S. Pikovsky, and J. Kurths, Phys. Rev. Lett. **76**, 1804 (1996).
10. A. Pikovsky, M. Rosenblum, and J. Kurths, Int. J. Bifurcation Chaos Appl. Sci. Eng. **10**, 2291 (2000).
11. T. E. Vadivasova and V. S. Anishchenko, Radiotekh. Élektron. (Moscow), No. 1, 34 (2004).
12. A. A. Koronovskiĭ and A. E. Khramov, *Continuous Wavelet Analysis and Its Applications* (Fizmatlit, Moscow, 2003).

Translated by V. Bukhanov

Doklady Physics, Vol. 49, No. 3, 2004, pp. 146–149. Translated from Doklady Akademii Nauk, Vol. 395, No. 2, 2004, pp. 183–186.

PHYSICS

Hydrodynamics of a Metal Surface Melt under the Action of Laser Radiation: Observation of Regime Changes in the Real-Time Mode

Academician S. N. Bagaev*, V. G. Prokoshev, A. O. Kucherik**, D. V. Abramov**, S. M. Arakelyan**, and I. I. Klimovskiĭ*****

Received November 20, 2003

INTRODUCTION

The physics of interaction of intense optical radiation with various materials is determined by the contribution and competition of a number of nonlinear dynamic processes and phenomena (for example, of thermochemical and hydrodynamic nature), by phase transitions, etc. These processes and phenomena sequentially replace each other and are responsible for the energy and mass transport in a substance under the action of laser radiation (see e.g., [1]). The real-time diagnostics of these processes and determination of dynamic parameters for such an interaction on the basis of observation of dynamic patterns in the region of the laser action on a substance are extremely topical. First of all, this presents a unique possibility of investigating various fundamental regimes in physics of the condensed state of a substance. Second of all, this allows us to control the process of the appearance of such regimes.

However, it is necessary to take into account the presence of the erosion flame immediately above the interaction region, which screens the observation zone. By virtue of this fact, we are restricted to the consideration of only initial and final states (localized in time) of the surface subjected to irradiation. In this case, registration of dynamics of the surface change in the course of the melting process remains inaccessible.

In this work, the dynamic scan of the transition between these states is realized. This makes it possible to study intermediate states, which, in essence, determines the physics of the interaction of optical radiation with matter. In the case under consideration, the time and space resolutions attained correspond to characteristic scales of processes being developed. To this end, a laser image intensifier (laser monitor) is used in the detecting unit. The monitor plays the role of a narrow-band active filter for the probing beam reflected from the zone of the action of the monitor's self-radiation [2]. At the same time, the incoherent radiation of the erosion flame is virtually not amplified in this filter and does not manifest itself in the visualization of the interaction region. This allowed us to experimentally study the evolution of hydrodynamic instabilities arising in the melt zone under the action of laser radiation and to obtain the corresponding oscillation spectra. Based on the analysis of phase portraits revealed, we managed to determine factors governing the oscillation stochastization and to find scenarios of the development of hydrodynamic instabilities.

EXPERIMENTAL PROCEDURE

In this study, we used the radiation of a YAG:Nd^{3+} laser (with a wavelength of $\lambda = 1.06$ μm). The laser operated in the quasi-continuous mode (with a pulse duration of $\tau = 2.5$ ms and pulse repetition frequency of $f = 150$ Hz). In this case, the radiation power density on the metal sample surface (steel, lead, titanium, etc.) was equal to 3×10^5 W cm^{-2}. Such light intensities corresponded to the thermocapillary regime of exciting-laser-induced instabilities [1]. A copper vapor laser amplifier ($\lambda = 0.51$ μm, $\tau = 20$ ns, $f = 16$ kHz) was used as a monitor. The radiation of this laser, which was reflected from the action zone on the sample surface, played the role of the probing beam. Arising hydrodynamic regimes were detected by means of a CCD camera (with a high speed on the order of 20 ms) using the corresponding projection optics that ensured the spatial resolution of dynamic patterns at a level no worse than 10 μm. A personal computer further provided the data processing and pattern recognition in both on-line and off-line regimes. In the course of the experiment, the

* *NPO Astrofizika, Volokolamskoe sh. 11, Moscow, 125424 Russia*

** *Vladimir State University, ul. Gor'kogo 87, Vladimir, 600026 Russia*

*** *Institute of Thermal Physics of Extremal States, Joint Institute of High Temperatures, Russian Academy of Sciences, Izhorskaya ul. 13/19, Moscow, 127412 Russia*
e-mail: laser@vpti.vladimir.su; arak@vpti.vladimir.su; mvv@hedric.msk.su

1028-3358/04/4903-0146$26.00 © 2004 MAIK "Nauka/Interperiodica"

digitized luminance $J(t)$ for certain regions of dynamic patterns being observed in the reflected monitor light was measured. The degree of variation of the luminance (i.e., the magnitude) is proportional to the amplitude of oscillations of arising hydrodynamic instabilities. Details of the experimental procedure are given in [2].

THE EXPERIMENTAL RESULTS

Figures 1 and 2 show typical images of the melt zone on a metal surface, which were obtained with the laser monitor during the action of pumping radiation. These images periodically vary from the pattern corresponding to a regular state with complex wave struc-

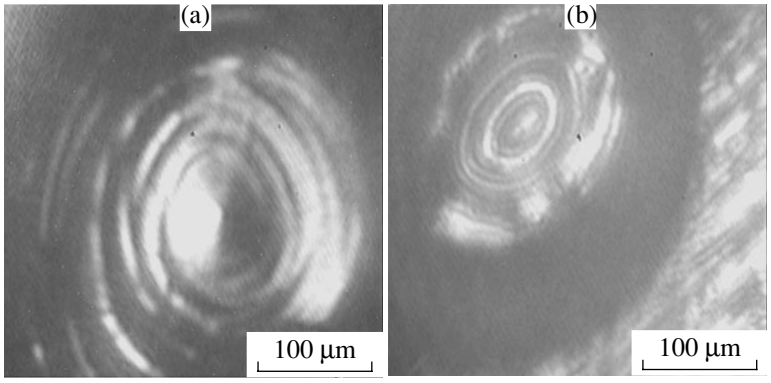

Fig. 1. Wave process arising under the laser action on the surface of melted metal: (a) lead and (b) titanium.

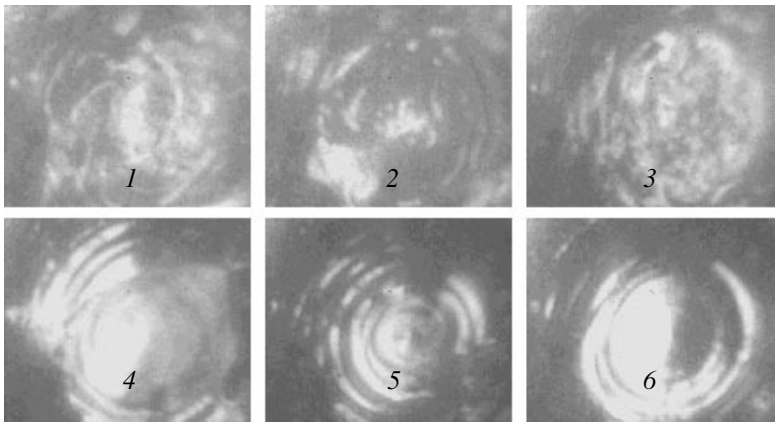

Fig. 2. Frames illustrating changes in regimes of lead melt flows under the action of laser radiation. As examples, 6 chosen frames out of a 25-frame episode of the melt dynamics evolution for the metal surface are presented. The 1st to 9th frames (illustrated by three characteristic images on frames *1*–*3*) correspond to the chaotic state of the lead surface melted by the laser radiation. Fragments of the melting process, which are presented on the 10th to 25th frames (see frames *4*–*6*), correspond to the ordered state with explicitly expressed surface waves.

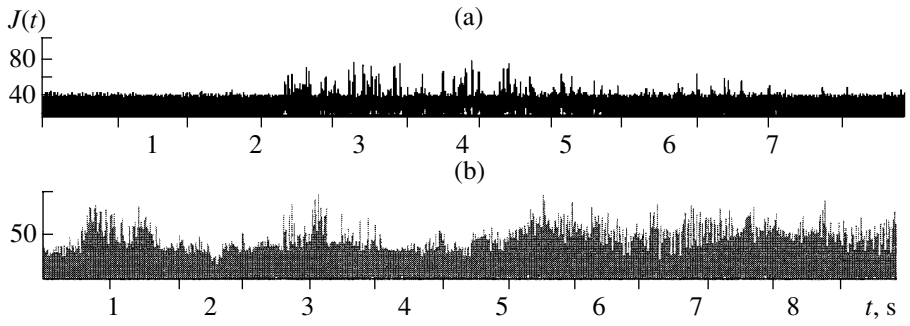

Fig. 3. Luminance $J(t)$ in the image center as a function of time: (a) steel and (b) lead.

Table

Experimental-run duration, s	Steel			Lead			Lorentz attractor (model)		
	D_L	D_m	ε	D_L	D_m	ε	D_L	D_m	ε
1	2.06	2.14	0.63	2.03	2.15	0.58			
4	2.34	2.27	0.77	2.63	2.36	0.87	2.30	2.35	0.85
8	2.40	2.34	0.83	2.68	2.48	0.96			

tures to that of their decay when the image has the form of a chaotic distribution of both light and dark spots (frame *3* in Fig. 2).

Figure 3 demonstrates the image luminance $J(t)$, which exhibits noticeable peaks and has the character of irregular oscillations.

ANALYSIS OF THE EXPERIMENTAL RESULTS AND THEIR DISCUSSION

Based on nonlinear-dynamics methods, we analyzed the time dependences obtained for the image luminance $J(t)$ in the course of the experiment. In accordance with these methods and using the one-dimensional realization of the observed physical quantity (Fig. 3; see, e.g., [3]), we can reconstruct the phase portrait of the entire system (Takens theorem). To this end, it is necessary to choose various realizations of the time process under study, which correspond to different time delays in the dependence obtained.

On the basis of this approach (the details of which are presented in [4]), we have analyzed the process observed of the development of hydrodynamic instabilities on the surface of a substance under the action of laser radiation. This analysis allows the character of the Fourier spectrum and phase portraits to be determined.

First of all, we have found that, initially, the oscillation spectrum is complicated with the development of an instability and then becomes quasi-continuous. Second of all, the phase portraits taken in the space of time-delay coordinates have the form typical for chaotic oscillations. Finally, parameters determining the oscillatory system being put in correspondence with the observed function $J(t)$ also acquire values intrinsic to a stochastic system.

In the latter case, the results of the analysis for three relevant parameters are given in the table. The first of them is the dimension (in the Lyapunov sense) $D_L = 2 + \frac{\lambda_+}{\lambda_-}$, where λ_+ and λ_- are sums of all positive and negative coefficients, respectively (this parameter makes it possible to find the general tendency of phase trajectories to the convergence or divergence). The second parameter is the mass dimension $D_M = \lim_{r \to 0} \frac{\ln M(r)}{\ln(1/r)}$, which characterizes the distribution $M(r)$ of phase-portrait points as a function of the distance r from the center of mass of the phase portrait. This parameter also allows the existence of anomalous densities in the phase-portrait structure to be determined, i.e., the degree of its disordering to be qualified. The third relevant parameter is the Shannon entropy $\varepsilon = \frac{1}{N}\sum_{i=1}^{N} p_i \ln p_i$, where the probability p_i of finding a point in a conditionally selected class of points of the one-dimensional realization was calculated for the number of classes $N = 16$.

Thus, it turns out to be possible to quantitatively classify the excitation of dynamic stochastic regimes in the case under consideration of laser initiation of hydrodynamic instabilities in the melt zone on the metal surface. Here, nonlinear spatial structures with a different degree of complexity arise, which appear and substitute each other with time. These structures can be aligned into a certain hierarchy of nonlinear transforms in the framework of fractal-geometry approaches on the basis of the comparison of topologically equivalent sets [5]. In this case, the change of a regime corresponds to sharp variation (discontinuity) of the corresponding dimension parameter.

CONCLUSIONS

In this paper, complex studies of nonlinear interactions of optical fields with a substance were carried out. These studies involve visualization of the laser-radiation action on the surface of a substance, as well as registration of dynamic spatial structures and instabilities being developed in this case. The observations were performed in the real-time mode, which is impossible in the case of a standard approach. The experimental method of the laser diagnostics in the real-time mode is based on the employment of a laser light amplifier for the optical image luminance. The mechanisms of the development and chaotization for such structures are investigated. Their quantitative characteristics and conditions for the appearance of the space-time chaos within the region of the laser action are determined. The goal of these studies consists in finding criteria responsible for the degree of ordering of energy- and mass-

transport processes and for their control and optimization. It was shown that the oscillation spectra, phase portraits, and controlling parameters of the processes under investigation are close to the corresponding characteristics of model hydrodynamic experiments aimed at the observation of stochastic regimes.

The study presented allows us to develop novel physical principles for controlling fundamental properties of surfaces of condensed media in the process of the action of a laser and to optimize this action. This is of particular importance in the case of the excitation of space-time instabilities, including those in problems of quantitative measurements of radiation resistance of various objects.

REFERENCES

1. N. V. Karlov and N. A. Kirichenko, *Vibrations, Waves, Structures* (Fizmatlit, Moscow, 2001) [in Russian].
2. V. G. Prokoshev, A. F. Galkin, I. I. Klimovskiĭ, *et al.*, Kvantovaya Élektron. (Moscow) **25**, 337 (1998).
3. M. I. Rabinovich and D. I. Trubetskov, *Introduction to Theory of Oscillations and Waves*, 2nd ed. (Nauka, Moscow, 1992). [Translated into English under the title: *Oscillations and Waves in Linear and Nonlinear Systems* (Kluwer, Dordrecht, 1989).]
4. P. S. Landa and M. G. Rozenblyum, Zh. Tekh. Fiz. **59** (1), 13 (1989) [Sov. Phys. Tech. Phys. **34**, 6 (1989)].
5. V. G. Prokoshev, D. V. Abramov, S. Yu. Danilov, *et al.*, Proc. SPIE **4429**, 96 (2001).

Translated by G. Merzon

Doklady Physics, Vol. 49, No. 3, 2004, pp. 150–153. Translated from Doklady Akademii Nauk, Vol. 395, No. 2, 2004, pp. 187–191.

PHYSICS

Experimental Corroboration of the Synthesis of Diamond in the Cavitation Process

Academician É. M. Galimov[1], A. M. Kudin[1], V. N. Skorobogatskiĭ[2], V. G. Plotnichenko[3], O. L. Bondarev[2], B. G. Zarubin[2], V. V. Strazdovskiĭ[2], A. S. Aronin[4], A. V. Fisenko[1], I. V. Bykov[1], and A. Yu. Barinov[2]

Received December 4, 2003

Thirty years ago, one of us (É.M.G.) theoretically justified the possibility of synthesizing diamonds in a cavitating fast fluid flow [1]. In that and more recent works [2, 3], variants of the cavitation synthesis of diamonds in nature were discussed. The essence of the idea is as follows. When a fluid rises rapidly from the mantle to the ground through a narrow channel–crack formed by it, sharp pressure differences arise. According to the Bernoulli equation, pressure in the fluid flow is inversely proportional to the velocity squared. Therefore, pressure decreases in a narrow spot, which gives rise to the appearance of gas bubbles. When the fluid again enters a wide place, pressure is recovered and bubbles collapse. Calculation shows that pressure can increase by several orders of magnitude. As was calculated in [1], pressure induced when bubbles filled with a carbon-containing gas collapse is sufficient for diamond synthesis. In [1, 2], it was assumed that the fluid contained CO_2, but a more recent analysis of diffusion velocities from the collapse medium showed that only hydrogen has a sufficiently high diffusion velocity. Therefore, a hydrocarbon substrate such as methane must be the initial substance.

In this work, we aim to reproduce the cavitation synthesis in experiments.

Benzene is used as the working substance. The saturated vapor of this low-viscous fluid has high pressure under normal conditions. In addition, it is characterized by a high carbon-to-hydrogen ratio (C_6H_6).

Figure 1 shows the layout of the experimental setup. It consists of (*1*, *4*) cavities, where a powder charge is ignited; movable plungers q_1 and q_2 joined to each other by a rod with a lock device, which makes it possible to uncouple the plunger q_2 when it reaches the extreme position; (*2*, *3*) cavities filled with the working substance (benzene); and a nozzle block in the form of a Venturi tube. The setup works as follows. The pressure of powder gases produced in cavity *1* induces motion of the plunger q_1 that displaces the fluid from cavity *2* into cavity *3* through the nozzle. The tensile stress arising in the narrowest cross section of the nozzle is responsible for the formation of vapor bubbles (first cavitation stage), which enter cavity *3*. When the plunger q_2 reaches the extreme right position (Fig. 1), the primer is struck and the powder charge in cavity *4* is ignited. Powder gases produced in cavity *4* displace the plunger q_2 in the opposite direction. This plunger increases the pressure in cavity *3* and provides the conditions for fast collapse of vapor bubbles.

Pressure in experiments was measured by piezoelectric transducers in cavities and nozzle. In methodical experiments (when powder in cavity *4* was not ignited), the velocities of plungers and rarefaction in cavity *3* were measured. Working pressures were in the range 120–150 MPa, rarefaction in cavity *3* was equal to about 0.02–0.04 MPa, and the velocities of the plungers q_1 and q_2 were equal to about 2 m/s. Measurement showed that the temperature of the fluid in cavity *3* virtually does not vary during the process. Therefore, the fluid can be treated as barotropic and isothermal in the following theoretical study.

The working regime in the experimental setup adequately simulates the second stage of the cavitation process, i.e., the cavitation collapse of bubbles that occurs in cavity *3* under the conditions corresponding

[1] *Vernadsky Institute of Geochemistry and Analytical Chemistry, Russian Academy of Sciences, ul. Kosygina 19, Moscow, 117975 Russia*
e-mail: galimov@geokhi.ru, bukov@geokhi.ru

[2] *Bauman State Technical University, Vtoraya Baumanskaya ul. 5, Moscow, 107005 Russia*
e-mail: m6bk@aport2000.ru

[3] *Fiber Optics Research Center, General Physics Institute, Russian Academy of Sciences, ul. Vavilova 38, Moscow, 117942 Russia*
e-mail: victor@fo.gpi.ac.ru

[4] *Institute of Solid State Physics, Russian Academy of Sciences, Chernogolovka, Moscow oblast, 142432 Russia*
e-mail: aronin@issp.ac.ru

1028-3358/04/4903-0150$26.00

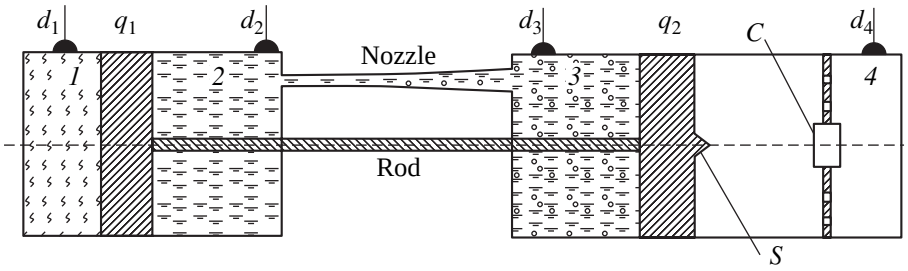

Fig. 1. Layout of the experimental setup: d_1–d_4 are pressure transducers, C is the primer, and S is the firing pin.

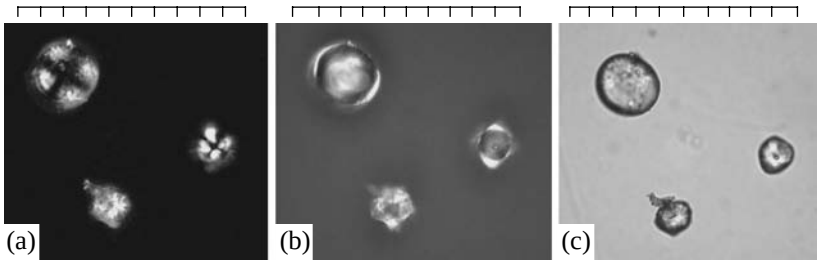

Fig. 2. Microscopic image of particles obtained in the cavitation experiment by using (a) crossed nicols, (b) reflected light, and (c) passing light. One scale division is equal to 1 μm.

to the recovery of pressure after the outflow of bubbles from the Venturi tube.

After the experiment, the fluid was poured out of the working cylinder. Suspended particles were precipitated by centrifugation, placed in a Petri dish, and studied under a microscope. A considerable part of the precipitated substance is a dark shapeless paste. However, this paste contained bright micron particles. In crossed nicols of the analyzer of the optical microscope, many of these particles provided a pronounced polarographic pattern in the form of a cross (Fig. 2). In reflected light, a noticeable brown inclusion was always observed in the central part of these particles. This inclusion is clearly seen in the far right particle in Fig. 2.

Sediment after centrifugation was analyzed with a PU 9804 Philips IR spectrometer. Two 0.75- and 1-mg samples were milled in a mechanical mill with 40 mg of KBr and pressed into tablets 10 mm in diameter. Spectra include frequencies corresponding to functional groups of organic compounds. Carbon in CH_2 groups is detected by asymmetric and symmetric valence vibrations at $\nu_{as} = 2921$ cm^{-1} and $\nu_s = 2851$ cm^{-1}, respectively, as well as by scission and pendulum vibrations at 1468 and 721 cm^{-1}, respectively. In addition to the absorption bands of organic compounds, the spectrum includes the lines $\nu = 2662$, 2510, 2170, and 2077 cm^{-1}, which can be treated as the bands of overtones and composite wavenumbers of longitudinal and transverse, optical and acoustic, vibrations of the diamond lattice. However, certain characteristic wavenumbers in the spectrum from cavitation-produced diamonds are higher than those from synthetic diamonds by several tens of inverse centimeters.

Organic compounds including polymeric compounds are naturally produced when cavitation is induced in benzene, and their presence is indirect evidence of the realization of the cavitation regime in the setup used in this work.

However, we are primarily interested in the nature of bright particles that are mentioned above and observed under the microscope. The substance precipitated from benzene was processed in hydrochloric acid at 80–218°C for ten hours for the removal of the organic component and was analyzed with a JEM-100CX scanning electron microscope. Table 1 presents data calculated from electron diffraction patterns for the samples under consideration in comparison with reference data for diamond and graphite. According to Table 1, the diamond phase is identified with a high probability in certain sections of particles being studied. In other sections, carbon is instead in the graphite phase.

Whole particles are an aggregate of nanocrystallites. The dimension of diamond crystals is equal to 10–30 nm. Figure 3 shows diffraction patterns from diamond particles, which also include an unidentified line (see table) that does not refer to the diamond phase. Certain ring reflections are split due to lattice distortion caused possibly by impurities. A number of aggregates provide the diffraction pattern shown in Fig. 3. The interplanar spacings calculated for this case correspond to graphite.

Individual particles were mechanically transported under the microscope to the sample table and analyzed

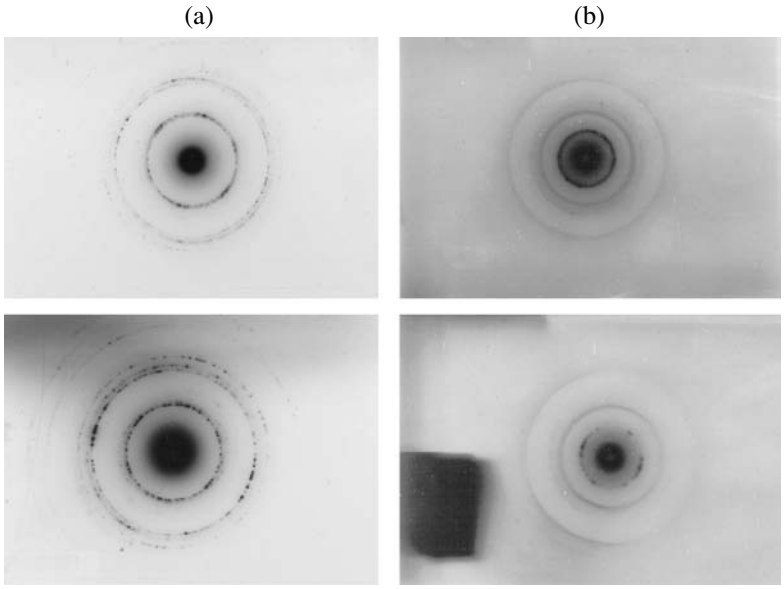

Fig. 3. Electron diffraction pattern (negative) of the structure of sections of cavitation-synthesized particles containing (a) the diamond phase and (b) predominantly graphite.

by Raman spectroscopy. Raman scattering spectra were detected with a T64000 triple spectrograph (Jobin Yvon firm) on a silicon photoreceiver (CCD matrix) cooled by liquid nitrogen. The Raman scattering spectrum was excited by a 5145-Å argon laser. Exciting radiation supplied on a sample through the microscope was focused on a spot with a diameter of about 2 μm and had a power of 10 mW. Although the spectrum of particles extracted from the products of cavitation processing of benzene included a line close to the characteristic 1330-cm^{-1} diamond line, this spectrum is more complicated and this line is broader. Figure 4 shows the typical Raman spectrum for particles synthesized in the experiment. It is known that the broadening of the Raman spectrum can be caused by both the small size of diamond clusters [4, 5] as was observed, e.g., in the Raman spectrum of a diamond film [6, 7] and the presence of nondiamond impurity (graphite, amorphous carbon, hydrocarbon formations). We note that some particles exploded when irradiated by a laser beam for a comparatively long time (100 s), which is probably associated with the presence of gas–liquid inclusions.

The Raman spectrum of a particle obtained in the cavitation experiment was compared to the Raman spectrum of a new carbon-containing formation synthesized in a high-pressure setup. The spectra were almost identical. Since a pressure of 70 kbar and a temperature of 1700°C in the high-pressure setup were in the region of the thermodynamic stability of diamond, the above new formation likely contained the diamond phase.

Diffraction data on the composition of particle agglomerates containing the diamond phase that are obtained in the cavitation experiment

Line no.	Experimental data				Reference data			
	d_{hkl}							
	sections with the diamond phase			sections without the diamond phase	diamond		graphite	
	6001995	6601997	6002000		*HKL*	d_{hkl}	*HKL*	d_{hkl}
1	2.08	2.08	2.08	3.37	111	2.06	002	3.38
2	1.25	1.25	1.25	2.12	220	1.26	100	2.12
3	1.16	1.16	1.16	1.69	–	–	004	1.69
4	1.07	1.07	1.08	1.23	311	1.08	110	1.227
5	–	–	–	1.12	331	0.82	006	1.12

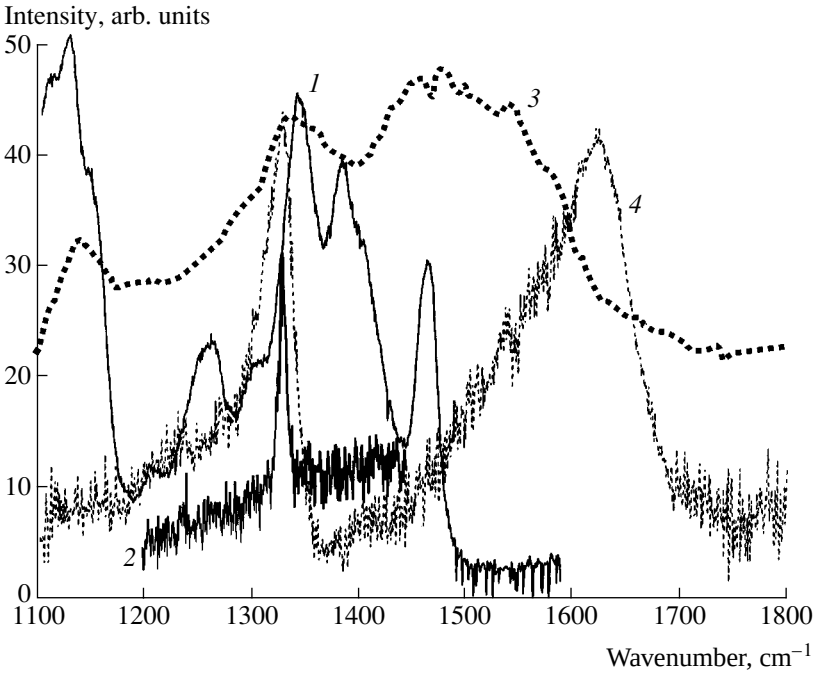

Fig. 4. Raman spectrum of the (*1*) experimental particle, (*2*) diamond crystal, (*3*) diamond film, and (*4*) explosion-produced microdiamonds. The particle under investigation was a 14-μm aggregate; exposition time is equal to 100 s. The spectra of the diamond film and explosion-produced microdiamonds are taken from [7] and [9], respectively. The excitation wavelength was equal to 632.8 nm.

However, the authors of [8] did not carry out studies corroborating this fact.

The conclusions of this work are as follows:

the excitation of cavitation in the working hydrocarbon fluid (benzene) is accompanied by the appearance of new formations that consist primarily of organic polymers and include solid carbon particles;

particles are aggregates of nanocrystalline structures;

at least some of such aggregates contain the diamond phase.

Thus, the possibility of synthesizing the diamond phase when exciting cavitation in a carbon-containing fluid has been experimentally corroborated.

ACKNOWLEDGMENTS

We are grateful to T.I. Abramyan, V.A. Alekseev, A.V. Ivanov, V.E. Kulikovskiĭ, B.A. Rudenko, and V.V. Koltashev for assistance at various stages of the work.

REFERENCES

1. E. M. Galimov, Nature (London) **243**, 389 (1973).
2. É. M. Galimov, Izv. Akad. Nauk SSSR, Geol., No. 1, 22 (1973).
3. É. M. Galimov, Geokhimiya **4**, 456 (1985).
4. J. Schwan, S. Ulrich, V. Batori, *et al.*, J. Appl. Phys. **80**, 440 (1996).
5. D. S. Knight and W. B. White, J. Mater. Res. **4**, 385 (1989).
6. A. A. Lyalin, A. V. Simakin, V. A. Bobyrev, *et al.*, Kvantovaya Élektron. (Moscow) **27** (1), 1 (1999).
7. J. Wagner, C. Wild, and P. Koidl, Appl. Phys. Lett. **59**, 779 (1991).
8. V. Yu. Litvin, Yu. A. Litvin, and A. A. Kadik, http://www.scgis.ru/russian/cp1251/h_dgggms/1-2003/informbul-1/term-3.pdf (Vestn. Otd. Nauk o Zemle Akad. Nauk, No. 1, 2003).
9. V. Yu. Dolmatov, Usp. Khim. **70**, 687 (2001).

Translated by R. Tyapaev

Doklady Physics, Vol. 49, No. 3, 2004, pp. 154–157. Translated from Doklady Akademii Nauk, Vol. 395, No. 3, 2004, pp. 326–329.

PHYSICS

SU(3) Polarization States in Quantum and Atomic Optics and High-Precision Measurements

Academician S. N. Bagaev*, A. P. Alodjants, and S. M. Arakelian****

Received November 20, 2003

The polarization of three-mode Bose systems having the Gell-Mann SU(3) symmetry is discussed. The concept of SU(3) polarization in the Hilbert space is proposed for a quantum system, and an original SU(3) interferometer that makes it possible to measure various Gell-Mann parameters for a light field is considered for the first time. Measurements of the signal-to-noise ratio that are limited only by quantum noise and based on the use of entangled photon states at the input of an optical system are analyzed. The possibility of the formation of a new type of quantum (helicity) states of light, where Hermitian quadratures are fundamentally correlated with polarization Stokes parameters, is shown in the classical-field approximation for one of the modes.

INTRODUCTION

Quantum states of light-field polarization are intensively investigated both theoretically and experimentally by a number of research groups [1–5]. Although practical applications of nonclassical polarization states in optics have already been widely discussed in connection with the problems of teleportation, quantum processing of information [1, 2], and high-precision measurements in ellipsometry [3–5], the nature of physical measurements and features of the formation of light characterized by a nonclassical polarization are not completely understood.

Stokes polarization parameters satisfying the SU(2) algebra are now commonly accepted as a universal description of quantum polarization states of the light field. Nonclassical states were described in terms of these quantities in many works, and the contribution of Russian researches to this field is decisive [3–7].

In this study, the quantum polarization properties are analyzed for three-mode light fields in the SU(3)-algebra representation, which is a standard approach in describing quantum phenomena in QCD and elementary particle physics [8]. A quantum parametric-interaction process, where one photon of the pumping wave decays into two, idler- and signal-wave, photons and energy transfer between all waves is taken into account, is an example of a three-mode optical system in nonlinear optics. The universal approach being considered, which is based on the second-quantization representation, can also be used to solve problems of atomic optics. First, we imply the quantum dynamics of three-level atomic systems [9] as well as the problem of interaction of atoms with a quantized external electromagnetic field [10].

SU(3) POLARIZATION QUANTUM STATES IN BOSE SYSTEMS

In the Schwinger representation, the quantum three-mode Bose system can be represented in terms of its Hermitian Gell-Mann operators of the SU(3) algebra λ_j, $j = 0, 1, \ldots, 8$ (cf. [8]):[1]

$$\lambda_0 = a_1^+ a_1 + a_2^+ a_2 + a_3^+ a_3; \tag{1a}$$

$$\lambda_1 = a_1^+ a_2 + a_2^+ a_1, \quad \lambda_2 = i(a_2^+ a_1 - a_1^+ a_2), \quad \lambda_3 = a_1^+ a_1 - a_2^+ a_2; \tag{1b}$$

$$\lambda_4 = a_1^+ a_3 + a_3^+ a_1, \quad \lambda_5 = i(a_3^+ a_1 - a_1^+ a_3); \tag{1c}$$

$$\lambda_6 = a_2^+ a_3 + a_3^+ a_2, \quad \lambda_7 = i(a_3^+ a_2 - a_2^+ a_3); \tag{1d}$$

$$\lambda_8 = \frac{1}{\sqrt{3}}(a_1^+ a_1 + a_2^+ a_2 - 2a_3^+ a_3), \tag{1e}$$

where $a_j (a_j^+)$ with $j = 1, 2$, and 3 are the photon creation (annihilation) operators. The operator λ_0 specified by Eq. (1a) determines the total number of photons in modes and commutes with the remaining operators

* *NPO Astrofizika, Volokolamskoe sh. 11, Moscow, 125424 Russia*

** *Vladimir State University, ul. Gor'kogo 87, Vladimir, 600000 Russia*

e-mail: laser@vpti.vladimir.su

[1] The introduction of the SU(N) symmetry group determining an $(N^2 - 1)$-dimensional vector field satisfying the requirements of invariance under local phase transformations is useful for describing the corresponding physical interaction.

1028-3358/04/4903-0154$26.00

specified by Eqs. (1b)–(1e). The noncommuting operators $\lambda_{1,2,3}$ in (1b) form an SU(2) subalgebra of the SU(3) algebra. In quantum optics, this subalgebra is an analogue of the polarization Stokes parameters $S_{1,2,3}$ of the light field, where modes 1 and 2 correspond to a linear (circular) polarization basis. The presence of the third mode a_3 implies, by analogy with elementary particle physics, the existence of the isospin (isospin polarization) of the light field.

Let us define the unit polarization vector **e** of the three-mode system as

$$\mathbf{e}a = \mathbf{e}_1 a_1 + \mathbf{e}_2 a_2 + \mathbf{e}_3 a_3, \quad (2)$$

where a is the annihilation operator of the three-mode field and $\mathbf{e}_j$ with $j = 1, 2$, and 3 are orthogonal vectors satisfying the condition

$$\sum_{j=1}^{3} |\mathbf{e}_j|^2 = 1. \quad (3)$$

Relation (2) is then represented in the form

$$a = e_1^* a_1 + e_2^* a_2 + e_3^* a_3, \quad (4)$$

where $e_j^* = \mathbf{e}^* \mathbf{e}_j$ are the projections of the polarization vector, which, within the SU(3) algebra, are specified by four phase parameters θ, ϕ, ψ_1, and ψ_2 (see [12]) as

$$e_1 = e^{i\psi_1}\sin\theta\cos\phi, \quad e_2 = e^{i\psi_2}\sin\theta\sin\phi, \quad e_3 = \cos\theta,$$
$$0 < \theta, \quad \phi \le \frac{\pi}{2}, \quad 0 \le \psi_{1,2} < 2\pi. \quad (5)$$

For the light field in a coherent state, we have

$$a|\alpha\rangle = \alpha|\alpha\rangle, \quad (6a)$$

$$a_j|\alpha_j\rangle = \alpha_j|\alpha_j\rangle, \quad (6b)$$

$$j = 1, 2, 3,$$

where $|\alpha\rangle = |\alpha_1\rangle|\alpha_2\rangle|\alpha_3\rangle$ is the coherent state of the three-mode field and $\alpha = \sum_{j=1}^{3} e_j^* \alpha_j$ is its eigenvalue; that is, $\alpha_j = e_j\alpha$, $j = 1, 2, 3$.

Effects of Bose–Einstein condensation in atomic optics are usually described by introducing atomic-coherent states, which, in the case of SU(3) symmetry, have the form

$$|\Psi\rangle_N = \frac{1}{\sqrt{N!}}(e_1 a_1^+ + e_2 a_2^+ + e_3 a_3^+)^N |0\rangle, \quad (7)$$

where $|0\rangle \equiv |0\rangle_1|0\rangle_2|0\rangle_3$ is the vacuum state and $N = \langle\lambda_0\rangle$ is the total mean number of particles.

Thus, expressions (4) and (5) specify the polarization state of the three-mode system in the Hilbert space. The isospin-polarization state corresponds to an "ordinary" polarization of a two-mode field. In this case, the phase parameters θ, ϕ, ψ_1, and ψ_2 can be related to the parameters of ellipticity and azimuth of the polarization, which are parameters measured in ellipsometry (see, e.g., [7]). However, the direct measurement procedure of the parameters θ, ϕ, ψ_1, and ψ_2, as well as the polarization degree of the light field, requires special analysis in the quantum case (see below).

SU(3) INTERFEROMETER

Let us consider the polarization degree P of the three-mode field and the degree of isospin polarization P_{IP}. These quantities can be expressed in terms of the expectation values of the operators λ specified by Eqs. (1) as

$$P = \frac{\sqrt{3}}{2}\frac{\left(\sum_{j=1}^{8}\langle\lambda_j\rangle^2\right)^{1/2}}{\langle\lambda_0\rangle}; \quad (8a)$$

$$P_{IP} = \frac{(\langle\lambda_1\rangle^2 + \langle\lambda_2\rangle^2 + \langle\lambda_3\rangle^2)^{1/2}}{\langle a_1^+ a_1\rangle + \langle a_2^+ a_2\rangle}. \quad (8b)$$

According to these expressions, $P = P_{IP} = 1$ for the field in coherent states (6) or (7).

Measurement of the quantities defined by Eqs. (8a) and (8b) and the quantum properties of an optical system having the SU(3) symmetry requires schemes and procedures other than those for the polarization characteristics of the SU(2) subalgebra [1–5, 7]. To this end, we propose the scheme of an SU(3) interferometer for simultaneous measurement of the Gell-Mann parameters (figure). The modes a_j, $j = 1, 2, 3$, are applied at the input of the interferometer, and the remaining modes V_j are vacuum ones. Detection provides measurement of the differences of the photon numbers at its output:

$$N_{12}^{(-)} = N_{21} - N_{12} = \frac{1}{2}\lambda_{12} + V_{12}; \quad (9a)$$

$$N_{13}^{(-)} = N_{31} - N_{13} = \frac{1}{2}\lambda_{13} + V_{13}; \quad (9b)$$

$$N_{23}^{(-)} = N_{32} - N_{23} = \frac{1}{2}\lambda_{23} + V_{23}, \quad (9c)$$

where $N_{ij} = d_{ij}^+ d_{ij}$ ($i, j = 1, 2, 3$) are the operators of the detected photon numbers and the normally ordered operators V_{ij} depend on the annihilation (creation) operators for the vacuum modes at the input of the interferometer. The measured Gell-Mann parameters λ_{ij} appearing in expressions (9a)–(9c) are represented in the form

$$\lambda_{12} = a_1^+ a_2 e^{i\phi_2} + a_2^+ a_1 e^{-i\phi_2}; \quad (10a)$$

$$\lambda_{13} = a_1^+ a_3 e^{-i\phi_1} + a_3^+ a_1 e^{i\phi_1}; \quad (10b)$$

$$\lambda_{23} = a_2^+ a_3 e^{i\phi_3} + a_3^+ a_2 e^{-i\phi_3}. \quad (10c)$$

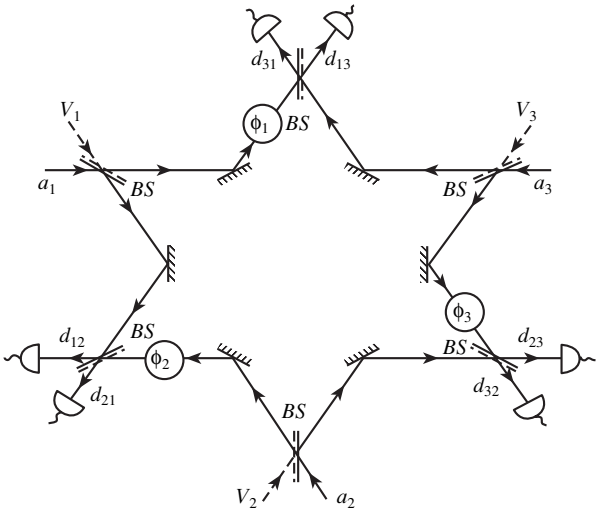

SU(3) interferometer for simultaneous measurement of the Gell-Mann parameters in optics. Quantum (a_j) and vacuum (V_j) modes ($j = 1, 2, 3$) are supplied to the input; ϕ_j are phase shifts in the interferometer arms due to linear optical elements; and *BS* are semitransparent beam splitters.

With the aid of expressions (9a)–(9c), the expectation values of the differences between photon numbers, $\langle N_{ij}^{(-)} \rangle$, are expressed as

$$\langle N_{12}^{(-)} \rangle = \frac{1}{2}\langle \lambda_{12} \rangle; \tag{11a}$$

$$\langle N_{13}^{(-)} \rangle = \frac{1}{2}\langle \lambda_{13} \rangle; \tag{11b}$$

$$\langle N_{23}^{(-)} \rangle = \frac{1}{2}\langle \lambda_{23} \rangle. \tag{11c}$$

Thus, for a certain phase difference ϕ_j in the interferometer arms, the Gell-Mann parameters $\lambda_{1,2}$, $\lambda_{4,5}$, and $\lambda_{6,7}$ [see (1b)–(1d)] can be measured simultaneously. Such measurements also make it possible to extract information on the phase parameters θ, ϕ, and $\psi_{1,2}$ similarly to measurements of the ellipticity and azimuth of polarization for the quantum two-mode field (cf. [7]).

For this interferometer, let us consider measurements limited only by quantum noise (figure). We define the signal-to-noise ratio for the detected differences of the photon numbers as

$$F_k = \frac{\left|\langle N_k^{(-)} \rangle\right|}{\langle (\Delta N_k^{(-)})^2 \rangle}, \quad k = 12, 13, 23, \tag{12}$$

where $\langle (\Delta N_{ij}^{(-)})^2 \rangle$ are the variances of the observed quantities. Using definition (12) and taking into account expressions (9)–(11), we obtain the measured signal-to-noise ratios in the form

$$F_{ij} = \frac{2\left|\langle \lambda_{ij} \rangle\right|}{\langle (\Delta \lambda_{ij})^2 \rangle + \langle a_i^+ a_1 \rangle + \langle a_j^+ a_j \rangle}, \quad i, j = 1, 2, 3, \quad i \neq j. \tag{13}$$

If radiation at the input of the interferometer is in coherent state (6), relation (13) yields

$$F_{12,\,SQL} = \left|\sin 2\phi \cos(\phi_2 + \psi_2 - \psi_1)\right|, \tag{14a}$$

$$F_{13,\,SQL} = \frac{\left|\sin 2\theta \cos\phi \cos(\phi_1 + \psi_1)\right|}{\cos^2\theta + \sin^2\theta \cos^2\phi}. \tag{14b}$$

$$F_{23,\,SQL} = \frac{\left|\sin 2\theta \sin\phi \cos(\phi_3 - \psi_2)\right|}{\cos^2\theta + \sin^2\theta \sin^2\phi}. \tag{14c}$$

Expressions (14a)–(14c) specify the standard quantum limit for measurement of the signal-to-noise parameters for the SU(3) interferometer shown in the figure. In this case, the quantities $F_{k,\,SQL}$ vary within the range $0 \le F_{k,\,SQL} \le 1$.

However, coherent states (6) are not optimal for the limiting accuracy of the measurements being discussed. Indeed, the quantities F_k [see (13)] are maximal if light is supplied to the input of the interferometer in a nonclassical (squeezed) state. For primary entangled states (7), in view of the corresponding input values of the phase parameters θ and ϕ [SU(3) polarization states] and under specific phase relations for ψ_j and ϕ_j in the interferometer arms, the variances of the Gell-Mann parameters vanish: $\langle (\Delta \lambda_{ij})^2 \rangle = 0$. Therefore, the quantities F_k are given by

$$F_{ij} = \frac{2\left|\langle \lambda_{ij} \rangle\right|}{\langle a_i^+ a_i \rangle + \langle a_j^+ a_j \rangle}, \quad i, j = 1, 2, 3, \quad i \neq j. \tag{15}$$

Expression (15) fixes the achievable accuracy (limited by quantum noise) of measurement of the parameters F_k in the interferometer scheme under consideration. This accuracy is determined by fundamental limitations imposed by quantum fluctuations of the light fields V_j in vacuum states. All other conditions being the same, $F_k\, F_k \ge F_{k,\,SQL}$, $k = 12, 13, 23$. In particular, state (7) is twice as sensitive to the signal-to-noise ratio as coherent state (6).

Further, we assume that the mode a_3 is a classical pumping mode that is described by a complex-valued amplitude $\alpha_3 = |\alpha_3| e^{i\varphi}$, where φ is phase. In this case, the operators λ_j, $j = 4, \ldots, 7$, specified by Eqs. (1b)–(1e) take the form

$$\lambda_{4,6} = |\alpha_3| Q_{1,2}, \quad \lambda_{5,7} = -|\alpha_3| P_{1,2}, \tag{16}$$

where

$$Q_j = a_j e^{-i\varphi} + a_j^+ e^{i\varphi}, \quad P_j = i(a_j^+ e^{i\varphi} - a_j e^{-i\varphi}), \quad j = 1, 2 \tag{17}$$

are Hermitian quadratures that are the generalized coordinates of the respective modes. An interesting feature of this SU(3)-symmetry representation is that simultaneous and exact measurement of the isospin parameters λ_j with $j = 1$, 2, and 3 and the Hermitian quadratures Q_i and P_i with $i = 1$ and 2 is impossible, because the corresponding operators do not commute.

In quantum theory, the spin projection onto the particle momentum is associated with helicity, which is a conserved quantity (see, e.g., [13]). Therefore, correlations between the quantities Q_i and P_i and the isospin-polarization (Stokes) parameters λ_j can be considered as an analogue of helicity states in quantum optics. The scheme shown in the figure makes it possible to detect such states by measuring correlations of photocurrents at the output of the interferometer (cf. [14]).

CONCLUSIONS

In this study, the polarization of a three-mode light field has been described on the basis of the SU(3) algebra. The degree of polarization, as well as the conditions of high-precision measurements, has been determined. The three-channel SU(3) interferometer proposed in this work makes it possible to simultaneously measure the quantities associated with different subalgebras of the SU(3) algebra. The achievable sensitivity is limited by quantum noise for nonclassical states of the modes at the input of the interferometer. New helicity states of light, which manifest themselves in correlations between Hermitian quadratures and isospin-polarization operators, have been predicted.

The quantum properties of SU(3) polarization that have been considered in this study for three modes of a light field differ from the previously discussed SU(3) symmetry of a two-mode (biphoton) field, which can be in three different quantum states (such states were referred to as optical quarks [2]). They characterize the possible manifestations of *a posteriori* polarization of light and can be revealed only in the process of its measurement. Such polarization states of an optical system are analogous to macroscopic polarization states of the Schrödinger "cat" type that were considered in [15] and could also be classified as *a posteriori* states of light polarization.

ACKNOWLEDGMENTS

This work was supported in part by the Russian Foundation for Basic Research (project no. 01-02-17478) and a research program of both the Ministry of Industry, Science, and Technologies and the Ministry of Higher Education of the Russian Federation. The work of A.P.A. was supported by the Foundation Dinastiya and International Center for Theoretical Physics in Moscow.

REFERENCES

1. W. P. Bowen, N. Treps, and R. Schnabel, Phys. Rev. Lett. **89**, 253601 (2002).
2. A. V. Burlakov and D. N. Klyshko, Pis'ma Zh. Éksp. Teor. Fiz. **69**, 795 (1999) [JETP Lett. **69**, 839 (1999)].
3. P. A. Bushev, V. P. Karassiov, and A. V. Masalov, Opt. Spektrosk. **91**, 558 (2001) [Opt. Spectrosc. **91**, 526 (2001)].
4. A. S. Chirkin, A. A. Orlov, and D. Yu. Parashchuk, Kvantovaya Élektron. (Moscow) **20**, 999 (1993).
5. A. P. Alodzhants and S. M. Arakelyan, Zh. Éksp. Teor. Fiz. **113**, 1235 (1998) [JETP **86**, 672 (1998)].
6. D. N. Klyshko, Zh. Éksp. Teor. Fiz. **111**, 1955 (1997) [JETP **84**, 1065 (1997)].
7. A. P. Alodjants and S. M. Arakelian, J. Mod. Opt. **46**, 475 (1999).
8. J. Elliott and P. Dawber, *Symmetry in Physics* (Macmillan, London, 1981; Mir, Moscow, 1983), Vol. 2.
9. C. K. Law, H. Pu, and N. P. Bigelow, Phys. Rev. Lett. **81**, 5257 (1998).
10. A. S. Shumovsky, J. Phys. A **32**, 6589 (1999).
11. A. V. Prokhorov, A. P. Alodzhants, and S. M. Arakelyan, Opt. Spektrosk. **94**, 50 (2003) [Opt. Spectrosc. **94**, 50 (2003)].
12. G. Khanna, S. Mukhopadhyay, R. Simon, and N. Mukunda, Ann. Phys. **253**, 55 (1997).
13. V. B. Berestetskiĭ and E. M. Lifshitz, *Quantum Electrodynamics*, 2nd ed. (Pergamon Press, Oxford, 1982; Nauka, Moscow, 2001).
14. S. N. Bagayev, V. I. Baraulia, and A. E. Bonert, Laser Phys. **11**, 1178 (2001).
15. A. P. Alodjants, A. Yu. Leksin, A. V. Prokhorov, and S. M. Arakelian, Laser Phys. **10**, 603 (2000).

Translated by T. Syromyatnikova

Doklady Physics, Vol. 49, No. 3, 2004, pp. 158–162. Translated from Doklady Akademii Nauk, Vol. 395, No. 3, 2004, pp. 330–334.

TECHNICAL PHYSICS

Optimal Control of Emission by Ultrashort-Pulse Antennas Operating in a Packet Regime

Corresponding Member of the RAS L. D. Bakhrakh and M. Ya. Izrailovich

Received November 24, 2003

INTRODUCTION

In the case of operation of ultrashort-pulse antennas (UPAs) in a packet regime, i.e., when a beam of periodically repeated signals is emitted, a rather significant deviation of the time structure of actually emitted signals from the desired (perfect) structure occurs. A similar effect also takes place in the case of emission of single pulses. In particular, in these cases, the emitted signal turns out noticeably more stretched in time compared to both the signal at the antenna input, which is formed by a UPA generator, and the desired (perfect) signal.

To avoid these distortions, apart from the basic signal, an additional correcting signal (control signal) is applied to the antenna input [1–3]. Problems of the determination of such control signals can be conditionally divided into two classes. The first class corresponds to lowering the level of the residual radiation, in particular, to providing their total absence at a certain given instance of time. The second class of problems consists in the best consistency of an emitted signal to its desired (perfect) time structure in accordance with a certain best-approximation criterion. In this case, the condition of the total (or partial) absence of the radiation at a certain fixed instant of time, which is given in the form of linear isoparametric conditions, can be taken into account. As applied to the single-signal emission regime, these problems were solved in [1, 2].

In the case of emission in packet regimes, problems of the determination of control signals become considerably more complicated. This is caused by a number of reasons. First, there exists a build-up effect for the residual radiation from each emitted pulse, which noticeably enhances distortions. Second, each of the control signals applied to the antenna input within the time range between the onset of the action of the current and subsequent working signals affects the time structure of not only the current signals but also of all subsequent emitted signals. Third, by virtue of dynamic distortions, even in the case of periodic basic (working) and control signals, the signal emitted by the antenna is precisely a periodic function of time. Therefore, with the exclusion of the case of a large number of emitted pulses, the problem cannot be considered in the steady-state periodic regime.

Heuristic methods of solving the first-class problems, i.e., those of lowering the total intensity of residual radiation, were proposed in [3]. In this paper, we describe regular procedures based on constructing a sequence of special Green's functions, on the abstract theory of linear operators, and on variational methods in the $L^2(0; T)$ space [4]. These procedures are used for solving the second-class problems, namely, search for the best consistency with the perfect form of emitted signals.

THE GREEN'S FUNCTIONS DESCRIBING THE DYNAMICS OF EMISSION IN A PACKET REGIME

The dynamics of a unidirectional antenna emission in the case of a single input pulse formed by a UPA generator is defined in the form [2]

$$y_0(t) = \int_0^t h(t-\tau)x_0(\tau)d\tau, \quad t \in (0; T_1],$$
$$y_0(t) = \int_0^{T_1} h(t-\tau)x_0(\tau)d\tau, \quad t > T_1. \tag{1}$$

Here, $x_0(t)$ is the working pulse formed by the UPA generator, T_1 is the pulse duration, $h(t-\tau)$ is the antenna pulsed transition function, and $y_0(t)$ is the time diagram of the emitted signal.

In the case of the action of n periodic working pulses repeating with a period T ($T > T_1$), it follows from (1)

Moscow Research Institute of Instrument Building, Kutuzovskiĭ pr. 34, Moscow, 121170 Russia

Blagonravov Institute of Engineering Science, Russian Academy of Sciences, ul. Bardina 4, Moscow, 117334 Russia

1028-3358/04/4903-0158$26.00

that the time diagram of an emitted signal is determined by the expressions

$$y_0 = \sum_{i=1}^{l-1} \int_{(i-1)T}^{(i-1)T+T_1} h(t-\tau)x_0(\tau)d\tau + \int_{lT}^{t} h(t-\tau)x_0(\tau)d\tau, \quad t \in (lT, lT+T_1),$$

$$y_0 = \sum_{i=1}^{l} \int_{(i-1)T}^{(i-1)T+T_1} h(t-\tau)x_0(\tau)d\tau, \quad t \in (lT+T_1, (l+1)T], \quad l = 2, 3, \ldots, n-1, \tag{2}$$

$$y_0 = \sum_{i=1}^{n} \int_{(i-1)T}^{(i-1)T+T_1} h(t-\tau)x_0(\tau)d\tau, \quad t \in (nT; \infty).$$

As was shown in [5], expressions (2) with allowance for the T periodicity of the function $x_0(t)$ can be transformed to the form

$$y_0(t) = \int_0^{T_1} g_{l-1}(t-\tau)x_0(\tau)d\tau + \int_0^{t-lT} h(t-\tau-lT)x_0(\tau)d\tau, \quad t \in (lT; lT+T_1],$$

$$y_0(t) = \int_0^{T_1} g_l(t-\tau)x_0(\tau)d\tau, \quad t \in [lT+T_1, (l+1)T], \tag{3}$$

$$y_0(t) = \int_0^{T} g_n(t-\tau)x_0(\tau)d\tau, \quad t \in ((n-1)T+T_1, \infty),$$

by means of introducing new integration variables $\tau_i = \tau - (i-1)T$. Here,

$$g_l(t-\tau) = \sum_{i=0}^{l-1} h(t-\tau-iT).$$

For $y_0(t)$, expression (3) can be written in the more compact form

$$y_0(t) = \int_0^{T} \varphi_l(t, \tau, T_1, T)x_0(\tau)d\tau, \quad t \in (lT; (l+1)T], \quad l = 0, 1, \ldots, n-1, \tag{4}$$

where the sequence of the Green's functions $\varphi_l(t, \tau, T_1, T)$ is determined in the form

$$\varphi_0(t, \tau, T_1, T) = \begin{cases} h(t-\tau), & \begin{cases} \tau \in (0; t) \\ t \in (0; T_1] \end{cases} \\ & \begin{cases} \tau \in (0; T] \\ t \in (T_1; T] \end{cases} \\ 0, \quad \tau \in 9(t; T_1], \quad t \in (0; T], \end{cases}$$

$$\varphi_l(t, \tau, T_1, T) = \begin{cases} g_l(t-\tau), & \begin{cases} \tau \in (0; t-lT] \\ t \in (lT; lT+T_1] \end{cases} \\ & \begin{cases} \tau \in (0; T_1] \\ t \in (lT+T_1; (l+1)T] \end{cases} \\ g_{l-1}(t-\tau), \quad \tau \in (t-lT; T_1] \\ t \in (lT; lT+T_1], \end{cases} \tag{5}$$

$$l = 1, 2, \ldots, n-2,$$

$$\varphi_{n-1}(t, \tau, T_1, T) = g_{n-1}(t-\tau),$$

$$\tau \in (0; T_1], \quad t \in ((n-1)T; \infty).$$

Let the perfect (desired) law of a unidirectional emission $y_*(t)$ be given. It follows from the physical sense of the packet pulse emission that the function $y_*(t)$ is T-periodic, the starting time of each period being coincident with the onset of the action of a sequential working pulse $x_0(t)$. In this case, $y_*(iT_2) = 0$, where T_2 is the given instant of the pulse end ($T_1 < T_2 \le T$). As in the case of single-pulse emission, the functions $y_*(t)$ and $y_0(t)$ are substantially different. However, in the given case, their divergence is even more significant by virtue of the distortion build-up effect. The periodic correcting action $u(t)$ applied to the antenna input should be determined in a manner that allows the level of these distortions to be decreased.

Let a T-periodic correcting signal (periodic control action) $u(t)$ acting within the interval $(0, T)$ be applied to the antenna input along with the working signal $x_0(t)$. Then, the unidirectional signal $y_0(t)$ (4) emitted by the antenna is transformed to the form

$$y(t) = \int_0^{T} \varphi_l(t, \tau, T_1, T)x_0(\tau) + \int_0^{T} \varphi_l(t, \tau, T)u(\tau)d\tau, \quad t \in (lT; (l+1)T], \quad l = 0, 1, \ldots, n-1, \tag{6}$$

where the sequence of the Green's functions $\varphi_l(t, \tau, T)$ that characterize the effect of introducing the control

action $u(t)$ is determined similarly to (5) by the expression

$$\varphi_0(t, \tau, T) = \begin{cases} h(t-\tau), & \tau \in (0; t] \\ 0, & \tau \in (t; T], \end{cases}$$

$$t \in (0; T),$$

$$\varphi_l(t, \tau, T) = \begin{cases} g_l(t-\tau), & \tau \in (0; t-lT] \\ g_{l-1}(t-\tau), & \tau \in (t-lT, T], \end{cases} \quad (7)$$

$$t \in (lT; (l+1)T], \quad l = 1, 2, \ldots, n-2,$$

$$\varphi_{n-1}(t, \tau) = g_{n-1}(t-\tau), \quad \tau \in (0; T),$$

$$t \in ((n-1)T; \infty).$$

THE PROCEDURE OF CONSTRUCTING THE OPTIMAL CONTROL

As in the case of emission of a single signal [2], for the best consistency of the time diagram of an emitted signal $y(t)$ (6) with the perfect diagram $y_*(t)$, we introduce the functional

$$J(u) = \int_0^{nT} [(y - y_*)^2 + \gamma u^2]\,dt, \quad \gamma > 0. \quad (8)$$

The first term in (8) determines the closeness of the emitted signal $y(t)$ to its perfect structure $y_*(t)$, whereas the second term corresponds to the limited intensity of the desired control action $u(t)$.

As was indicated above, the functions entering into the functional, namely, both the given function $y_*(t)$ and $u(t)$ to be determined, are T-periodic. At the same time, the integration variable t is given within the segment $[0, nT]$. By virtue of this fact, in order to determine the function $y_*(t)$ that minimizes functional (8), we cannot directly employ the procedure described in [2] or other variational methods inherent in the theory of optimal control. Indeed, as a result of application of a certain method, the determined function $u_*(t)$ is not T-periodic, because the function $y(t)$ (6) is also not periodic. Therefore, the condition $u(t + T) = u(t)$ imposed on the function $u(t)$ in the case of the minimization of the functional $J(u)$ (8) is a specific limitation that cannot be imposed on the basis of procedures used in the optima-control theory.

By virtue of this fact, the following approach is applied to solve the problem formulated above. The functional $J(u)$ is transformed in the following manner:

$$J(u) = \sum_{l=0}^{n-1} \int_{lT}^{(l+1)T} [(y_l - y_*)^2 + \gamma u^2]\,dt. \quad (9)$$

Here, the values of the function $y(t)$ (6), which it acquires within the semisegments $t \in (lT; (l+1)T]$, $l = 0, 1, \ldots, n-1$, are denoted as y_l. In each n term in (9), the integration variable t acquires certain values within the same semisegments. As a result of replacing integration variables $t_l = t - lT$ in each of the terms of (9), the functional is reduced to the form

$$J(u) = \sum_{l=0}^{n-1} \int_0^T \{[y_l(t_l) - y_*]^2 + \gamma u^2\}\,dt_l. \quad (10)$$

Since, in each term of (10), the integration variable t_l varies within the same limits $[0; T]$, we may introduce an independent variable $\theta = t_l$ identical for each term. Thus,

$$J(u) = \sum_{l=0}^{n-1} \int_0^T \{[y_l(\theta) - y_*(\theta)]^2 + \gamma u^2(\theta)\}\,d\theta. \quad (11)$$

In this case, the expressions for $y_l(\theta)$, $l = 0, 1, \ldots, n-1$ are determined in accordance with (6) by the substitution θ for $t - lT$ in the Green's functions $\varphi_l(t, \tau, T_1, T)$ (5) and $\varphi_l(t, \tau, T)$ (7).

To minimize the functional $J(u)$ (11), in analogy with the signal correction in the case of single-pulse emission [2], the most efficient procedure is based on both the use of the abstract theory of linear operators in the space $L^2(0; T)$ and calculations of the Gateaux derivative over the desired function u [4] with the specifics of the given problem taken into account. In this case, in accordance with both (6) and the transformation of the arguments described above, the expressions for $y_l(\theta)$ are written out in the form of linear operators

$$y_l = A_l x_0 + B_l u, \quad l = 0, 1, \ldots, n-1, \quad (12)$$

where A_l, B_l are linear operators determined in terms of the corresponding Green's functions.

With allowance for (12), the abstract form of the functional $J(u)$ (11) being minimized is the following:

$$J(u) = \sum_{l=0}^{n-1} (A_l x_0 + B_l u - y_*, A_l x_0 + B_l u - y_*) + \gamma n(u, u). \quad (13)$$

As a result of application of the procedure developed for the determination of the minimization conditions [4] to the functional $J(u)$ (13), we can determine the following linear operator equation with respect to the desired function u:

$$\left(\sum_{l=0}^{n-1} B_l^* B_l + \gamma n\right) u = \sum_{l=0}^{n-1} (B_l^* y_* - B_l^* A_l x_0). \quad (14)$$

In Eq. (14), operators conjugate to the operators B_l are

denoted by B_l^*. Since

$$B_l f = \int_0^T \varphi_l(\theta, \tau, T) f(\tau) d\tau,$$

the conjugate operators can be written in the form

$$B_l^* f = \int_0^T \varphi_l(\theta, \tau, T) f(\theta) d\theta,$$

where f is an arbitrary function.

Operator equation (14) determines the optimal control function

$$u^*(t) = R(n, \gamma) \sum_{l=0}^{n-1} (B_l^* y_* - B_l^* A_l x_0). \quad (15)$$

Here, $R(n, \gamma)$ is the linear operator inverse with respect to the operator

$$\sum_{l=0}^{n-1} (B_l^* B_l + \gamma n).$$

Since operator equation (14) in its nonabstract form is the Volterra equation of the second kind, the operator $R(n, \gamma)$ is the resolvent to this equation, whereas the function $u^*(t)$ is its solution.

ALLOWANCE FOR QUENCHING THE RESIDUAL RADIATION

Optimal correcting action $u^*(t)$ (15) provides the best consistency (in the sense of the integral square metric) with the perfect signal $y_*(t)$ over the entire period T corresponding to the emission of each of n pulses that form a packet. However, as was noted above, the problem of lowering the total level of residual radiation also remains urgent. The corresponding solution is presented in [3] without allowance for the criterion of the best consistency of the time diagram for the emitted signal $y(t)$ (6) with the perfect diagram $y_*(t)$ as a whole. By virtue of this fact and based on the above procedure of constructing the function $u^*(t)$ (15), it is also reasonable to take into account the conditions of quenching the summed residual radiation.

In accordance with (5)–(7), the emission intensity at the instants of time $t = lT$, $l = 1, 2, \ldots, n-1$ before the onset of the emission of each of the subsequent pulses is determined by the expression

$$y(lT) = \int_0^{T_1} g_{l-1}(lT - t) x_0(t) dt + \int_0^T g_{l-1}(lT - t) u(t) dt. \quad (16)$$

According to [3], the functional

$$y_n = \sum_{l=1}^{n} y(lT) = \int_0^{T_1} G_n(t) x_0(t) dt + \int_0^T G_n(t) u(t) dt, \quad (17)$$

is used as the summed intensity of the residual radiation. Here, by virtue of (16), the relationship

$$G_n(t) = \sum_{l=1}^{n} g_{l-1}(lT - t)$$

is valid. The minimization of the summed residual radiation y_n (17) is equivalent to the minimization of the second term.

By virtue of the aforesaid, for the determination of $u^*(t)$, instead of the functional $J(u)$ (13), we introduce the extended functional

$$J(u, \lambda) = \sum_{l=0}^{n-1} (A_l x_0 + B_l u - y_*, A_l x_0 + B_l u - y_*) + \gamma n(u, u) + \lambda c_n u, \quad (18)$$

where $c_n u = \int_0^T G_n(t) u(t) dt$ is the linear operator and λ is the weight coefficient (Lagrange multiplier).

In the case of functional (18), Eq. (14) can be represented as

$$\left(\sum_{l=0}^{n-1} B_l^* B_l + \gamma n \right) u = \sum_{l=0}^{n-1} (B_l^* y_* - B_l^* A_l x_0) - \lambda G_n. \quad (19)$$

The solution to Eq. (19) is obtained in the form

$$u^*(t, \lambda) = R(n, \gamma)(D_n - \lambda G_n), \quad (20)$$

where

$$D_n = \sum_{l=0}^{n-1} (B_l^* y_* - B_l^* A_l x_0).$$

If, as in [3], a limitation for the intensity of the con-

trol action is given,

$$\frac{1}{T}\int_0^T u^2 dt \le W, \tag{21}$$

then we can determine from (20), (21) the value of λ^* corresponding to the limiting admissible value of W:

$$\lambda^* = \frac{1}{b}[c + \sqrt{c^2 + (WT - a)b}]. \tag{22}$$

Here,

$$a = \int_0^T R^2(n, \gamma) D_n^2 dt,$$

$$b = \int_0^T R^2(n, \gamma) G_n^2 dt,$$

$$2c = \int_0^T R^2(n, \gamma) D_n G_n dt.$$

The final expression for the optimal control is found by substitution of λ^* (22) into formula (20).

REFERENCES

1. L. D. Bakhrakh and M. Ya. Izrailovich, Antenny, No. 2, 45 (2001).
2. L. D. Bakhrakh and M. Ya. Izrailovich, Dokl. Akad. Nauk **379**, 325 (2001) [Dokl. Phys. **46**, 491 (2001)].
3. L. D. Bakhrakh and M. Ya. Izrailovich, Dokl. Akad. Nauk **391**, 754 (2003) [Dokl. Phys. **48**, 432 (2003)].
4. R. E. Bellman, I. Glicksberg, and O. A. Gross, *Some Aspects of the Mathematical Theory of Control Processes* (Rand, Santa Monica, CA, 1958; Inostrannaya Literatura, Moscow, 1962).
5. M. Ya. Izrailovich, Probl. Mashinostr. Nadezhnosti Mash., No. 6, 10 (1995).

Translated by G. Merzon

Doklady Physics, Vol. 49, No. 3, 2004, pp. 163–166. Translated from Doklady Akademii Nauk, Vol. 395, No. 3, 2004, pp. 335–338.

TECHNICAL PHYSICS

Production of Disperse Composite Materials in a Dusty Plasma

A. S. Ivanov[1], V. S. Mitin[2], A. F. Pal[3], A. N. Ryabinkin[3]*, A. O. Serov[3], E. A. Skryleva[4], A. N. Starostin[1], Academician V. E. Fortov[5], and Yu. M. Shulga[5]

Received December 8, 2003

In this study, we established that the use of a dusty plasma trap makes it possible to produce a disperse composite material (DCM) in amounts necessary for physical and technological experiments. A diamond-based Ni-coated DCM was investigated in detail. The coating is a dense 10-nm-thick Ni layer with a characteristic roughness of about 3 nm. It is shown that powders are virtually free of dendritic coating-material formations with a fractal structure, and a Ni film is strongly bonded to the diamond surface.

INTRODUCTION

The laboratory study of dusty plasma structures became possible due to simple inexpensive setups providing plasma traps, i.e., plasma regions where disperse particles can be confined for a long time [1]. The application of dusty plasma traps is of great practical interest, because they significantly expand the possibilities of creating new unique materials, which cannot be produced by *in situ* methods due to, for example, either thermodynamic or kinetic limitations. We imply the usage of dusty plasma traps in the technology of producing high-quality DCMs—powders consisting of coated particles with sizes of 0.1–10 μm. The current methods of producing such DCMs are characterized by a number of disadvantages, including discontinuities in coatings, poor adhesion between the deposited component and the surface of the initial material, and the formation of agglomerates containing several particles of the initial material coated by a common shell. As a result, powders produced by these methods are inhomogeneous and, eventually, products made from them have worse strength properties.

By using the features of the state of small particles in a plasma, it is possible to provide strong adhesion between a coating and a substrate, control the process of coating deposition, and preset parameters of the composition and structure of composite particles. In this study, we report some results of the investigation of DCMs produced in dusty plasma by a method similar to that described in [2, 3].

EXPERIMENTAL PROCEDURE

In this work, we studied DCMs produced on a plasma setup similar to that described in [4]. In the vacuum chamber of the setup, an asymmetric rf capacitive discharge (up to 30 W in power) was maintained at pressures between 0.1 and 13.3 Pa. The chamber volume was equal to 35 l, and the circulation rate of the gas (argon) in our experiments did not exceed 10 l/s.

The dusty plasma trap is formed by the special disposition of electrodes. Using a dispersing device, the trap can be filled with a dust whose particles have sizes from 1 to 20 μm. Disperse particles in such a trap have negative electric charges from 10^3e to 10^4e, where e is the electron charge. Coulomb repulsion sharply retards the coagulation of particles forming a long-lived quasi-liquid. The concentration of disperse particles that was measured by the methods of laser diagnostics [5] was found to be 10^6 cm^{-3}.

Levitated particles were coated by an atomic beam produced by a sputtering magnetron system. This system provides a directed sputtering-atom flux of 10^{16}–10^{17} s^{-1} cm^{-2} with an average energy of 2–10 eV [6]. As a substrate material, we took diamond and glassy carbon powders with a mean size of particles of about 3–4 μm and Al_2O_3 and SiO_2 powders whose particles have a mean size of about 2 μm. As a coating

[1] *Russian Research Centre Kurchatov Institute, pl. Kurchatova 1, Moscow, 123182 Russia*

[2] *Bochvar All-Russia Research Institute of Inorganic Materials, ul. Rogova 5, Moscow, 123060 Russia*

[3] *Skobel'tsyn Institute of Nuclear Physics, Moscow State University, Vorob'evy gory, Moscow, 119899 Russia*

* *e-mail: aserov@mics.msu.su*

[4] *Moscow State Institute of Steel and Alloys (Technological University), Leninskiĭ pr. 4, Moscow, 117936 Russia*

[5] *Institute of Problems of Chemical Physics, Russian Academy of Sciences, Chernogolovka, Moscow oblast, Russia*

1028-3358/04/4903-0163$26.00

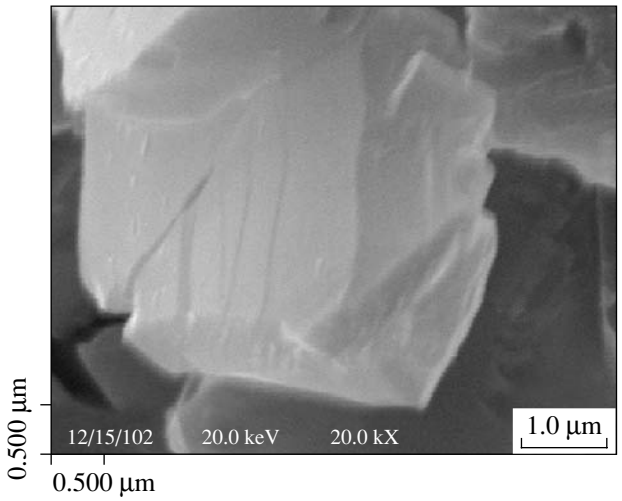

Fig. 1. Image of Ni-coated diamond particles in a microphotograph obtained with a scanning electron microscope.

material, we used copper, nickel, zirconium, stainless steel, and other metals.

RESULTS AND DISCUSSION

In this study, we report the results of our investigations of diamond-based Ni-coated DCMs. To determine the properties of the product, we applied a number of methods: X-ray analysis, precision chemical analysis, scanning and transmission electron microscopy, etc. We also studied X-ray photoelectron spectra of the DCMs.

Unlike the photographs of initial diamond powder, the images of the particles after treatment are quite clear (Fig. 1). This indicates that the electric conductivity of the coating is relatively high. Within the above resolution, the coating is rather smooth, follows the substrate relief, and contains no fractal "cauliflower-type" structures [3].

The microphotographs of the DCM-particle edges made with an ÉVM-100B transmission electron microscope operating at an accelerating voltage of 50 kV showed that the characteristic coating roughness is about 3 nm (Fig. 2). There are also indications that the Ni film is separated from the diamond substrate.

The nickel content in a sample was analyzed by the method of burning the sample in oxygen at 1673 K. The initial diamond powder was completely burned in this process. The metal concentration in the DCM sample under study, which was found from the weight of unburned residue, is given in the table.

The specific surface was determined by measuring the low-temperature adsorption of argon (the Brunauer–Emmet–Teller method). The results of our investigations are also given in the table. The mean coating thickness evaluated from the measured nickel concentration and specific surface was equal to about 10 nm.

In the range of angles under investigation, the X-ray diffraction patterns for the initial diamond (which were recorded by using an ADP-1 DRON diffractometer with monochromatic CrK_α radiation) virtually represent a single peak attributed to the (111) reflection of the diamond lattice (Fig. 3). In the diffraction pattern of DCMs, nickel manifests itself in the form of two peaks corresponding to the (111) and (200) reflections of the fcc lattice. The lattice parameter calculated using these peaks equals 0.3529 nm, which slightly exceeds the value in bulk nickel (0.3524 nm [7]). The size of the regions of coherent scattering from nickel that corresponds to the coating thickness along the direction perpendicular to the (200) plane was evaluated by the formula $D_{200} = \frac{\lambda}{\beta}\cos\Theta$, where λ is the wavelength of X-ray radiation and β is the half-width of the (200) diffraction peak. The lower intensity peak was chosen

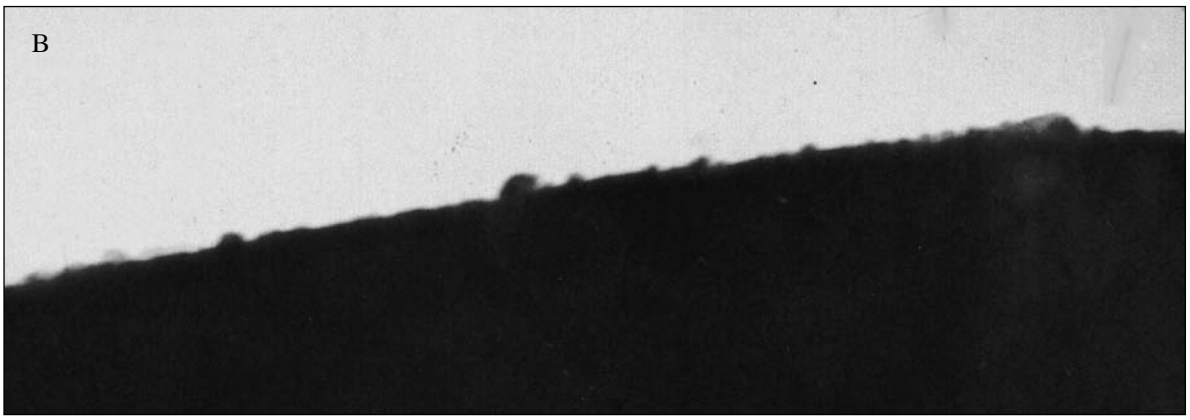

Fig. 2. Image of a Ni-coated diamond particle in a microphotograph obtained with a transmission electron microscope. The height of the letter is equal to 57 nm.

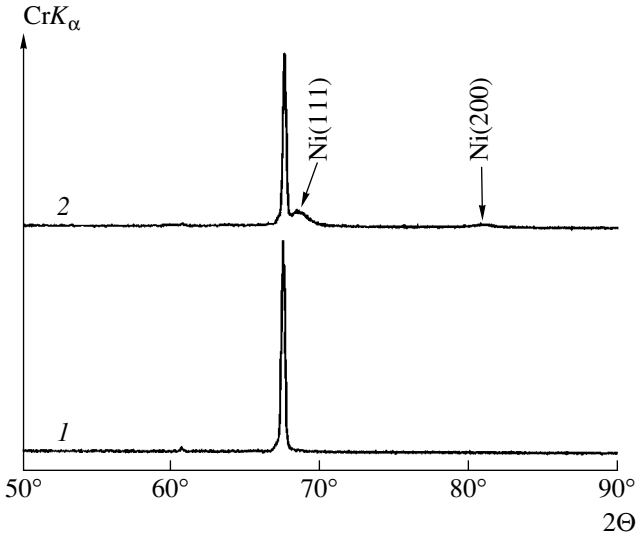

Fig. 3. X-ray diffraction patterns of the (*1*) initial diamond powder and (*2*) DCM sample under investigation.

because its half-width can be evaluated more accurately than that of the (111) Ni peak, which overlaps the (111) peak of diamond. It turns out that D_{200} = 12.0 nm for the sample under discussion. This value is in agreement with the data on the mean coating thickness obtained by measuring the specific surface and mean nickel content in the sample.

The magnetic properties of the samples were studied with an EG&G PARC M4500 vibrating magnetometer. The samples for investigations were placed in a thin diamagnetic ampoule the signal from which was taken into account when processing data. The magnetization curve of the DCMs under investigation is represented in the form of the hysteresis loop with a coercive force of H_c = 131 Oe. The saturation state (where specific magnetization M is independent of the magnetic field strength H) is not attained even at $H = 10^4$ Oe. Consequently, a sample contains superparamagnetic nickel particles. Using the M value for $H = 10^4$ Oe, it is possible to evaluate the content of ferromagnetic nickel $C_{f\,Ni}$ in the sample:

$$C_{f\,Ni} = \frac{M_1}{M_s},$$

where M_1 is the M value measured at $H = 10^4$ Oe and M_s is the saturation magnetization for bulk nickel (M_s = 55 emu/g [8]). As is seen in the table, the $C_{f\,Ni}$ value is much lower than that of C_{Ni} found by the above method of unburned residue. This difference can be attributed to the fact that, in addition to the superparamagnetic particles, the sample contains nickel in the form of nickel oxide NiO, which is an antiferromagnetic material [9].

To investigate X-ray photoelectron spectra, the samples under study (in the form of powders) were pressed as a continuous layer into indium substrates. The spectra were recorded with a PHI-5500 spectrometer with a spherical analyzer. The residual pressure in the spectrometer chamber did not exceed 7×10^{-8} Pa.

From the general X-ray photoelectron spectra, it follows that the basic element on the surface of initial diamond is carbon. After the deposition of a coating, the basic element is nickel. As would be expected, nickel in the surface layer under investigation is present in the form of both metal and its oxide on the metal surface. The Ni 2*p* line (Fig. 4) is a complex curve consisting of three peaks. Two of them, corresponding to the binding energies 861.2 and 855.6 eV, are associated with nickel oxide, and the third (852.8 eV), with metallic nickel. Short-term etching (less than 1 min) of the sample by an Ar^+ ion beam in the spectrometer chamber made it possible to virtually completely remove the NiO film from the surface (Fig. 4). This testifies to a compara-

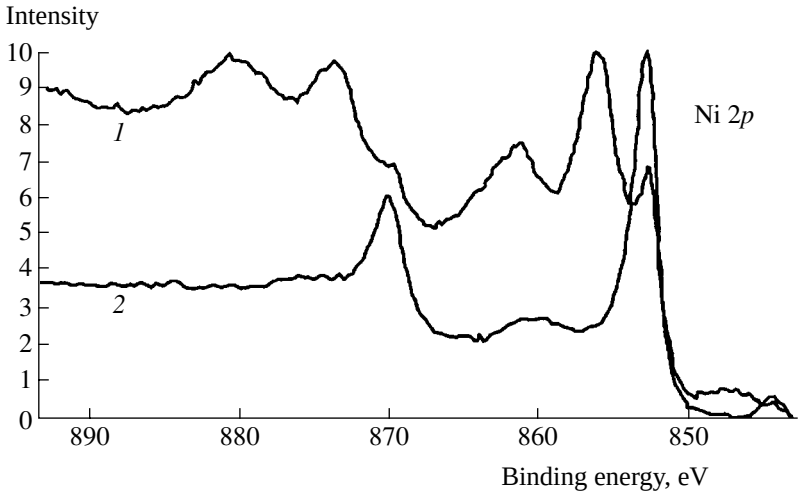

Fig. 4. Photoelectron spectra of Ni 2*p* for the DCM under investigation (*1*) before and (*2*) after ion etching.

Results of the analyses of the samples under investigations

Diamond powder	C_{Ni}, wt %	S, m^2/g	H_c, Oe	M_1, emu/g ($H = 10^4$ Oe)	$C_{f\,Ni}$, wt %
Initial	0	0.76	0	0	0
Ni-coated	7.5	1.14	131	0.85	1.55

tively high oxidation stability of the coating. The Ni coating thickness evaluated from the X-ray photoelectron spectra obtained during ion etching was no less than 10 nm. This value is in good agreement with the data mentioned above.

CONCLUSIONS

Thus, our investigations demonstrate that the use of a dusty plasma makes it possible to produce a disperse composite diamond-based Ni-coated material in amounts necessary for physical and technological experiments. The coating is a dense nickel layer with a thickness of about 10 nm and a characteristic roughness of about 3 nm. In contrast to [3], our samples are virtually free of dendritic formations with a fractal structure in the coating material, and the nickel film is strongly bonded to the diamond surface.

ACKNOWLEDGMENTS

This work was supported by the Russian Foundation for Basic Research, project no. 01-02-17726a.

REFERENCES

1. A. P. Nefedov, O. F. Petrov, and V. E. Fortov, Usp. Fiz. Nauk **167**, 1215 (1997) [Phys. Usp. **40**, 1163 (1997)].
2. V. Yu. Baranov, I. A. Belov, V. E. Fortov, *et al.*, German Patent No. 19832908.3 (July 1998).
3. H. Kersten, P. Schmetz, and G. M. W. Kroesen, Surf. Coat. Technol. **108**–**109**, 507 (1998).
4. A. Ivanov, A. Pal, A. Ryabinkin, *et al.*, in *Proceedings of the 16th International Symposium on Plasma Chemistry, Taormina, 2003*, p. 542.
5. Tsuyoshi Fukuzava, Kawasaki Hiroharu, *et al.*, J. Appl. Phys. **83**, 4212 (1998).
6. B. S. Danilin and V. K. Syrchin, *Magnetron Sputtering* (Radio i Svyaz', Moscow, 1982).
7. *Card-File of JCPDS: International Centre for Diffraction Data*, 1995, 04–0850.
8. C. Kittel, *Introduction to Solid State Physics*, 5th ed. (Wiley, New York, 1976; Nauka, Moscow, 1978).
9. N. W. Ashcroft and N. D. Mermin, *Solid State Physics* (Holt, Rinehart and Winston, New York, 1976; Mir, Moscow, 1979).

Translated by Yu. Vishnyakov

Doklady Physics, Vol. 49, No. 3, 2004, pp. 167–170. Translated from Doklady Akademii Nauk, Vol. 395, No. 3, 2004, pp. 339–342.

TECHNICAL PHYSICS

Nickel Alloy Substrates with a Sharp Cube Texture for High-T_c Superconducting Tapes

Academician V. M. Schastlivtsev*, Corresponding Member of the RAS V. V. Ustinov*, D. P. Rodionov*, B. K. Sokolov*, I. V. Gervas'eva*, Yu. V. Khlebnikova*, A. P. Nosov*, V. A. Sazonova*, V. G. Vasil'ev, E. V. Vladimirova**, A. Abaleshev***, P. Gierlowski***, S. Lewandowski***, and H. Szymczak*****

Received December 11, 2003

The formation of a sharp cube texture in thin metallic tapes became of interest due to the development of technology for producing high-T_c superconductor (HTSC) films on flexible tape substrates with a sharp cube texture [1–4]. Such technology opened new prospects in practical applications of HTSCs. Due to the epitaxy phenomenon, a texture with low-angle grain boundaries is formed in HTSC polycrystalline films deposited onto these substrates, which increases the critical transport current [1, 2]. High-purity (99.99%) nickel with high corrosion resistance under heating was initially used as the substrate material. Under 95–99% rolling reduction and recrystallization, it is possible to achieve high sharpness of the cube texture with misorientations in the rolling plane up to 5°–10°. The low mechanical properties of the nickel tape caused a number of technological difficulties in the manufacture of superconducting structures. In addition, nickel is a ferromagnet at cryogenic temperatures, which prevents the production of superconductors with the maximum functionality.

The principal aim of this work is the development of nickel-based alloys that have a sharp cube texture resembling a single-crystal texture, enhanced strength characteristics, and a Curie point below 70 K, that is, below the working temperature of the superconducting composite (about 76 K).

* *Institute of Metal Physics, Ural Division, Russian Academy of Sciences, ul. S. Kovalevskoĭ 18, Yekaterinburg, 620219 Russia e-mail: phym@imp.uran.ru*

** *Institute of Solid State Chemistry, Ural Division, Russian Academy of Sciences, ul. Pervomaĭskaya 91, Yekaterinburg, 620219 Russia e-mail: ihim2@prm.uran.ru*

*** *Instytut Fizyki Polskiej Akademii Nauk, Al. Lotnikóv 32/46, Warsaw, PL-02-668 Poland e-mail: gierl@ifpan.edu.pl, lewan@ifpan.edu.pl, szymh.edu.pl*

The transition metals of groups Va, VIa, and VIIa of the periodic table were used as alloying elements. The phase diagrams of alloys of these metals with nickel include large regions of the disordered substitutional solid solution with the fcc structure.

Alloys with the following compositions were manufactured (the alloying ranges in at. % are indicated in brackets): Ni–Cr (2.1–22.0), Ni–Mo (1.6–9.3), Ni–V (2.5–10.1), Ni–W (1.1–7.4), Ni–Mn (1.9–22.1), Ni–Re (1.1–4.1), and Ni–Nb (1.9–5.4). The alloys were melted in alundum crucibles in an argon atmosphere using 99.94% pure nickel and alloying elements with purity no less than 99.8%. The weight of ingots was equal to 200–500 g. The technology for producing cold-rolled and recrystallized tapes was described in [3, 4, 6–9]. In this work, 30–50 runs of cold rolling provided a deformation degree of about 98%.

Due to deformation, the material acquires a crystallographic texture with the main components (*S*) $\{123\}\langle 634\rangle$, (*C*) $\{112\}\langle 111\rangle$, and (*B*) $\{110\}\langle 112\rangle$. The alloying of nickel changes the proportions between the *S*, *C*, and *B* components. As a result, the deformation texture transforms from the type characteristic of copper to that characteristic of α brass. The experiments demonstrated that a change in the lattice constant up to 3.540–3.555 Å (Fig. 1) with the alloying of pure nickel gives rise to significant transformation of the deformation texture. For larger lattice constants in the alloy, the texture induced by cold rolling corresponds to that characteristic of α brass. In fact, the alloying range is limited by an alloy lattice constant of 3.54 Å, because the "copper-type" texture is preserved in this case. The existence of this texture is a necessary condition for the formation of the sharp cube texture under annealing. The quantitative analysis of the deformation texture using three-dimensional orientation functions demonstrated that the transformation from the copper-type texture to the α-brass texture occurs when the sum of the volume fractions of the *C* and *S* components becomes smaller than the doubled volume fraction of the *B* component.

1028-3358/04/4903-0167$26.00 © 2004 MAIK "Nauka/Interperiodica"

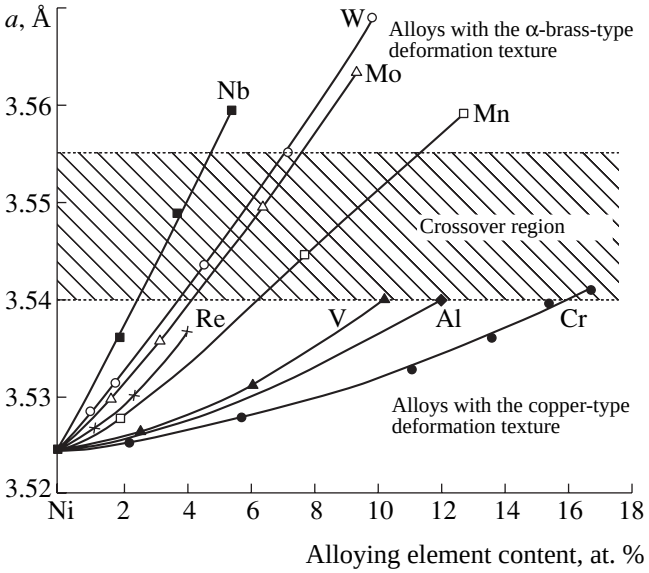

Fig. 1. Lattice parameter for the fcc nickel alloys vs. the alloying element content.

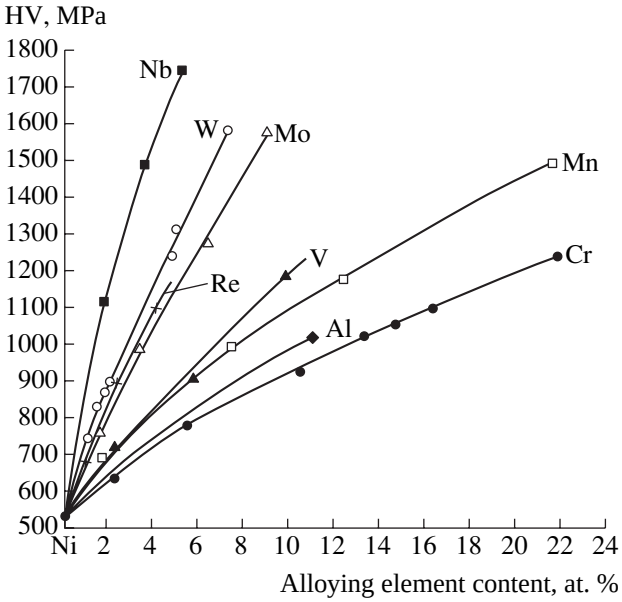

Fig. 2. Hardening of nickel alloyed with various elements of the periodic table.

An attempt to attribute the texture transformation to the stacking fault energy under alloying, which decreases with an increase in the content of the alloying element, failed because the γ_{sf} value is high ($\gamma/Gb \times 10^{-3}$ ratio is larger than 4–5). For such γ_{sf} values, it is difficult to observe the splitting of dislocations by electron microscopy. Vishnyakov [5] concluded that the texture transformation in fcc copper alloys occurs at 20–30 mJ/m^2.

The allowable limits for alloying in nickel alloys (in at. %) are determined as follows: up to 15.0 in Ni–Cr, up to 10.1 in Ni–V, 4–5 in Ni–W and Ni–Mo, up to 5.0 in Ni–Re, and up to 2.0 in Ni–Nb [7–9]. In Ni–Mn alloys, the copper-type texture remains for a Mn content as high as 13 at. % (Fig. 1).

The annealing of deformed alloys at 900–1100°C leads to the formation of the $\{100\}\langle 001\rangle$ primary recrystallization texture. In the alloys where the copper-type texture is formed under deformation, the sharp cube texture is the basis for the functional composition alloy–buffer layer–superconductor. Indeed, due to epitaxy, the sharp, almost single-crystalline, substrate texture transfers its perfect characteristics to the buffer layer and superconductor.

Two problems are solved by alloying. First, alloying leads to substantial hardening of the tape. This fact is important when the substrate becomes as thin as 30–50 μm. The effect of alloying on the hardness of the alloys within the allowable alloying range is illustrated in Fig. 2. The efficiency of hardening qualitatively correlates with the variation of the lattice constant under alloying (Fig. 1). The hardening of the alloy increases with an increase in the lattice expansion per 1 at. % of the alloying element. In the region where we observe the sharp cube texture associated with recrystallization, it is possible to achieve more than doubled hardening

Parameters of the textured tapes made of nickel and nonmagnetic nickel alloys

Alloy composition, at. %	Alloy composition, wt %	*a*, Å	Grain size before rolling, μm	HV, MPa	σ_T, MPa	T_C, K	Texture misorientation	
							along the rolling direction	across the rolling direction
Ni	99.93	3.5240	30	538	74	626	6.3	11
Ni–11.0 Cr	9.9	3.5329	25	924	148	~0	5.4	8.2
Ni–13.5 Cr	12.2	3.5358	20	1032	187	antiferromagnet	5.9	9.9
Ni–10.1 V	8.9	3.5400	13	1188	272	<50	6.7	13

Note: Texture misorientation is characterized by the half-width of the {200} peak in these directions.

(HV hardness increases from 500 MPa in pure nickel to 1000–1100 MPa in the alloys).

Second, nonmagnetic alloys can be produced due to alloying. Alloying only with V and Cr substantially decreases the Curie temperature within the allowable alloying range. Such alloys as Ni–10 at. % V and Ni–10–11 at. % Cr had $T_C < 50$ K. The alloys with the Cr content exceeding 14 at. % were antiferromagnets. In Mo-alloyed nickel alloys, it was impossible to attain T_C lower than 70 K, because alloying with 4–5 at. % Mo leads to changes in the deformation texture preventing the formation of the cube texture after recrystallization.

In addition, the alloying of nickel with the elements of groups Va, VIa, and VIIa of the periodic table allowed us to solve the technological problem of using less pure nickel (lower than 99.9%) to produce alloys retaining their sharp cube texture (the misorientation of the texture in the tape plane was equal to 6°–10°, the content of the cubic component was as high as 95%) [6–8].

The onset temperature for the secondary recrystallization destroying the cube texture in the nickel alloys under discussion lies in the range 1000–1150°C. Therefore, industrial operations concerning the sputtering of buffer and functional layers can be carried out at temperatures up to 800–900°C. The table presents a number of parameters characterizing the 110- to 120-μm-thick textured tapes made of nickel and nonmagnetic nickel alloys by cold rolling (98% deformation degree) and annealing at 900°C for 1 h. The volume fraction of the $\{100\}\langle 001\rangle$ cubic component in the textures of the nonmagnetic nickel alloys was equal to 90–95%.

The functionality of the nickel-alloy substrates was tested by the deposition of the bilayer structure consisting of the CeO_2 buffer layer and the $YBa_2Cu_3O_{7-\delta}$ HTSC film onto the textured tape of the Ni–11 at. % Cr alloy (annealed at 950°C for 1 h).

The CeO_2 buffer layer and superconducting $YBa_2Cu_3O_{7-\delta}$ layer were deposited onto the substrate by the laser sputtering of polycrystalline targets with the suitable composition. The first layers were deposited in vacuum (9×10^{-6} Torr) on substrates heated up to 600°C. When the film thickness attained 50 nm, oxygen was let in the chamber (up to a pressure of 10^{-2} Torr). Then, the deposition of the buffer layer was continued up to 750 nm. The superconductor layer was deposited at substrate temperature (version 1) 700 and (version 2) 720°C. In this case, the oxygen pressure was equal to 0.28 Torr and the film thickness was equal to 300 nm. After termination of the sputtering process, the chamber was filled with oxygen up to a pressure of 0.5 atm and the structure was cooled to 200°C at a rate of 10 K/min.

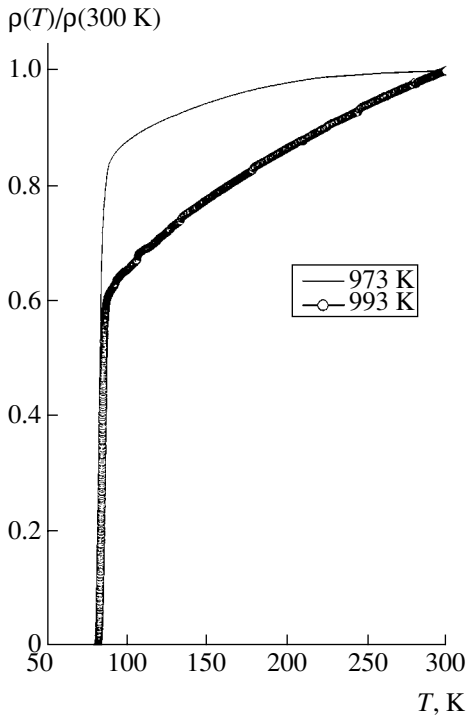

Fig. 3. Temperature dependence of the normalized resistivity for the $CeO_2/YBa_2Cu_3O_{7-\delta}$ bilayer structures grown on the textured tapes of Ni–11 at. % Cr alloy.

According to the x-ray diffraction data, the texture misorientations in the grown HTSC films are equal to 6.7° and 10° along and across the rolling direction, respectively (version 2).

Figure 3 shows the temperature dependence of the ratio $\frac{\rho(T)}{\rho(300\ \mathrm{K})}$, where $\rho(T)$ is the resistivity of the produced structures at temperature T. The superconducting transition point is equal to 81 and 83 K for versions 1 and 2, respectively. For these two cases, $\rho(T)/\rho(300\ \mathrm{K})$ is equal to 1.138 and 1.534 and the width of the superconducting transition is equal to 4 and 3.24 K, respectively. Such parameters are only slightly worse than those for heterostructures grown on $SrTO_3$ single-crystal substrates [11].

ACKNOWLEDGMENTS

This work was supported by the Presidium of the Russian Academy of Sciences (project no. 9), the Russian Foundation for Basic Research (project no. 01-03-32506), the Council of the President of the Russian Federation for Support of Young Russian Scientists and Leading Scientific Schools (project nos. NSh-1380.2003.2, NSh-778.2003.3), and the Russian and Polish Academies of Sciences (project no. PBZ-KBN-013/T08/19).

REFERENCES

1. A. Goyal, D. P. Norton, J. D. Budai, *et al.*, Appl. Phys. Lett. **69**, 1795 (1996).
2. D. P. Norton, A. Goyal, J. D. Budai, *et al.*, Science **274**, 755 (1996).
3. E. D. Specht, A. Goyal, D. F. Lee, *et al.*, Supercond. Sci. Technol. **7**, 945 (1998).
4. J. Eickmeyer, D. Selbmann, R. Opitz, *et al.*, Physica C (Amsterdam) **341**–**348**, 2425 (2000).
5. Ya. D. Vishnyakov, *Stacking Faults in Crystal Structure* (Metallurgiya, Moscow, 1970).
6. D. P. Rodionov, I. V. Gervas'eva, Yu. V. Khlebnikova, and B. K. Sokolov, Fiz. Met. Metalloved. **92** (3), 24 (2001).
7. D. P. Rodionov, I. V. Gervas'eva, Yu. V. Khlebnikova, and B. K. Sokolov, Fiz. Met. Metalloved. **94** (6), 62 (2002).
8. D. P. Rodionov, I. V. Gervas'eva, Yu. V. Khlebnikova, and B. K. Sokolov, Fiz. Met. Metalloved. **93** (5), 68 (2002).
9. J. D. Budai, A. Goyal, D. P. Norton, *et al.*, US Patent No. 5739086 (1998).
10. A. Goyal, E. D. Specht, D. M. Kroeger, *et al.*, US Patent No. 5964966 (1999).
11. E. Varesi, G. Celentano, T. Petrisor, *et al.*, Supercond. Sci. Technol. **16**, 498 (2003).

Translated by K. Kugel

Doklady Physics, Vol. 49, No. 3, 2004, pp. 171–174. Translated from Doklady Akademii Nauk, Vol. 395, No. 1, 2004, pp. 43–46.

MECHANICS

Conservation Laws in Vibration Theory

Yu. I. Bobrovnitskiĭ

Presented by Academician K.V. Frolov September 19, 2003

Received October 16, 2003

Conservation laws, or integrals of motion, are important in mechanics and other sciences, because they make it possible to analyze the motion of a certain system without solving the equations of motion. The laws of conservation of energy, momentum, power flux, etc., are among these laws [1].

Conservation laws are closely related to the symmetry properties of the system under consideration. Jacobi was probably the first to point out this fact [1]. The most general result in this field was obtained in [2], where conservation laws were expressed explicitly in terms of the Lagrangian and symmetry transformations (Noether's theorem). Numerous more recent works were devoted to the expansion of Noether's group-theoretical approach to systems and media for which the Lagrangian does not exist (see, e.g., [3, 4]). Some works concerned the creation of artificial procedures for deriving certain conservation laws directly from the equations of motion (e.g., [5, 6]). However, the general theory and method of constructing the complete set of conservation laws have not yet been developed.

In this work, a new method is proposed for obtaining conservation laws for oscillatory and wave processes in linear systems and media including those for which Noether's theorem is inapplicable (nonconservative, gyroscopic). It is assumed that the linear differential operator describing vibrations of a system is known. The notion of a Lagrangian adjoint system or medium is of key importance in the method. In contrast to available methods, this method enables one to construct the complete set of independent bilinear conservation laws. Below, the method is reported and its application is exemplified. Some of the presented conservation laws are obtained for the first time.

Let us consider a linear discrete or continuous mechanical system (or medium) whose oscillatory (or wave) motion is described by the ordinary differential operator of the order n:

$$l(y) = a_0(x)y^{(n)} + a_1(x)y^{(n-1)} \\ \ldots + a_{n-1}(x)y' + a_n(x)y. \quad (1)$$

Here, x is the coordinate or time varying in the interval (x_1, x_2), $y(x)$ is the function characterizing vibrations of the system (e.g., displacement), and prime and superscript (k) mean the first and kth derivatives, respectively. Operator (1) describes a wide class of vibration problems, including vibrations of discrete systems in the finite element method, wave processes in one-dimensional media (beams, bars), waves in two- and three-dimensional elastic wave guides such as shells, and waves in many other mechanical systems.

According to the theory of linear differential equations [7], the homogeneous equation

$$l(y) = 0 \quad (2)$$

has n linearly independent partial solutions $y_j(x)$ and its general solution is equal to their linear combination

$$y(x) = \sum_{j=1}^{n} c_j y_j(x), \quad (3)$$

where c_j are arbitrary constants.

A function P of solution (3) is called the integral of motion (conservation law) if it is independent of x over the interval under consideration:

$$P[y(x)] = \text{const}(x). \quad (4)$$

The number of independent integrals of motion is equal to the number n of constants c_j in general solution (3). The knowledge of all integrals of motion is equivalent to the knowledge of all solutions $y_j(x)$ of Eq. (2). However, the determination of integrals of motion and their analysis are often simpler and more convenient than the determination and analysis of solutions of the equation. When only some conservation laws are found, they facilitate the determination of missing solutions. This is the important role of conservation laws.

Blagonravov Institute of Mechanical Engineering, Russian Academy of Sciences,
M. Khariton'evskiĭ per. 4, Moscow, 101990 Russia
e-mail: bobrovni@orc.ru

1028-3358/04/4903-0171$26.00

The starting point of the method proposed in this work for constructing conservation laws is known Lagrange's identity [7]

$$l(y)\bar{z} - y\overline{l^*(z)} = P'(y, z). \quad (5)$$

Here,

$$l^*(z) = (-1)^n(\bar{a}_0 z)^{(n)} + (-1)^{n-1}(\bar{a}_1 z)^{(n-1)} + \ldots + \bar{a}_n z \quad (6)$$

is the differential operator adjoint to Eq. (1), and

$$P(y, z) = y^{(n-1)}a_0\bar{z} + y^{(n-2)}[-(a_0\bar{z})' + a_1\bar{z}] \ldots + y[(-1)^{n-1}(a_0\bar{z})^{(n-1)} + \ldots + a_{n-1}\bar{z}] \quad (7)$$

is the bilinear form containing derivatives of y and z up to the order $n - 1$. The overbar means complex conjugation. Details of the derivation of expressions for the adjoint operator and bilinear form can be found in [7]. Let $y(x)$ and $z(x)$ be solutions of Eq. (2) and the homogeneous adjoint equation

$$l^*(z) = 0, \quad (8)$$

respectively. Then, it follows from Lagrange identity (5) that bilinear form (7) is independent of x in the interval under consideration,

$$P_1(y, z) = P(y, z) = \text{const} \quad (9a)$$

and, therefore, is an integral of motion. Equality (9a) is called the first conservation law. It relates any solution of Eq. (2) with an arbitrary solution of adjoint equation (8). If the operator is self-adjoint, i.e., $l^* = l$, the first law is written as

$$P_1(y_j, y_k) = \text{const}, \quad (9b)$$

where y_j and y_k are two solutions of Eq. (2), or

$$P_1(y, y) = \text{const}, \quad (9c)$$

where y is any solution of Eq. (2), e.g., general solution (3).

Then, let us replace the solution y in Lagrange's identity by its derivative y'. Differentiating Eq. (2) with respect to x and substituting $l(y') = -l'(y)$ into Eq. (5), we obtain the second conservation law in the form

$$P_2(y, z) = P(y', z) + \int_{x_1}^{x} \bar{z}l'(y)dx = \text{const}. \quad (10)$$

Here, $l'(y)$ is operator (1), where coefficients $a_k(x)$ are replaced by $a_k'(x)$, and the term with the nth derivative in the bilinear form $P(y', z)$ is expressed in terms of lower order derivatives by using Eq. (2).

The third conservation law is obtained similarly by replacing the solution in Lagrange identity (5) by its derivative y'':

$$P_3(y, z) = P(y'', z) + \int_{x_1}^{x} \bar{z}[2l'(y') + l''(y)]dx = \text{const}. \quad (11)$$

Here, the derivatives of y whose orders are higher than $n-1$ in $P(y'', z)$ must be expressed from Eq. (2). Repeating this process, i.e., replacing y by $y^{(k)}$ in Lagrange's identity, one can obtain all n independent conservation laws. The first conservation law given by Eq. (9) is well known. At the same time, as far as I know, the remaining conservation laws including, Eqs. (10) and (11), are obtained for the first time.

For systems and media whose vibrations are described by differential equations with constant coefficients, the conservation laws obtained above are reduced to a particularly simple form. In this case, all terms involving integrals are equal to zero, and the system of independent laws takes the form

$$P_k(y, z) = P(y^{(k-1)}, z) = \text{const}, \quad k = 1, 2, \ldots, n. \quad (12)$$

All other bilinear conservation laws, including those obtained for $k > n$, are combinations of relations (12).

One of the disadvantages of the relations obtained above is the requirement that the coefficients of Eq. (1) be differentiable. This requirement can be replaced by the condition of the summability of coefficients. An arbitrary linear self-adjoint differential operator with variable coefficients has the form

$$l(x) = (-1)^n[a_0(x)y^{(n)}]^{(n)} + (-1)^{n-1} \times [a_1(x)y^{(n-1)}]^{(n-1)} + \ldots + a_n(x)y, \quad (13)$$

where the functions $a_k(x)$ are real. Replacing ordinary derivatives $y^{(k)}$ by so-called quasi-derivatives $y^{[k]}$ defined as [7]

$$y^{[1]} = y^{(1)}; \ldots; y^{[n-1]} = y^{(n-1)}; \quad y^{[n]} = a_0 y^{(n)}; \quad y^{[n+k]} = a_k y^{(n-k)} - (y^{[n+k-1]})' \quad (14)$$

and repeating the above procedure, we easily obtain $2n$ integrals of motion, which are similar to Eqs. (10) and (11) and are meaningful for coefficients $a_k(x)$ that are measurable in a given interval and summable in each of its closed finite subintervals. In particular, they are valid for discontinuous coefficients corresponding to wave processes in layered media (see example 3 below).

The proposed method is also applicable to systems of N linear equations for N unknown functions, i.e., to

equations similar to Eq. (1), where y is the N-component vector function and $a_k(x)$ are $N \times N$ matrices. In this case, it is only necessary to replace complex conjugation by Hermitian conjugation and the ordinary product by the scalar product of vector functions (see example 2).

For illustration, let us apply the above results to some simple systems.

Example 1. Free vibrations of a linear damping system with one degree of freedom are described by the operator

$$l(y) = m\ddot{y} + b\dot{y} + ky = 0, \quad (15)$$

where m is the mass, b is the damping coefficient, k is the elasticity, and the point means the time derivative. The adjoint operator

$$l^*(z) = m\ddot{z} - b\dot{z} + kz \quad (16)$$

differs from direct operator (15) by the sign of the damping coefficient and, therefore, describes an active system with negative losses. Two independent conservation laws (12) for this system have the form

$$P_1 = m(\dot{y}\bar{z} - y\dot{\bar{z}}) + by\bar{z} = \text{const}, \quad (17)$$

$$P_2 = m\dot{y}\dot{\bar{z}} + ky\bar{z} = \text{const}. \quad (18)$$

The latter relation is the conservation law for the total cross energy of oscillatory processes in direct and adjoint systems with one degree of freedom. In the absence of losses ($b = 0$), $l^* = l$ and relation (18) at $z = y$ takes the form of the ordinary energy conservation law in a conservative system. The physical meaning of relation (17) is not clear. Conservation law (18) was obtained by many authors, e.g., in [3–5], whereas I have not seen law (17) in previous works.

Let us show that constants in conservation laws (17) and (18) are combinations of arbitrary constants A and B appearing in the general solution of Eq. (15):

$$y(t) = e^{-\beta t}(A\cos\omega t + B\sin\omega t),$$

where $\omega^2 = \frac{k}{m} - \beta^2$ and $\beta = \frac{b}{2m}$. Substituting the solution to adjoint equation (16) in the form $z_1(t) = e^{\beta t}\cos\omega t$ into Eqs. (17) and (18), we obtain

$$P_1 = m\omega B, \quad P_2 = m\omega(\omega A + \beta B).$$

For the second independent solution $z_2(t) = e^{\beta t}\sin\omega t$ of the adjoint equation, we obtain

$$P_1 = -m\omega A, \quad P_2 = m\omega(\omega B - \beta A).$$

Example 2. The natural vibrations of the linear damped system with N degrees of freedom with time-independent parameters are described by the system of N equations

$$l(u) = M\ddot{u} + B\dot{u} + Ku = 0. \quad (19)$$

Here, $u = [u_1, u_2, \ldots, u_N]^T$ is the displacement vector function, where the superscript T means transposition, and M, B, and K are real $N \times N$ inertia, damping, and stiffness matrices, respectively. These matrices are generally asymmetric, because it is assumed that the system under consideration can involve gyroscopic elements in addition to losses and Coriolis and Lorentz forces are taken into account [8]. Using the usual definition $v^*u = u_1\bar{v}_1 + u_2\bar{v}_2 + \ldots + u_N\bar{v}_N$ for the scalar product of two vector functions u and $v = [v_1, v_2, \ldots, v_N]^T$, where v^* is the vector function Hermitian conjugate to v, we find from Lagrange's identity that the operator adjoint to operator (19) has the form

$$l^*(v) = M^*\ddot{v} - B^*\dot{v} + K^*v.$$

Similar to the system with one degree of freedom (example 1), the adjoint system with N degrees of freedom is active, i.e., has negative damping. In this case, conservation laws (12) are written as

$$P_1 = v^*M\dot{u} - \dot{v}^*Mu + v^*Bu = \text{const}, \quad (20)$$

$$P_2 = \dot{v}^*M\dot{u} + v^*Ku = \text{const}. \quad (21)$$

The latter relation is the conservation law for the total cross energy of vibrations of two, direct and adjoint, systems. The complete system of conservation laws is obtained from Eqs. (20) and (21) by substituting some N independent partial solutions of the adjoint equation $l^*(v) = 0$.

Example 3. Let us consider a system with one degree of freedom without losses and with time-dependent mass $m(t)$ and stiffness $k(t)$. Its free vibrations are described by the self-adjoint differential operator

$$l(y) = \frac{d}{dt}[m(t)\dot{y}] + k(t)y, \quad (22)$$

which has form (13). In the general case, where $m(t)$ and $k(t)$ are discontinuous (i.e., changes in mass and stiffness can be jumplike), the quasi-derivative technique should be used. Setting

$$y^{[0]} = y, \quad y^{[1]} = -m\dot{y}, \quad y^{[2]} = ky - \frac{dy^{[1]}}{dt} = l(y)$$

in accordance with Eq. (14), it is easy to obtain the bilinear form

$$P(y, z) = y\bar{z}^{[1]} - y^{[1]}\bar{z}$$

and two conservation laws

$$P_1 = P(y, z) = m(t)(\dot{y}\bar{z} - y\dot{\bar{z}}) = \text{const}, \quad (23)$$

$$P_2 = P(y^{[1]}, z) - \int_{t_0}^{t} l(y^{[1]})\bar{z}\,dt = \text{const}. \quad (24a)$$

Simple transformations reduce the latter law to the form

$$P_2 = -m(m\dot{y}\bar{z} + ky\bar{z}) + \int_{t_0}^{t} \frac{d}{dt}(mk)y\bar{z}dt = \text{const.} \quad (24b)$$

For example, let mass and stiffness vary linear with time; i.e., $m(t) = m_0 t$ and $k(t) = k_0 t$. In this case, the general solution of the equation $l(y) = 0$ is written as

$$y(t) = AJ_0(\omega t) + BN_0(\omega t), \quad (25)$$

where J_0 and N_0 are the zeroth order Bessel functions, $\omega^2 = \frac{k_0}{m_0}$, and A and B are the vibration amplitudes. It is easy to check that relations (23) and (24) are integrals of oscillatory motion (25) for both $z = y$ and $z_1 = J_0$ and $z_2 = N_0$ and their right-hand sides are combinations of the amplitudes A and B.

ACKNOWLEDGMENTS

This work was supported in part by the Council of the President of the Russian Federation for Support of Young Russian Scientists and Leading Scientific Schools (project no. NSh-2247.2003.1).

REFERENCES

1. C. Lanczos, *The Variational Principles of Mechanics*, 4th ed. (Dover, New York, 1986; Mir, Moscow, 1965).
2. E. Noether, Nachr. Ges. Wiss. Goettingen **2**, 235 (1918).
3. P. M. Morse and H. Feshbach, *Methods of Theoretical Physics* (McGraw-Hill, New York, 1953; Inostrannaya Literatura, Moscow, 1958), Vol. 1.
4. L. Y. Bahar and H. G. Kwatny, J. Sound Vib. **102**, 551 (1985).
5. T. Honein, N. Chien, and G. Herrmann, Phys. Lett. A **155**, 223 (1991).
6. A. G. Kotousov and N. A. Makhutov, Dokl. Akad. Nauk **351**, 476 (1996) [Phys. Dokl. **41**, 602 (1996)].
7. M. A. Naimark, *Linear Differential Operators*, 2nd ed. (Nauka, Moscow, 1969; Ungar, New York, 1967).
8. A. Pippard, *The Physics of Vibration*, 2nd ed. (Cambridge Univ. Press, New York, 1989; Vysshaya Shkola, Moscow, 1985).

Translated by R. Tyapaev

Doklady Physics, Vol. 49, No. 3, 2004, pp. 175–178. Translated from Doklady Akademii Nauk, Vol. 395, No. 1, 2004, pp. 47–50.

MECHANICS

Theory of Metal Surface Destruction under the Action of Laser Radiation

O. B. Kovalev, A. M. Orishich,
Corresponding Member of the RAS V. M. Fomin, and A. V. Zaytsev

Received October 27, 2003

The efficiency of technologies related to the laser processing of materials is closely associated with processes of radiation interaction with a substance in the narrow channel of the laser cut. In this paper, the problem of describing the shape of a surface formed as a result of the laser cutting of metals by an intense radiation flux is studied. The effect of the Gaussian beam polarization on the radiation absorption factor with allowance for the spatial orientation of the beam incidence plane is analyzed. We show for the first time that it is most efficient to use the elliptic polarization of the radiation, which possesses a quite certain ratio of the ellipse semiaxes and is oriented along the beam direction. A calculation model for the laser cut surface is proposed. The model takes into account the multiple reflection of the focused laser radiation in the cut channel.

At present, new technology for the laser cutting of thick materials (with a thickness of 20–30 mm) has appeared [1, 2]. This fact is closely related to the development of intense industrial lasers (CO_2 lasers and excimer lasers) of permanent and periodic action, whose power reaches 10 kW. In this connection, more adequate mathematical methods for describing the interaction of laser radiation with metals are now necessary. In the available literature [3, 4], problems related to the effect of the radiation polarization on the shape and depth of the cut have not been adequately explored. Mathematical models capable of studying the cutting process with allowance for the multiple reflection of radiation, which is extremely important for modeling the cutting of thick materials, are absent.

The traditional setting of the problem on the motion of a free surface of a material under the action of laser radiation is reduced to the equation of kinematic consistency of surface points [3, 4]:

$$\frac{\partial z_m}{\partial t} - V_c\frac{\partial z_m}{\partial x} = -V_n\sqrt{1+\left(\frac{\partial z_m}{\partial x}\right)^2+\left(\frac{\partial z_m}{\partial y}\right)^2}, \quad (1)$$

$$\begin{aligned}\frac{\partial z_m}{\partial x}(-a, y, t) &= \frac{\partial z_m}{\partial x}(a, y, t) = 0, \quad -b \le y \le b,\\ \frac{\partial z_m}{\partial y}(x, -b, t) &= \frac{\partial z_m}{\partial y}(x, b, t) = 0, \quad -a \le x \le a,\end{aligned} \quad (2)$$

$$z_m(x, y, 0) = 0, \quad (3)$$

where $z = z_m(x, y, t)$ is the equation for the free surface of a material, V_c is the cutting speed, and a and b are the plate dimensions.

The normal component V_n of the displacement velocity for points of the surface is represented by the ratio of the radiation power density Q absorbed by the surface element and of the energy spent for destroying the material:

$$V_n = \frac{Q}{\rho_m H_m + c_s^0\rho_s^0(T_m - T_0)}, \quad Q = AI(x, y, z)\cos\gamma. \quad (4)$$

Here, A is the absorption factor; $I(x, y, z)$ is the radiation intensity density; γ is the angle of incidence of the beam; x, y, z are the spatial coordinates; ρ_m is the material density corresponding to the melting temperature T_m; H_m is the melting specific heat; and ρ_s^0 and c_s^0 are the density and specific heat capacity of the material at the initial temperature T_0.

We consider a constant acting radiation of a CO_2 laser with a wavelength of $\lambda_0 = 10.6$ μm, which is directed along the OZ axis of the Cartesian coordinate system. The radiation intensity density is described by

Institute of Theoretical and Applied Mechanics, Siberian Division, Russian Academy of Sciences, ul. Institutskaya 4/1, Novosibirsk, 630090 Russia
e-mail: kovalev@itam.nsc.ru; orishich@itam.nsc.ru; fomin@itam.nsc.ru; zaitsev@gorodok.net

1028-3358/04/4903-0175$26.00 © 2004 MAIK “Nauka/Interperiodica”

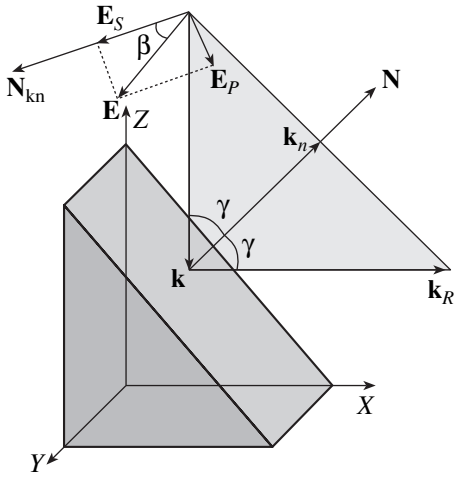

Fig. 1. Scheme of interaction of laser radiation with a material surface element.

the Gaussian distribution, which corresponds to the TEM_{00} mode [5]:

$$I(x, y, z) = \frac{2W}{\pi\omega_z^2}\exp\left(-\frac{2r^2}{\omega_z^2}\right),$$
$$\omega_z = \sqrt{\omega_0^2 + \left(\frac{(z - z_f)\lambda_0}{\pi\omega_0}\right)^2}, \quad r = \sqrt{x^2 + y^2}, \tag{5}$$

where W is the radiation power; z_f is the distance between the focal surface and the plane $z = 0$; and ω_0 is the beam radius in the focal plane.

We now analyze the effect of the radiation polarization on the absorption factor. We consider a surface element inclined with respect to the *OX* axis of the Cartesian coordinate system (Fig. 1). The incidence plane is formed by the wave vectors $\mathbf{k}$ and $\mathbf{k}_R$ of the incident and reflected radiations and by the unit vector of the normal $\mathbf{N}$ to the surface. The vector $\mathbf{E}$ of the electric-field intensity is decomposed into two components. The components $\mathbf{E}_p$ lying in the incidence plane and $\mathbf{E}_s$ oriented normally to the incidence plane are put in correspondence to the reflection coefficients R_p and R_s, respectively. Let β be the angle between the vector $\mathbf{E}$ and a normal $\mathbf{N}_{kn}$ to the incidence plane. In accordance with [6], we write the expression for the absorption factor in the form

$$A(\beta, \gamma) = 1 - R(\beta, \gamma)$$
$$= 1 - \cos^2\beta \cdot R_s - \sin^2\beta \cdot R_p. \tag{6}$$

We consider the case of the elliptic polarization of the beam when the end of the vector $\mathbf{E}$, which lies in the (X, Y) plane, describes an ellipse with the semiaxes a and b directed along the *OX* and *OY* axes, respectively. In this case, the relationship $a^2 + b^2 = 1$ is valid. We can represent the absorption factor as a sum $A = a^2A_x + b^2A_y$, where A_x, A_y are the absorption factors for the radiation linearly polarized along the *OX* and *OY* axes, respectively. According to (6), we can write

$$A_x(\gamma, \beta_x) = 1 - R_s(\gamma)\cos^2\beta_x - R_p(\gamma)\sin^2\beta_x,$$
$$A_y(\gamma, \beta_y) = 1 - R_s(\gamma)\cos^2\beta_y - R_p(\gamma)\sin^2\beta_y, \tag{7}$$

where β_x and β_y are the angles between the normal $\mathbf{N}_{kn}$ to the incidence plane and *OX* and *OY* axes, respectively. For the angles β_x and β_y, the equalities

$$\cos^2\beta_x = \left(\left(\frac{\mathbf{k}}{|\mathbf{k}|} \times \mathbf{N}\right) \cdot \mathbf{e}_x\right)^2 = (\mathbf{N}, \mathbf{e}_y)^2 = N_y^2,$$
$$\cos^2\beta_y = \left(\left(\frac{\mathbf{k}}{|\mathbf{k}|} \times \mathbf{N}\right) \cdot \mathbf{e}_y\right)^2 = (\mathbf{N}, \mathbf{e}_x)^2 = N_x^2 \tag{8}$$

occur. Substituting relationships (8) into formulas (7), we obtain the expression for the absorption factor A in the case of elliptic polarization:

$$A(\gamma, N_x, N_y) = 1 - R_S(\gamma)(a^2N_y^2 + b^2N_x^2)$$
$$- R_P(\gamma)(a^2(1 - N_y^2) + b^2(1 - N_x^2)). \tag{9}$$

In accordance with expression (9), the radiation absorption factor is strongly dependent on the spatial orientation of both the vector of a normal to the surface and the radiation polarization characterized by the ratio $\xi = \frac{b}{a}$ of the semiaxes. For $\xi = 0$, we deal with the linear *P* wave, and for $\xi = 1$, we have the circular polarization. For $\xi = \infty$, we deal with the linear *S* wave, whereas for all other values of ξ, we have the elliptic polarization. Equations (1)–(5), (9) were solved numerically by the pseudo-transient method using the explicit finite-difference scheme. In the case of cutting by the *S*-polarization beam, when the electric-field vector $\mathbf{E}$ is perpendicular to the direction of field motion, the maximum of the radiation absorption corresponds to the side walls. In this case, the absorption factor on the cut front is low; therefore, the ultimate cutting parameters also are small, and a broad cut with a smooth surface is realized since the maximal density of the power absorbed corresponds to the beam center. In the case of cutting by the *P*-polarization beam with the vector *E* parallel to the beam motion, the maximal density of the power being absorbed corresponds to the cut front, where the radiation is incident at the angle of about 85°–87°. In this case, a narrow cut is formed because the major part of the radiation does not penetrate deep into the cut being reflected from its front.

Figure 2 exhibits the results of a series of numerical experiments aimed at the determination of the maximal cut depth L as a function of the parameter ξ. The values of the beam power $W = 600$ W, of the speed $V_c = 44$ mm s^{-1}, and geometric characteristics of Gaussian beam (5) ($\omega_0 = 100$ μm, $z_f = 0$) remained constant

throughout the calculations. There exists a pronounced maximum (L = 3.8 mm at ξ = 0.75) in the curve $L(\xi)$. This maximum corresponds to an elliptically polarized beam with ellipticity oriented along the beam's direction of motion. At present, in the literature and among specialists in the field of the laser cutting of materials, there exists the common opinion on the highest efficiency of using radiation with the linear polarization (ξ = 0) oriented along the cut direction [7]. The results of our theoretical studies presented in this paper have shown for the first time that the elliptically polarized radiation with a certain ratio of the semiaxes $\left(\frac{b}{a} = 0.75\right)$ and oriented along the beam direction can possess the maximum efficiency.

We now analyze the effect of the multiple reflection of radiation on the cut depth. For the majority of materials, the absorption factor is small (A = 0.01–0.5). In this case, the radiation of reflected waves can play an important role. This is especially true for deep and thin cuts, when the multiple repeated reflections mainly contribute to the energy being absorbed. The analysis of laser cutting performed in [1, 2] shows that the multiple reflections of radiation occur, while it propagates inside the cut or a cavity, especially in the case of thick (on the order of 10 mm and more) materials. Existing methods of modeling the interaction of laser radiation with metals are based on approximation (1)–(5), in which only single radiation absorption is taken into account. It is well known [5] that focused laser radiation propagating in the form of electromagnetic oscillations has the shape of Gaussian beam (5), which is a partial solution to the Maxwell equations. In the case of reflection of the Gaussian beam from an arbitrary surface, the beam shape can be considerably changed, the wave properties of the radiation being important in this case. Correctly setting the problem on the interaction of electromagnetic radiation with an arbitrary metal surface is rather complicated, since it requires solving complete electrodynamics equations.

The physical model for calculating the surface shape which is proposed by the authors and takes into account the multiple reflection of radiation differs from the conventional model described by Eqs. (1)–(5). The difference consists in the fact that the normal component V_n of the displacement velocity for points of the surface is expressed in terms of the sum of the total multiply absorbed power Q at each point of the surface. In order to calculate the function $Q(x, y, z_m(x, y, t))$, the trajectory method is used. This method consists in the fact that the density distribution of Gaussian beam intensity (5) is subject to finite-element discretization. Each of the elements represents a light ray that contains the radiation energy $dE_{k_i} = I(x_{k_i}, y_{k_i}, z_{k_i})dx\,dy$ and has the coordinates $x_{k_i}, y_{k_i}, z_{k_i}$ and the velocity $\mathbf{V}_{k_i}$ along

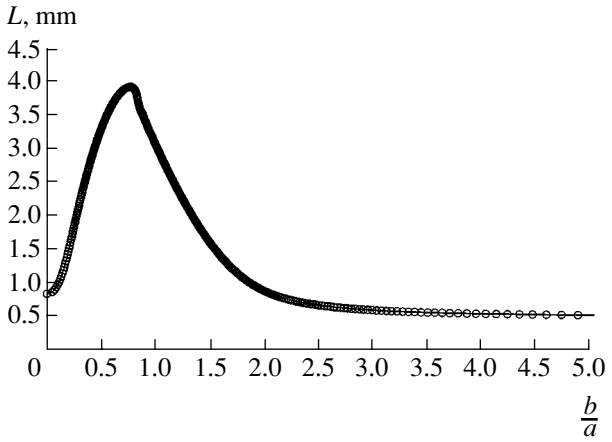

Fig. 2. Effect of the radiation polarization (ratio of the semiaxes $\xi = \frac{b}{a}$) on the maximal cutting depth L.

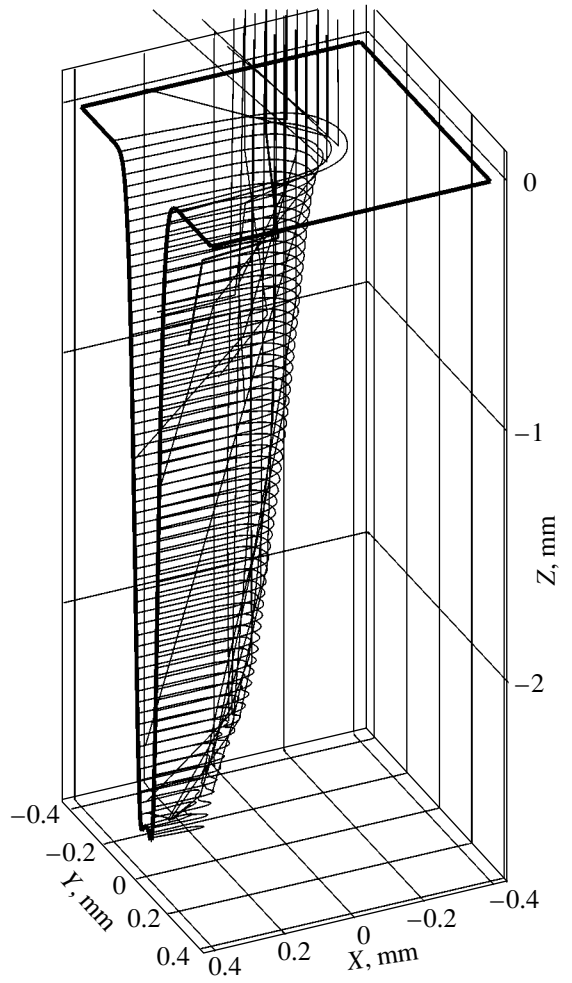

Fig. 3. Radiation propagation in the cut channel in the case of the laser cutting of metals. The power is W = 1 kW, the cutting speed is V_c = 0.17 m s^{-1}, the distance of the focus depth is z_f = 0.25 mm, and the radius of the beam focal plane is ω_0 = 100 μm.

the direction of the wave vector $\mathbf{k}_i$. After the interaction with the surface has occurred, the trajectory of each light ray changes its direction in accordance with the geometric-optics law (i.e., the angle of incidence equals the reflection angle). In this case, the radiation energy decreases by the value of energy absorbed by the metal surface.

Figure 3 presents the spatial pattern of the laser radiation propagation in the cut channel of a metallic plate. The horizontal level lines correspond to the contour of the surface being obtained. As is seen, the light rays are multiply reflected from the internal channel surface. Taking into account the moderate absorption factor of metals (e.g., the maximum value for stainless steel reaches $A \approx 0.5$), the multiple-reflection model proposed makes it possible to describe the process of the energy transfer deep into the channel and, hence, to more correctly model its structure, especially in the case of cutting thick materials.

REFERENCES

1. A. M. Orishich, V. B. Shulyat'ev, and S. A. Konstantinov, in *Proceedings of the 7th International Conference "Lasers and Laser-Information Technologies: Fundamental Problems and Applications," Vladimir–Suzdal', 2001*, p. 54.
2. Yu. V. Afonin, A. P. Golyshev, and A. I. Ivanchenko, Proc. SPIE **4900**, 929 (2002).
3. G. P. Cherepanov and A. G. Cherepanov, Fiz. Khim. Obrab. Mater., No. 2, 133 (1990).
4. A. V. Nesterov and V. G. Niz'ev, Izv. Ross. Akad. Nauk, Ser. Fiz. **63**, 2039 (1999).
5. A. N. Oraevskiĭ, Proc. (Tr.) P.N. Lebedev Phys. Inst. **187**, 3 (1988).
6. M. Born and E. Wolf, *Principles of Optics* (Pergamon Press, Oxford, 1969; Nauka, Moscow, 1973).
7. A. G. Grigor'yants, *Principles of Laser Processing of Materials* (Mashinostroenie, Moscow, 1989).

Translated by G. Merzon

Doklady Physics, Vol. 49, No. 3, 2004, pp. 179–182. Translated from Doklady Akademii Nauk, Vol. 395, No. 1, 2004, pp. 51–54.

MECHANICS

Effect of Parametric Dissipative Fluctuation Forces on the Motion of the Earth's Pole

Yu. G. Markov* and I. N. Sinitsyn**

Presented by Academician V.V. Kozlov November 25, 2003

Received November 25, 2003

Geophysical observations and measurements concerning large-scale motions (Rossby waves) in the atmosphere and ocean, as well as friction effects in Earth tides, testify that friction forces are much smaller than, e.g., Coriolis forces. Nevertheless, friction, as well as energy dissipation due to numerous friction effects occurring in the Earth's crust and ocean, accompanying continental drift and convective motion in the Earth's mantle, etc., cannot be disregarded [1–3].

Allowance for frictional torques is especially important when studying, e.g., vibration dumping in geodynamic processes. When dealing with such a fine problem as the effect of frictional torques in geodynamic processes, one should remember that the age of the Earth is important in all these processes. It is known that dissipative processes in the Earth are synchronized with the cycles in the Earth–Moon–Sun system due to the billion-year evolution of the solar system.

Continuing works [4–6] devoted to spectral correlation models of the motion of the pole of the deformable Earth, we take into account parametric dissipative fluctuation forces.

1. The notation and assumptions in this paper are the same as in [5, 6]. The projection r_t of the instantaneous angular velocity of the Earth on the axis of its rotation is assumed constant: $r_t = r_n = \text{const}$. The projections of the instantaneous angular velocity on the Earth's axes are denoted by p_t and q_t ($p_t, q_t \ll r_0$). We take the following model for the specific moments of dissipative fluctuation forces:

$$M_1^{\mathrm{df}} A^{*-1} = V_{1t} - (D_1^* + D_1^0 + D_1' V_{1t}) p_t - (D_{12}^* + D_{12}^0 + D_{12}' V_{2t}) q_t; \quad (1)$$

$$M_2^{\mathrm{df}} B^{*-1} = V_{2t} - (D_{21}^* + D_{21}^0 + D_{21}' V_{1t}) p_t - (D_2^* + D_2^0 + D_2' V_{2t}) q_t. \quad (2)$$

Here, $D_{1,2}^*$ and $D_{1,2}^0$ ($D_{1,2}'$) are the coefficients determining the regular and irregular (constant and variable) components of the specific moments of dissipative forces, respectively; $D_{12,21}^*$ and $D_{12,21}^0$ ($D_{12,21}'$) are the corresponding anisotropy parameters for these moments; and V_{1t} and V_{2t} are Gaussian broadband processes similar to white noise.

Following [5, 6], the axial and centrifugal moments of the deformable Earth are taken into account by introducing effective daily humps and spikes. Moreover, the moments of gravitational forces of the Sun are included. According to [5, 6] and Eqs. (1) and (2), the equations of motion of the Earth's pole (in the Stratonovich sense) have the form

$$\dot{p}_t + N_* q_t = \mathcal{P}_1 + \mathcal{P}_2 V, \quad p_{t_0} = p_0; \quad (3)$$

$$\dot{q}_t - N_* p_t = \mathcal{Q}_1 + \mathcal{Q}_2 V, \quad q_{t_0} = q_0, \quad (4)$$

where

$$\mathcal{P}_1 = \mathcal{P}_{10} + \mathcal{P}_{11}\cos\omega_* t + \mathcal{P}_{12}\cos 2\omega_* t; \quad (5)$$

$$\mathcal{Q}_1 = \mathcal{Q}_{10} + \mathcal{Q}_{11}\cos\omega_* t + \mathcal{Q}_{12}\cos 2\omega_* t; \quad (6)$$

$$\begin{aligned}\mathcal{P}_{10} &= -\frac{3}{2}u_4\omega_*^2\left(1-\frac{3}{2}b_1^2\right) - \frac{3}{2}u_6\omega_*^2\left(1-\frac{b_1}{2}\right) \\ &\quad -\frac{3}{2}u_{11}\omega_*^2\left(1-\frac{b_1^2}{2}\right) - u_4 r_*^2, \\ \mathcal{Q}_{10} &= \frac{3}{2}u_7\omega_*^2\left(1-\frac{b_1}{2}\right) + \frac{3}{2}u_8\omega_*^2\left(1-\frac{3b_1^2}{2}\right) \\ &\quad -\frac{3}{2}u_{10}\omega_*^2\left(1-\frac{b_1^2}{2}\right) + u_8 r_*^2;\end{aligned} \quad (7)$$

$$\begin{aligned}\mathcal{P}_{11} &= 3u_1 b\omega_*^2 + \frac{3}{2}u_{13}b\omega_*^2, \\ \mathcal{Q}_{11} &= -3u_2 b\omega_*^2 - 3u_{14}b\omega_*^2;\end{aligned} \quad (8)$$

* *Moscow Aviation Institute (Technical University), Volokolamskoe sh. 4, Moscow, 125080 Russia*

** *Institute for Problems of Informatics, Russian Academy of Sciences, ul. Vavilova 30/6, Moscow, 117900 Russia*

1028-3358/04/4903-0179$26.00 © 2004 MAIK "Nauka/Interperiodica"

$$\mathcal{P}_{12} = \frac{9}{4}u_4 b_1^2\omega_*^2 + \frac{3}{4}u_6 b_1^2\omega_*^2 + \frac{3}{4}u_{11}b_1^2\omega_*^2,$$
$$\mathcal{Q}_{12} = -\frac{3}{4}u_7 b_1^2\omega_*^2 - \frac{9}{4}u_8 b_1^2\omega_*^2 + \frac{3}{4}u_{10}b_1^2\omega_*^2; \quad (9)$$

$$\mathcal{P}_2 = \mathcal{P}_2(p_t, q_t, \mathcal{D}, \mathbf{V}) = V_{1t} - (D_1^* + D_1^0 + D_1'V_{1t})p_t - (D_{12}^* + D_{12}^0 + D_{12}'V_{2t})q_t; \quad (10)$$

$$\mathcal{Q}_2 = \mathcal{Q}_2(p_t, q_t, \mathcal{D}, \mathbf{V}) = V_{2t} - (D_{21}^* + D_{21}^0 + D_{21}'V_{1t})p_t - (D_2^* + D_2^0 + D_2'V_{2t})q_t. \quad (11)$$

Here, $N_* = (C^* - B^*)A^{*-1}\omega_*$ is the Chandler frequency; ω_* corresponds to the annual period ($r_* = 365\omega_*$); the parameter vector $\mathbf{u} = [u_1 \ldots u_{15}]^T$ is the same as in [5]; $b_1 \approx b$, $0.4 \le b \le \frac{4}{3}\pi^{-1}$, $\mathcal{D} = \{D_i^*, D_i^0, D_i', D_{ij}'\}$, $i, j = 1, 2$; and $\mathbf{V} = [V_{1t}V_{2t}]^T$. Terms involving the squares and products of $\mathbf{u}$, p_t, and q_t are omitted in the functions $\mathcal{P}_{1,2}$ and $\mathcal{Q}_{1,2}$ [5, 6].

Equations (3) and (4) represent a two-dimensional linear stochastic system involving two parametric random processes of the form

$$\dot{Y} = a_0 + (a + A^0)Y + \left(b_0 + \sum_{h=1}^{2} b_h Y_h\right)V, \quad Y(t_0) = Y_0. \quad (12)$$

Here,

$$\mathbf{Y} = [Y_1Y_2]^T, \quad Y_1 = p_t, \quad Y_2 = q_t, \quad \mathbf{V} = [V_{1t}V_{2t}]^T; \quad (13)$$

$$a_0 = \begin{bmatrix}\mathcal{P}_1\\ \mathcal{Q}_1\end{bmatrix}, \quad a = \begin{bmatrix}-D_1^* & -(N_* + D_{12}^*)\\ N_* - D_{21}^* & -D_2^*\end{bmatrix}, \quad A^0 = \begin{bmatrix}-D_1^* & -D_{12}^0\\ -D_{21}^0 & -D_2^0\end{bmatrix}; \quad (14)$$

$$b_0 = \begin{bmatrix}1 & 0\\ 0 & 1\end{bmatrix}, \quad b_1 = \begin{bmatrix}-D_1' & 0\\ -D_{21}' & 0\end{bmatrix}, \quad b_2 = \begin{bmatrix}0 & -D_{12}'\\ 0 & -D_2'\end{bmatrix}. \quad (15)$$

Following [5, 6], we reduce Eq. (12) to the stochastic differential equation in the Ito sense:

$$\dot{Y} = \bar{a}_0 + (\bar{a} + A^0)Y + \left(b_0 + \sum_{h=1}^{2} b_h Y_h\right)V. \quad (16)$$

Here,

$$\bar{a}_0 = a_0 + \Delta a, \quad \bar{a} = a + \Delta a; \quad (17)$$

$$\Delta a_0 = -\frac{1}{2}\begin{bmatrix}D_1'\nu_{11} + D_{12}'\nu_{22}\\ D_2'\nu_{22} + D_{21}'\nu_{11}\end{bmatrix}, \quad \Delta a = \begin{bmatrix}\Delta D_1 & \Delta D_{12}\\ \Delta D_{21} & \Delta D_2\end{bmatrix}; \quad (18)$$

$$\Delta D_1 = -\frac{1}{2}(D_1'^2\nu_{11} + D_{12}'D_{21}'\nu_{12}),$$
$$\Delta D_2 = -\frac{1}{2}(D_2'^2\nu_{22} + D_{12}'D_{21}'\nu_{12}),$$
$$\Delta D_{12} = -\frac{1}{2}(D_1'D_{12}'\nu_{12} + D_2'D_{12}'\nu_{22}),$$
$$\Delta D_{21} = -\frac{1}{2}(D_1'D_{21}'\nu_{11} + D_2'D_{21}'\nu_{12}). \quad (19)$$

2. In the simplest model of stochastic dissipation, $D_{1,2}' = 0$, $D_{12,21}' = 0$, and $D_{1,2}^0$ are the independent Gaussian random variables with zero mathematical expectation and standard deviations $\mathcal{D}^0 = \{\sigma_{D_1}, \sigma_{D_2}, \sigma_{D_{12}}, \sigma_{D_{21}}\}$. In this case, the conditional expectations and spectral correlation characteristics for a given matrix A^0,

$$m_t(A^0), \quad s(\omega, A^0), \quad K_t(A^0), \quad K_{t_1t_2}(A^0) \quad (20)$$

are determined by Eqs. (17), (18), and (20) given in [6], and the transfer and weighting functions are defined by Eqs. (26) and (29) for $\alpha - a$ and $\alpha_0 = a_0$ [see Eqs. (14) above]. Averaging relations (20) over the matrix A^0, we obtain the unconditional characteristics

$$Mm_t(\mathcal{D}^0), \quad Dm_t(\mathcal{D}^0), \quad MK_t(\mathcal{D}^0), \quad DK_t(\mathcal{D}^0), \quad Ms(\omega, \mathcal{D}^0), \quad Ds(\omega, \mathcal{D}^0), \quad MK_{t_1t_2}(\mathcal{D}^0), \quad DK_{t_1t_2}(\mathcal{D}^0), \quad (21)$$

where M and D mean the mathematical expectation and standard deviation, respectively.

3. We now consider the variable components of the irregular dissipation factors. According to Eq. (12), the

equations for the expectation m_t, covariance matrix K_t, and covariance function $K(t_1, t_2)$ have the form [7, 8]

$$\dot{m}_t = am_t + a_0, \quad m_{t_0} = m_0; \tag{22}$$

$$\dot{K}_t = \bar{a}K_t + K_t\bar{a}^{\mathrm{T}} + b_0\nu b_0^{\mathrm{T}} + \sum_{h=1}^{2}(b_h\nu b_0^{\mathrm{T}} + b_0\nu b_h^{\mathrm{T}})m_h + \sum_{l,h=1}^{2}\sum^{2} b_h\nu b_l^{\mathrm{T}}(m_h m_l + k_{hl}), \quad K(t_0) = K_0; \tag{23}$$

$$\frac{\partial K(t_1, t_2)}{\partial t_2} = K(t_1, t_2)\bar{a}(t_2)^{\mathrm{T}}, \quad K_{t_1, t_1} = K_{t_1}, \text{ for } t_1 < t_2; \quad K(t_1, t_2) = K(t_2, t_1)^{\mathrm{T}}, \text{ for } t_2 < t_1. \tag{24}$$

If intensities are constant, i.e., $\nu = \nu_0$, the expectations $\langle m_t\rangle$ and covariance matrix $\langle K_t\rangle$, which are averaged over the period $2\pi\omega_*^{-1}$ under steady-state conditions when $\langle m_t\rangle^{\cdot} = 0$ and $\langle K_t\rangle^{\cdot} = 0$, satisfy the relations

$$a\langle m_t\rangle + \langle a_0\rangle = 0; \tag{25}$$

$$\bar{a}\langle K_t\rangle + \langle K_t\rangle\bar{a}^{\mathrm{T}} + b_0\nu_0 b_0^{\mathrm{T}} + \sum_{h=1}^{2}(b_h\nu_0 b_0^{\mathrm{T}} + b_0\nu_0 b_h^{\mathrm{T}})\langle m_h\rangle + \sum_{l,h=1}^{2}\sum^{2} b_h\nu_0 b_l^{\mathrm{T}}(\langle m_h m_l\rangle + \langle k_{hl}\rangle) = 0. \tag{26}$$

According to Eq. (24), the function $k(\tau) = \langle K(t_1, t_1 + \tau)\rangle$ satisfies the equation

$$\frac{dk(\tau)}{d\tau} = k(\tau)\bar{a}^{\mathrm{T}}. \tag{27}$$

4. Equations (22) for the expectations $m_t = [m_1 m_2]^{\mathrm{T}}$ are separated from the equations for the correlation characteristics and are written in the form

$$\dot{m}_1 = -D_1^e m_1 - N_{1*}^e m_2 + \mathcal{P}_t^e; \tag{28}$$

$$\dot{m}_2 = -N_{2*}^e m_1 - D_2^e m_2 + \mathcal{Q}_t^e; \tag{29}$$

$$D_1^e = D_1^* - \frac{1}{2}(D_1'^2\nu_{11} + D_{12}'D_{21}'\nu_{12}),$$
$$D_2^e = D_2^* - \frac{1}{2}(D_1'^2\nu_{22} + D_{12}'D_{21}'\nu_{12}),$$
$$D_{12}^e = D_{12}^* - \frac{1}{2}(D_1'D_{12}'\nu_{12} + D_2'D_{12}'\nu_{22}),$$
$$D_{21}^e = D_{21}^* - \frac{1}{2}(D_1'D_{21}'\nu_{11} + D_2'D_{21}'\nu_{12}); \tag{30}$$

$$N_{1*}^e = N_* + D_{12}^e, \quad N_{2*}^e = N_* - D_{21}^e; \tag{31}$$

$$\mathcal{P}_1^e = \mathcal{P}_1 - \frac{1}{2}(D_1'\nu_{11} + D_{12}'\nu_{22}),$$
$$\mathcal{Q}_1^e = \mathcal{Q}_1 - \frac{1}{2}(D_2'\nu_{22} + D_{21}'\nu_{11}). \tag{32}$$

Equations (28)–(32) allow us to draw the following qualitative conclusions concerning the effect of stochastic dissipative forces on the motion of the Earth's pole. First, the average values of the dissipation factors $D_{1,2}^e$ and gyroscopic moment (N_{1*}^e and N_{2*}^e) decrease. Second, additional constant components originate in the trend of the Earth's pole:

$$\langle m_1\rangle = -\frac{1}{2}(D_1'\nu_{11} + D_{12}'\nu_{22})(N_{1*}^e)^{-1},$$
$$\langle m_2\rangle = \frac{1}{2}(D_2'\nu_{22} + D_{21}'\nu_{11})(N_{2*}^e)^{-1}. \tag{33}$$

The corresponding effects are proportional to $\mathcal{D}$ and ν.

5. Equations (23) for the standard deviations k_{11} and k_{22} and covariance k_{12} have the form

$$\dot{k}_{11} = -2D_1^e k_{11} - 2N_{1*}^e k_{12} + c_{11}^e,$$
$$c_{11}^e = 2D_1\nu_{11}m_1 + 2D_{12}'\nu_{12}m_2 + (m_1^2 + k_{11})D_1'^2\nu_{11} + 2(m_1 m_2 + k_{12})D_1'D_{12}'\nu_{12} + (m_2^2 + k_{22})D_{12}'^2\nu_{12}; \tag{34}$$

$$\dot{k}_{12} = N_{2*}^e k_{11} - N_{1*}^e k_{22} - k_{12}(D_1^e + D_2^e) + c_{12}^e,$$
$$c_{12}^e = (D_1'\nu_{12} + D_{21}'\nu_{11})m_1 + (D_2'\nu_{12} + D_{12}'\nu_{22})m_2 + (m_1^2 + k_{11})D_{21}'D_1'\nu_{11} + (m_1 m_2 + k_{12})(D_{21}'D_{12}'\nu_{12} + D_2'D_1'\nu_{12}) + (m_2^2 + k_{22})D_{12}'D'_2\nu_{22}; \tag{35}$$

$$\dot{k}_{22} = 2N_{2*}^e k_{12} - 2D_2^e k_{22} + c_{22}^e,$$
$$c_{22}^e = 2D_{21}'\nu_{12}m_1 + 2D_2'\nu_{22}m_2 + (m_1^2 + k_{11})D_{21}'D_2'\nu_{11} + 2(m_1 m_2 + k_{12})D_{21}'D_2'\nu_{12} + (m_2^2 + k_{22})D_2'^2\nu_{22}. \tag{36}$$

Two important qualitative conclusions follow from these equations. First, when the moments of parametric dissipative fluctuation forces are isotropic ($\nu_{11} = \nu_{22} =$

$\nu_0, \nu_{12} = 0$, $D_1^* = D_2^* = D^*$, $D_1' = D_2' = D_0' > 0$, $D_{12}' = D_{21}' = 0$), since

$$D_i^e = D^* - \frac{D_0'^2 \nu_0}{2} > 0, \quad N_{i*}^e = N_*, \quad i = 1, 2; \tag{37}$$

$$c_{ii}^e = 2D_0' \nu_0 m_i + (m_i^2 + k_{ii}) D_0'^2 \nu_0, \quad i = 1, 2, \quad c_{12}^e = 0, \tag{38}$$

the standard deviations $\langle k_{11} \rangle$ and $\langle k_{22} \rangle$ increase due to c_{ii}^e. Second, the anisotropy of the parametric dissipative fluctuation forces ($\nu_{12} \neq 0$, D_{12}', $D_{21}' \neq 0$) changes the average covariance $\langle k_{12} \rangle$ and increases the standard deviations $\langle k_{11} \rangle$ and $\langle k_{22} \rangle$.

According to [9–11], the relaxation time D_*^{-1} averaged over various estimates is equal to 10–100 yr, while the standard deviations of p_t and q_t are equal to 0.02"–0.04". According to Eqs. (37) and (38), isotropic parametric dissipative fluctuations of about $D'^2 \nu_0 \sim 10^{-1} D^*$ additionally increase the standard deviations by 0.01"–0.02". The anisotropy of parametric dissipative fluctuations increases both dispersions and covariances by no less than 30% of the respective increases due to isotropic perturbations.

6. Thus, stochastic spectral correlation models have been developed for fluctuations induced in the motion of the pole of the deformable Earth by both isotropic and anisotropic dissipative fluctuations. The perturbation effects are estimated more accurately.

The results can be extended to the three cases where (i) fluctuations in the angular velocity of the Earth's rotation must be taken into account, (ii) additive noise differs from parametric noise, and (iii) the moments of rheological dissipative fluctuation forces are taken into consideration.

ACKNOWLEDGMENTS

This work was supported by the Branch of Information Technologies and Computer Systems, Russian Academy of Sciences (project no. 10002-251/OITVS-01/097-098/210503-180) and the Russian Foundation for Basic Research (project nos. 04-02-16303 and 01-01-00758).

REFERENCES

1. IERS Annual Reports, Central Bureau IERS, 2003.
2. L. V. Rykhlova, G. S. Kurbasova, and M. N. Rybalova, Nauchn. Inform. Astron. Inst. Akad. Nauk SSSR **69**, 3 (1991).
3. H. Moritz and I. Mueller, *Earth Rotation: Theory and Observations* (Ungar, New York, 1987; Naukova Dumka, Kiev, 1992).
4. Yu. G. Markov and I. N. Sinitsyn, Dokl. Akad. Nauk **385**, 189 (2002) [Dokl. Phys. **47**, 531 (2002)].
5. Yu. G. Markov and I. N. Sinitsyn, Dokl. Akad. Nauk **390**, 343 (2003) [Dokl. Phys. **48**, 253 (2003)].
6. Yu. G. Markov and I. N. Sinitsyn, Dokl. Akad. Nauk **391**, 194 (2003) [Dokl. Phys. **48**, 364 (2003)].
7. V. S. Pugachev and I. N. Sinitsyn, *Theory of Stochastic Systems* (Logos, Moscow, 2003).
8. V. S. Pugachev and I. N. Sinitsyn, *Stochastic Differential Systems: Analysis and Filtration* (Nauka, Moscow, 1990).
9. Yu. G. Markov and I. N. Sinitsyn, Dokl. Akad. Nauk **393**, 618 (2003) [Dokl. Phys. **48**, 691 (2003)].
10. M. Arato, *Linear Stochastic Systems with Constant Coefficients: A Statistical Approach* (Springer, Berlin, 1982; Nauka, Moscow, 1989).
11. N. S. Sidorenkov, *Physics of the Earth Rotation Instability* (Nauka, Moscow, 2002).

Translated by V. Chechin

Doklady Physics, Vol. 49, No. 3, 2004, pp. 183–186. Translated from Doklady Akademii Nauk, Vol. 395, No. 1, 2004, pp. 55–58.

MECHANICS

Classification of Three-Dimensional Periodic Fluid Flows

Yu. D. Chashechkin and A. V. Kistovich

Presented by Academician V.V. Kozlov October 22, 2003

Received October 24, 2003

Each physical factor—rotation, stratification, and compressibility of a fluid—is associated with a characteristic type of waves, which are usually analyzed independently [1]. However, elementary waves (acoustic, internal, gyroscopic) do not completely present the properties of periodic flows in the bulk of a real fluid, where all factors act simultaneously and hybrid waves with a complicated dispersion law exist. When studying waves, dissipation effects are considered as corrections ensuring flow attenuation [2]. However, in continua, dissipation factors determine the order of equations and the total number of elements of periodic flows, including waves and sets of boundary layers on rigid boundaries and free surfaces. The consistent inclusion of dissipation effects enables one to find self-consistent solutions of linearized problems of the generation of internal waves [3] without additional empirical parameters (force and mass sources [2]).

In this work, the complete mathematical classification of three-dimensional periodic flows in the bulk of a fluid is given for the first time with allowance for compressibility, stratification, rotation, and viscous dissipation. Diffusion and heat conduction are disregarded. Only general-type propagating waves having all wave-vector components are analyzed.

Small-amplitude waves in a viscous inhomogeneous fluid rotating with angular velocity Ω in the gravitational field with acceleration g are studied. The unperturbed stable density distribution $\rho(z)$ is determined by the buoyancy scale $\Lambda = \left|\frac{d\ln\rho(z)}{dz}\right|^{-1}$. Oscillations of stratified incompressible and compressible media are characterized by the buoyancy frequency $N = \sqrt{\frac{g}{\Lambda}}$ and adiabatic frequency $N_c = \sqrt{N^2 - \frac{g^2}{c^2}}$, respectively, where c is the speed of sound.

We use the Cartesian coordinate system (x, y, z), where the z axis is directed to the zenith and the x and y axes are taken so that the corresponding projections of the angular velocity are equal to each other. In the linear approximation, the system of the equations of motion has the form [1]

$$\frac{\partial u}{\partial t} = -\frac{\partial P}{\partial x} + 2\Omega\left(v\sin\varphi - \frac{1}{\sqrt{2}}w\cos\varphi\right) + \nu\Delta u + \left(\mu + \frac{\nu}{3}\right)\frac{\partial}{\partial x}\nabla\cdot\mathbf{u},$$

$$\frac{\partial v}{\partial t} = -\frac{\partial P}{\partial y} + 2\Omega\left(\frac{1}{\sqrt{2}}w\cos\varphi - u\sin\varphi\right) + \nu\Delta v + \left(\mu + \frac{\nu}{3}\right)\frac{\partial}{\partial y}\nabla\cdot\mathbf{u}, \quad (1)$$

$$\frac{\partial w}{\partial t} = -\frac{\partial P}{\partial z} + \sqrt{2}\Omega(u - v)\cos\varphi + \nu\Delta w + \left(\mu + \frac{\nu}{3}\right)\frac{\partial}{\partial z}\nabla\cdot\mathbf{u} - \rho g,$$

$$\frac{\partial\rho}{\partial t} - \frac{w}{\Lambda} + \nabla\cdot\mathbf{u} = 0, \quad \frac{\partial P}{\partial t} = wg - c^2\nabla\cdot\mathbf{u},$$

where $\mathbf{u} = (u, v, w)$ is the velocity, P and ρ are the pressure minus hydrostatic pressure and medium-density perturbation normalized to the density at the reference level $z = 0$, φ is the latitude of the observation point, and ν and μ are the first and second kinematic viscosities.

System (1) is supplemented by the no-slip boundary conditions on rigid surfaces and the condition of damping of perturbations at infinity. The dynamic and kine-

Institute for Problems in Mechanics,
Russian Academy of Sciences,
pr. Vernadskogo 101/1, Moscow, 117526 Russia
e-mail: chakin@ipmnet.ru
e-mail: akist@vniiftri.ru

1028-3358/04/4903-0183$26.00

matic boundary conditions on the free surface $z_S = \zeta(x, y)$ have the form [1]

$$(p - p_0)n_i - (\sigma'_{ik} - \sigma'^{(0)}_{ik})n_k + \alpha n_i \Delta_\perp \zeta|_{z=\zeta} = 0,$$
$$\frac{\partial \zeta}{\partial t} = w|_{z=\zeta}, \quad \Delta_\perp = \frac{\partial^2}{\partial x^2} + \frac{\partial^2}{\partial y^2}, \tag{2}$$

where p and p_0 are pressures inside and outside the medium under consideration, respectively; σ'_{ik} and $\sigma'^{(0)}_{ik}$ are the corresponding viscous stress tensors; α is the surface tension coefficient; and n_i is the component of the unit normal to the surface. Analysis of system (1) is simplified when the viscosity coefficient and the ratio of the densities of the media in contact (e.g., liquid and gas) are small.

When studying periodic flows

$$\mathbf{u} = \mathbf{u}_0 \exp(ikr - i\omega t), \quad P = P_0 \exp(ikr - i\omega t),$$
$$\rho = \rho_0 \exp(ikr - i\omega t)$$

with frequency ω and wave vector $\mathbf{k} = (k_x, k_y, k_z)$, the general solution of system (1) is represented as a superposition of elementary waves [4]

$$A = \sum_j \int_{-\infty}^{+\infty} \int_{-\infty}^{+\infty} a_j(k_x, k_y) \exp(i(k_{zj}(k_x, k_y)z + k_x x + k_y y - \omega t))dk_x dk_y, \tag{3}$$

where A is a velocity component, pressure, or density. The summation is performed over all roots of the dispersion equation that satisfy the boundary conditions of the problem or the radiation condition in an unbounded medium (damping of perturbations at infinity). The dispersion equation is obtained by substituting the solution in form (3) into Eqs. (1). For steady periodic waves, frequency ω is given, and the dispersion equation describes the relation between the wavenumber components [e.g., $k_{zj}(k_x, k_y)$ for given k_x and k_y values].

System (1) with boundary conditions (2) admits two types of waves: surface waves whose amplitude decreases monotonically with the distance from the boundary and internal waves with maximum displacements in the bulk of the fluid. When the media in contact have considerably different densities, their properties can be analyzed independently [1].

For flows in the bulk of the fluid, the substitution of Eq. (3) into Eqs. (1) yields the system of algebraic equations for the amplitudes u_0, v_0, w_0, P_0, and ρ_0:

$$\left(i\omega - \nu k^2 - \left(\mu + \frac{\nu}{3}\right)k_x^2\right)u_0 + \left(2\Omega \sin\varphi - \left(\mu + \frac{\nu}{3}\right)k_x k_y\right) \times v_0 - \left(\sqrt{2}\Omega \cos\varphi + \left(\mu + \frac{\nu}{3}\right)k_x k_z\right)w_0 - ik_x P_0 = 0,$$
$$-\left(2\Omega \sin\varphi + \left(\mu + \frac{\nu}{3}\right)k_x k_y\right)u_0 + \left(i\omega - \nu k^2 - \left(\mu + \frac{\nu}{3}\right)k_y^2\right)v_0 + \left(\sqrt{2}\Omega \cos\varphi - \left(\mu + \frac{\nu}{3}\right)k_y k_z\right)w_0 - ik_y P_0 = 0, \quad \left(\sqrt{2}\Omega \cos\varphi - \left(\mu + \frac{\nu}{3}\right)k_x k_z\right)u_0 \tag{4}$$
$$-\left(\sqrt{2}\Omega \cos\varphi + \left(\mu + \frac{\nu}{3}\right)k_y k_z\right)v_0 + \left(i\omega - \nu k^2 - \left(\mu + \frac{\nu}{3}\right)k_z^2\right)w_0 - ik_z P_0 - g\rho_0 = 0,$$
$$-ik_x u_0 - ik_y v_0 + \left(\frac{1}{\Lambda} - ik_z\right)w_0 + i\omega\rho_0 = 0,$$
$$-ik_x c^2 u_0 - ik_y c^2 v_0 + (g - ik_z c^2)w_0 + i\omega P_0 = 0,$$

where $k^2 = k_x^2 + k_y^2 + k_z^2$.

The condition of the existence of a nontrivial solution provides the dispersion equation for hybrid waves of the most general type:

$$\omega D_\nu(k)(\omega D_\nu(k)\tilde{D}_\nu(k) + 2\sqrt{2}\omega\Omega g(k_y - k_x)\cos\varphi) - \omega D_\nu(k)N^2\left(D_\nu(k) + i\left(\mu + \frac{\nu}{3}\right)k_\perp^2\right) + 4\omega\Omega^2\left(N^2 \sin^2\varphi - \omega\left(D_\nu(k) + i\left(\mu + \frac{\nu}{3}\right)f^2(k)\right)\right) + c^2(D_\nu(k)(N_c^2 k_\perp^2 - \omega k^2 D_\nu(k)) + 4\omega\Omega^2 f^2(k)) = 0, \tag{5}$$

where

$$f(k) = \frac{1}{\sqrt{2}}(\sqrt{2}k_z \sin\varphi + (k_x + k_y)\cos\varphi),$$
$$\tilde{D}_\nu(k) = \omega + i\left(\frac{4\nu}{3} + \mu\right)k^2, \quad D_\nu(k) = \omega + i\nu k^2.$$

Dispersion equation (5) for the wavenumber k is singularly perturbed, because the leading, k^6, term involves a small factor ν^2. In the general case, two of the six roots of Eq. (5) are regular in viscosity and describe the propagation of wave perturbations and the remaining four roots characterize the set of coexisting boundary layers. Single-frequency boundary layers dif-

fer from each other in thickness and other properties. Their number and behavior generally depend on the space dimension and are determined by the boundary conditions.

Solutions of Eq. (5) are further analyzed in the spherical coordinate system (k, Ψ, Θ) introduced in the wavenumber space (k_x, k_y, k_z) by the relations

$$k_x = k\sin\Theta\cos\Psi, \quad k_y = k\sin\Theta\sin\Psi, \quad k_z = k\cos\Theta.$$

In this analysis, both types of singular solutions, as well as solutions regular in viscosity, are taken into account.

The domain of existence of propagating waves that have real frequency ω and are characterized by dispersion relation (5) depends on many factors, such as the ratio of wave, rotation, and buoyancy frequencies, the compressibility of the medium, and the geometry of the problem, and is determined by the inequality

$$2\omega^2\Omega^2\sin^2\Theta\cos^2\varphi(\sin\Psi - \cos\Psi)^2 \geq \frac{c^2(4\Omega^2(N^2\sin^2\varphi - \omega^2) - \omega^2(N^2 - \omega^2))}{g^2(N_c^2\sin^2\Theta - \omega^2 + 4\Omega^2F^2)}, \quad (6)$$

which is simplified for certain types of waves.

In an unbounded medium on a plane the normal to which is characterized by angles Ψ and Θ, two boundary layers with the thickness

$$\delta_{b\pm} = \sqrt{\frac{2\nu}{N|\omega_\pm - \omega^*|}}, \quad \omega^* = \frac{\omega}{N},$$

$$\omega_\pm = \frac{N_c}{2\omega}\sin^2\Theta\left[1 \pm \sqrt{1 + \frac{16\omega^2\Omega^2F^2}{N_c^4\sin^4\Theta}}\right], \quad (7)$$

where

$$F = \frac{1}{\sqrt{2}}(\sqrt{2}\cos\Theta\sin\varphi + \sin\Theta(\sin\Psi + \cos\Psi)\cos\varphi)$$

along with three-dimensional waves, are generally formed. Since the condition $\frac{g\Lambda}{c^2} \ll 1$ is satisfied for virtually all media, the adiabatic frequency N_c in expressions for $\omega_\pm$ in Eqs. (7) can be approximately replaced by the buoyancy frequency N.

Taking compressibility into account and disregarding rotation effects ($\Omega = 0$), we conclude from Eq. (5) that propagating three-dimensional acoustic gravity waves exist in two frequency bands $\omega \leq N_c$ and $\omega \geq N$, in agreement with [6]. In the $\omega \ll N_c$ band, they exhibit the properties of internal gravity waves, and their characteristics for $\omega \gg N$ approach the isotropic sound. Simultaneously with waves, two types of boundary layers with the characteristic thicknesses

$$\delta_{St} = \delta_N\sqrt{\frac{2}{\sin\Theta_\omega}},$$

$$\delta_i = \delta_N\sqrt{\frac{2\sin\Theta_\omega}{\left|\left(1 - \frac{g\Lambda}{c^2}\right)\sin^2\Theta - \sin^2\Theta_\omega\right|}} \approx \delta_N\sqrt{\frac{2\sin\Theta_\omega}{|\sin^2\Theta - \sin^2\Theta_\omega|}}, \quad (8)$$

where

$$\delta_N = \sqrt{\frac{\nu}{N}}, \quad \Theta_\omega = \arcsin\frac{\omega}{N}$$

are formed at rigid boundaries. The first of them is similar to the periodic Stokes flow in a homogeneous fluid [1], and the second, whose parameters depend both on the buoyancy frequency N and on the speed of sound c, is specific for stratified media. The universal microscale δ_N is common for both boundary layers. The thicknesses of the boundary layers also depend on the slopes of the waves and bounding surfaces. The characteristics of the boundary layers supplementing internal waves were analyzed in [5] disregarding compressibility and rotation.

The frequency band $\omega_- < \omega < \omega_+$ of the existence of inertial gravity waves in stratified rotating incompressible media is limited by the values

$$\omega_\pm^2 = \frac{1}{2}(N^2 + 4\Omega^2 \pm \sqrt{(N^2 + 4\Omega^2\cos2\varphi)^2 + 16\Omega^4\sin^2 2\varphi}),$$

which depend on the latitude of the observation point. Simultaneously with three-dimensional inertial gravity waves, there are two types of boundary layers with the scales

$$\delta_{b\pm} = \delta_N\sqrt{\frac{2}{|\omega_\pm - \omega^*|}},$$

$$\omega_\pm = \frac{\sin^2\Theta}{2\omega^*}\left[1 \pm \sqrt{1 + \frac{16\Omega^2\omega^{*2}F^2}{N^2\sin^4\Theta}}\right], \quad \omega^* = \frac{\omega}{N}. \quad (9)$$

Inertial acoustic waves in an unstratified fluid ($N = 0$) coexist with two separated boundary layers with the thickness

$$\delta_{b\pm} = \sqrt{\frac{\nu}{\Omega|F \pm \cos\Theta_\omega|}}, \quad (10)$$

where $\Theta_\omega = \arccos\frac{\omega}{2\Omega}$ is the slope of the propagation

lines of the inertial acoustic waves to the horizon. One of these waves with thickness δ_{b+} is an analogue of the known Ekman layer [9]. Periodic flows have the properties of inertial and acoustic waves for $\omega \ll \Omega$ and the opposite case, respectively.

Three-dimensional acoustic waves in a homogeneous fluid ($N = \Omega = 0$) are characterized by the dispersion $\omega^2 = k^2\left(c^2 - i\omega\left(\frac{4\nu}{3} + \mu\right)\right)$. In this case, two sets of boundary layers are joined in the united doubly degenerate Stokes layer with the thickness $\delta_{St} = \sqrt{\frac{2\nu}{\omega}}$. Perturbations within this layer are transverse with zero divergence of the velocity; i.e., the fluid within it behaves as incompressible.

From the form of the dispersion of three-dimensional periodic perturbations in a homogeneous incompressible fluid, $k^2 D_\nu^2(k) = 0$, when $N = \Omega = \nabla \cdot \mathbf{u} = 0$, it follows that this medium is free of developed propagating waves, and a doubly degenerate viscous boundary layer consisting of two periodic Stokes flows with thickness $\delta_{St} = \sqrt{\frac{2\nu}{\omega}}$ arises near the rigid oscillating boundary.

The inclusion of thermal diffusivity and diffusion in multicomponent media leads to both the appearance of additional equations in system (1) of the equations of motion and an increase in the number of types of boundary layers. Each dissipative factor gives rise to the appearance of a new pair of boundary layers, which can be both completely or partially separated [8].

Large-scale wave and fine-structure boundary-layer elements are inseparable components of the united system of periodic flows. All elements of this system appear and disappear simultaneously, regardless of differences in scales.

In the general case, solutions for stratified rotating media allow the uniform transition to a homogeneous fluid at rest. In this case, two different boundary layers are joined in the united degenerate layer. The inverse analytic extrapolation of solutions is impossible because of the insufficient completeness of the original problem formulation.

In the general case, the dynamics of hydrodynamic systems is determined by the nonlinear interaction between all structural elements of flows both regular, waves, and singular, boundary layers. In particular, variations in the structure and nonlinear interactions of boundary layers make it possible to generate internal waves even in the cases, where direct excitation is forbidden in linear theory by the conditions of wave propagation [9, 10]. Owing to large vorticity, interacting boundary layers are effective generators of vortex motions. Experimental study of the dynamics of boundary layers and generation of vortices requires substantial improvement of instruments for visualization and measurement of flows. These instruments must resolve the fine structure of the smallest elements of flows.

REFERENCES

1. L. D. Landau and E. M. Lifshitz, *Course of Theoretical Physics*, Vol. 6: *Fluid Mechanics* (Nauka, Moscow, 1986; Pergamon, New York, 1987).
2. M. J. Lighthill, *Waves in Fluids* (Cambridge Univ. Press, Cambridge, 1978; Mir, Moscow, 1981).
3. Yu. V. Kistovich and Yu. D. Chashechkin, Prikl. Mekh. Tekh. Fiz. **42**, 52 (2001).
4. G. B. Whitham, *Linear and Nonlinear Waves* (Wiley, New York, 1974; Mir, Moscow, 1977).
5. A. Yu. Vasil'ev and Yu. D. Chashechkin, Prikl. Mekh. Tekh. Fiz. **67**, 442 (2003).
6. I. Tolstoy, *Wave Propagation* (McGraw-Hill, New-York, 1973).
7. J. Pedlosky, *Geophysical Fluid Dynamics* (Springer, Heidelberg, 1981; Mir, Moscow, 1984; Springer, New York, 1987), Vol. 2.
8. Yu. D. Chashechkin and A. V. Kistovich, Dokl. Akad. Nauk **393**, 776 (2003) [Dokl. Phys. **48**, 710 (2003)].
9. Yu. V. Kistovich and Yu. D. Chashechkin, Dokl. Akad. Nauk **367**, 636 (1999) [Dokl. Phys. **44**, 573 (1999)].
10. Yu. V. Kistovich and Yu. D. Chashechkin, Dokl. Akad. Nauk **382**, 772 (2002) [Dokl. Phys. **47**, 163 (2002)].

Translated by R. Tyapaev

Doklady Physics, Vol. 49, No. 3, 2004, pp. 187–190. Translated from Doklady Akademii Nauk, Vol. 395, No. 2, 2004, pp. 192–195.

MECHANICS

Effect of Conjugate Resonances and Bifurcations under the Biharmonic Excitation of a Pendulum with a Vibrating Suspension Axis

I. I. Blekhman* and P. S. Landa**

Presented by Academician N.F. Morozov October 6, 2003

Received October 14, 2003

1. We call attention to the effect of conjugate resonances and bifurcations in nonlinear systems excited by a biharmonic action with substantially different frequencies. This effect is that resonances and bifurcations arise in such systems when (i) the low frequency varies while the high frequency is fixed, (ii) the high frequency varies while the low frequency is fixed, and (iii) the amplitude of the high-frequency action varies, whereas the frequencies are fixed. As an example, we studied both ordinary and parametric resonances in the classical problem of the behavior of a pendulum with the vibrating suspension axis. It is clear that the effects under consideration take place also in other, more complicated, systems, including systems with random excitation. The results make it possible to deterministically explain the mechanism of the widely discussed phenomenon of stochastic resonance (see also [2]). In conclusion, we mention the applications of the results to the problems of controlling the resonance properties of systems and preventing any resonant situations.

We use the approach of vibrational mechanics and the method of the direct separation of motions [1]. In this approach, the effects under consideration are explained as follows. A high-frequency vibration substantially changes the parameters and response of the system to the low-frequency action. As a result, the low-frequency action is such as if it was applied to another system. In the particular case of a pendulum, it is a system with different effective restoring force, which essentially depends on the frequency and amplitude of the high-frequency action. Thus, the effects under consideration are closely associated with the strong influence of a high-frequency vibration on the effective elastic characteristics of bodies. This property was discussed in detail in [1, 2] and in references cited therein.

The problem of the biharmonic action on the other system, the Duffing oscillator, was considered in [3]. It was shown that the results obtained by the method of the direct separation of motions agreed well with the previous numerical investigation [4]. In the last paper, the shift of resonances under high-frequency excitation was also discovered and such resonances were called vibrational.

2. We consider a pendulum whose suspension axis oscillates in two mutually perpendicular directions according to the law (Fig. 1)

$$\begin{aligned} x &= H_\Omega \sin\Omega t + H_\omega \sin\omega t, \\ y &= G_\Omega \cos(\Omega t + \theta_\Omega) + G_\omega \cos(\omega t + \theta_\omega), \end{aligned} \tag{1}$$

where Ω and ω are the frequencies, H and G are the amplitudes, and θ is the phase shift. The pendulum axis

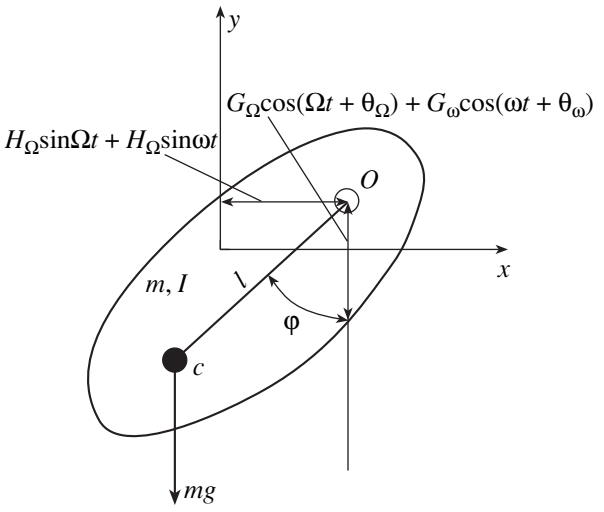

Fig. 1. Pendulum with a vibrating suspension axis.

* *Institute of Problems of Mechanical Engineering, Russian Academy of Sciences, Vasil'evskiĭ Ostrov, Bol'shoĭ pr. 61, St. Petersburg, 199178 Russia*
OAO Mekhanobr-Tekhnika, St. Petersburg, Russia
e-mail: blekhman@vibro.ipme.ru

** *Moscow State University, Vorob'evy gory, Moscow, 119992 Russia*
e-mail: planda@lpi.ru

1028-3358/04/4903-0187$26.00 © 2004 MAIK "Nauka/Interperiodica"

oscillates with each of the two frequencies along an elliptic trajectory. The equation of motion of the pendulum has the form

$$I\ddot{\varphi} + h\dot{\varphi} + mgl\sin\varphi + ml\Omega^2[H_\Omega\cos\varphi\sin\Omega t - G_\Omega\sin\varphi\cos(\Omega t + \theta_\Omega)] + ml\omega^2[H_\omega\cos\varphi\sin\omega t - G_\omega\sin\varphi\cos(\omega t + \theta_\omega)] = 0, \quad (2)$$

where φ is the angle of deviation of the pendulum from the lower position; I, m, and l are the moment of inertia, mass, and distance from the center of gravity C to the axis of suspension of the pendulum O, respectively; g is the gravitational acceleration; and h is the viscous resistance coefficient.

3. Let the high frequency Ω be much higher than the low frequency ω (by a factor of no less than three). Then, seeking the solution of Eq. (2) in the form

$$\varphi = \alpha(t) + \psi(t, \Omega t), \quad (3)$$

where α is the slow component and ψ is the fast component that is 2π-periodic in Ωt and has a zero average, we use the method of direct separation of motions [1]. As a result, we arrive at the following equation of slow motions:

$$I\ddot{\alpha} + h\dot{\alpha} + mgl\sin\alpha + \frac{(ml\Omega)^2}{4I}[(G_\Omega^2 - H_\Omega^2)\sin 2\alpha + 2G_\Omega H_\Omega\cos 2\alpha\sin\theta_\omega] = -ml\omega^2[H_\omega\cos\alpha\sin\omega t - G_\omega\sin\alpha\cos(\omega t + \theta_\omega)]. \quad (4)$$

This equation is obtained under the assumptions

$$\frac{p}{\omega} \sim \varepsilon, \quad \frac{ml\sqrt{G_\Omega^2 + H_\Omega^2}}{I} = \frac{\sqrt{G_\Omega^2 + H_\Omega^2}}{l_0} \sim \varepsilon, \quad \frac{h}{I\Omega} \sim \varepsilon. \quad (5)$$

Here, ε is a small parameter and $p = \sqrt{\frac{mgl}{I}} = \sqrt{\frac{g}{l_0}}$, where l_0 is the equivalent length of the mathematical pendulum. The moments with the frequency ω are treated as slow moments.

For one-frequency fast oscillations of the axis of the pendulum, when $G_\omega = H_\omega = 0$, the main qualitative result of investigating Eq. (5) is as follows [1]. Due to vibration, the pendulum seems to be attracted to the major semiaxes of the elliptic trajectory of the pendulum-axis oscillations. If this attraction is strong enough (in the case of vertical vibration), then the upper position of the pendulum, which is unstable in the absence of vibration, becomes stable (the main classical result [1, 5, 6]).

Let us now analyze more complicated equation (4).

4. First, we consider the case of ordinary resonance. This case corresponds to the vertical fast and horizontal slow oscillations of the axis ($H_\Omega = 0$, $G_\Omega = 0$). Equation (4) takes the form

$$I\ddot{\alpha} + h\dot{\alpha} + mgl\sin\alpha + \frac{(mlG_\Omega)^2}{4I}\Omega^2\sin 2\alpha = -mlH_\omega\omega^2\sin\omega t. \quad (6)$$

The small oscillations of the pendulum near the lower equilibrium position are described by the equation

$$I\ddot{\alpha} + h\dot{\alpha} + \left[mgl + \frac{(mlG_\Omega\Omega)^2}{2I}\right]\alpha = -mlH_\omega\omega^2\sin\omega t. \quad (7)$$

Hence, the resonance arises when the following equality is satisfied (disregarding the small damping effect):

$$\omega = p_{v0} = \sqrt{p^2 + q^2\Omega^2}, \quad p^2 = \frac{mgl}{I} = \frac{g}{l_0}, \quad q^2 = \frac{1}{2}\left(\frac{mlG_\Omega}{I}\right)^2 = \frac{1}{2}\left(\frac{G_\Omega}{l_0}\right)^2; \quad (8)$$

where p_{v0} is the frequency of free oscillations near the lower position. This frequency is changed under the high-frequency vibration.

It follows from relation (8) that the resonance (peak of the oscillation amplitude A under variation of the parameter) may arise in this system when both the slow-oscillation frequency ω of the pendulum axis varies, whereas the fast-oscillation frequency Ω is fixed (Fig. 2a), and vice versa (if $\omega > p$, see Fig. 2b). It is also remarkable that the dependence of the oscillation amplitude of the pendulum is resonant under variation of the fast oscillation amplitude G_Ω to which the parameter q is proportional (and also if $\omega > p$, see Fig. 2c). If $\omega < p$, the dependences in Figs. 2a and 2b are monotonic. The described resonances, i.e., the resonances whose frequencies are related by the first of Eqs. (8), are referred to as conjugate resonances.

The plot in Fig. 2c is similar to that given when considering the phenomenon called the stochastic resonance (see, e.g., [3]). The above discussion shows that this effect is not associated with noise-induced random jumps of the system. It occurs because the high-frequency component changes the effective stiffness of the system with respect to the low-frequency signal. All the above effects are explained by this change, depending essentially on both the frequency Ω and amplitude G_Ω.

All above resonances correspond to the forced oscillations of the pendulum with low frequency ω.

Let us now consider the small oscillations of the pendulum near the upper position $\alpha = \pi$. Equation (6) easily leads to the classical condition $G_\Omega\Omega > \sqrt{2gl_0}$, under which the upper position of the pendulum is stable [1, 5, 6]. In terms of the above notation, this inequality takes the form

$$q\Omega > p. \tag{9}$$

The resonance takes place if the following equality is satisfied:

$$\omega = p_{v\pi} = \sqrt{q^2\Omega^2 - p^2}, \tag{10}$$

where $p_{v\pi}$ is the frequency of the free oscillation of the pendulum near the upper equilibrium position.

Similarly to the first of Eqs. (8), equality (10) generates three kinds of resonances, and we could draw plots similar to those shown in Fig. 2. The difference is that, first, the condition $\omega < p$ is satisfied automatically in this case and, second, the bifurcation points are conjugate, which corresponds to the change in the stability character of the upper position of the pendulum at $q\Omega = p$. These points can be achieved when both the frequency Ω varies, whereas the amplitude G_Ω is constant, and vice versa.

5. Let us now discuss parametric resonance. This case corresponds to the fast and slow vertical oscillations of the pendulum axis ($H_\Omega = 0$, $H_\omega = 0$). Equation (4) for the small oscillations of the pendulum near the stable equilibrium position $\alpha = 0$ takes the form

$$\ddot{\alpha} + h_1\dot{\alpha} + p_{v0}^2[1 - \gamma\sin(\omega t + \theta_\omega)]\alpha = 0, \tag{11}$$

where $h_1 = \dfrac{h}{I}$ and $\gamma = \dfrac{G_\omega\omega^2}{l_0 p_{v0}^2}$. The condition of the basic parametric resonance is the equality

$$\omega = 2p_{v0} = 2\sqrt{p^2 + q^2\Omega^2}, \tag{12}$$

which differs from the first of Eqs. (8) only by a factor of two. Therefore, all statements made in Section 4 are completely valid for this case (the same is true for other parametric resonances).

6. The properties established above for a particular example are applicable for general nonlinear systems with positional nonlinearity, such as the system that is described by the Duffing equation and sometimes called bistable oscillator [3].

Another generalization refers to the nonlinear system under consideration excited by a random action with the pronounced high- and low-frequency components of the spectrum. In this case, the high-frequency component of excitation changes the properties of the system with respect to the low-frequency component. As a result, the low-frequency excitation seems to be acting on another system modified by the high-frequency excitation, and this change depends significantly on the intensity of the high-frequency component.

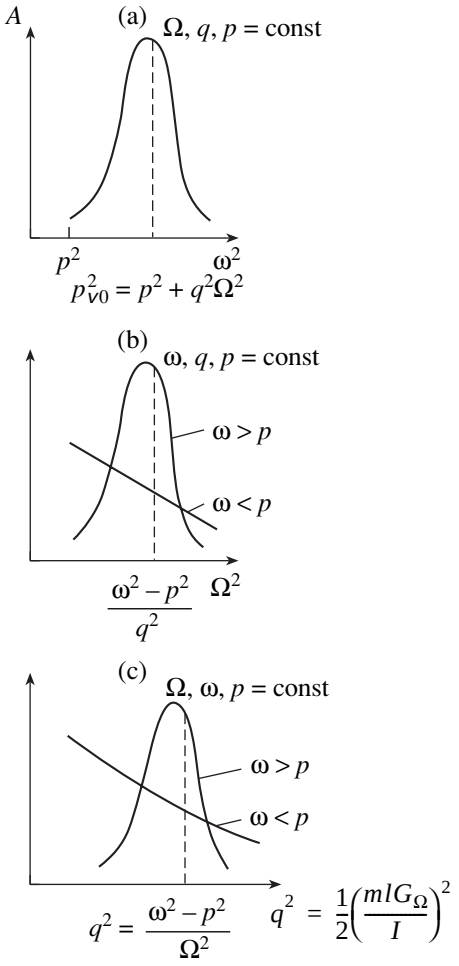

Fig. 2. Ordinary conjugate resonances near the lower position of the pendulum under variation of the (a) low frequency, (b) high frequency, and (c) amplitude of the high-frequency action.

The above results make it possible to simply explain the mechanism of the effect of stochastic resonance—nonmonotonic (resonance) dependence of the amplitude of the output signal in the nonlinear system on the level of a random action. The same is true for the corresponding bifurcations.

Two practical consequences are as follows. First, the resonance states of the system with respect to the low-frequency action can be controlled by varying the high-frequency action. Second, it is necessary to take into account changes induced by the high-frequency action in the resonance frequencies of the system with respect to the low-frequency action.

ACKNOWLEDGMENTS

This work was supported by the Presidium of the Russian Academy of Sciences (program no. 19, project no. 1.4) and the Council of the President of the Russian Federation for Support of Young Russian Scientists and Leading Scientific Schools (project no. NSh-1521.2003.8).

REFERENCES

1. I. I. Blekhman, *Vibrational Mechanics* (Fizmatlit, Moscow, 1994; World Scientific, Singapore, 2000).
2. P. S. Landa, *Regular and Chaotic Oscillations* (Springer, Heidelberg, 2001).
3. I. I. Blekhman and P. S. Landa, Izv. Vyssh. Uchebn. Zaved., Prikl. Nelineĭnaya Din., Nos. 1–2, 44 (2002).
4. P. S. Landa and P. V. E. McClintock, J. Phys. A **33**, L433 (2000).
5. A. Stephenson, Mem. Proc. Manch. Philos. Lit. Soc. **52**, 1 (1908).
6. P. L. Kapitsa, Zh. Éksp. Teor. Fiz. **21**, 588 (1951).

Translated by I. Blekhman

Doklady Physics, Vol. 49, No. 3, 2004, pp. 191–193. Translated from Doklady Akademii Nauk, Vol. 395, No. 2, 2004, pp. 196–198.

MECHANICS

Physical Modeling of Firestorms

A. M. Grishin, A. N. Golovanov, and Ya. V. Sukov

Presented by Academician G.G. Chernyĭ October 30, 2003

Received October 31, 2003

Firestorms are a kind of atmospheric vortices (tornados). As a rule, they accompany city [1] or forest fires [2]. At present, there are almost no experimental data on the initiation and development of firestorms, contrary to the case of tornados [3]. In this paper, we report the results of laboratory physical modeling on various setups with different swirls of a convective column.

As combustible materials, we used crude oil (modeling of firestorms accompanying accidents with oil reservoirs); combustible forest materials, including fallen pine and cedar needles and birch foliage (modeling of firestorms accompanying forest fires); and fragments of various wooden constructions with sizes of $1 \times 3 \times 5$ cm and $1 \times 1 \times 3$ mm (modeling of firestorms accompanying fires in cities and other urban areas). The substrate-surface area was chosen from the condition $\frac{h}{D} = (1.0–5.0)_{10^{-3}}$, where h is the height of substrate elements and D = 6–15 cm is the diameter. The moisture content in elements was $W = \frac{m - m_0}{m_0} = 0.007–0.13$, where m is the mass of damp fragments and m_0 is the mass of the fragments dried at a temperature of 373 K; i.e., it was below the critical moisture content for which land forest fires were initiated [2]. Combustible materials were placed on special substrates and were ignited by a hot wire.

During the experiments, the following parameters of gas and combustible materials were monitored. The gas temperature T_c was measured by the thermoelectric method using a chromel–alumel thermocouple with a junction diameter of 0.2 mm. The heat-flux density q was measured by the exponential method using a heat-flux transducer. The gas velocity v_l along the y axis (see Fig. 1) and the tangential velocity v_t were measured by the hot-wire and pneumatic methods as well as by photographing the trajectories of fine-grained aluminum particles introduced into the flow in the direction of the tangential velocity of the vortex. The exposure of the camera was equal to $\tau = 0.008$ s. The photographic film was processed on an MF-2 microphotometer.

The parameters were determined with total errors $\delta T_c \le 4.8\%$; $\delta q \le 9.2\%$; $\delta v \le 9.0\%$ (hot-wire anemometer), 7.9% (tracks of luminous particles), and 6.1% (Pitot–Prandtl tube); and $\delta m \le 2.3\%$. Using the results of measurements (three to five experiments), the 0.95 confidence intervals were calculated.

Figures 1 and 2 show the photographs of the flame front in a firestorm formed when burning oil. Contrary to the interaction between an atmospheric vortex and a heavy liquid with a concave free surface, the interaction between the firestorm and a fire source is accompanied by the formation of a mushroom-shaped convective column composed of hot combustion products and air, where heated particles move along spiral lines. Therefore, it is appropriate to use the term firestorm to describe the result of this interaction.

Table 1 presents the heat-flux densities measured by the transducer, which was introduced into the firestorm base at the point 0 (see Fig. 1), under various experimental conditions. The analysis of these results shows

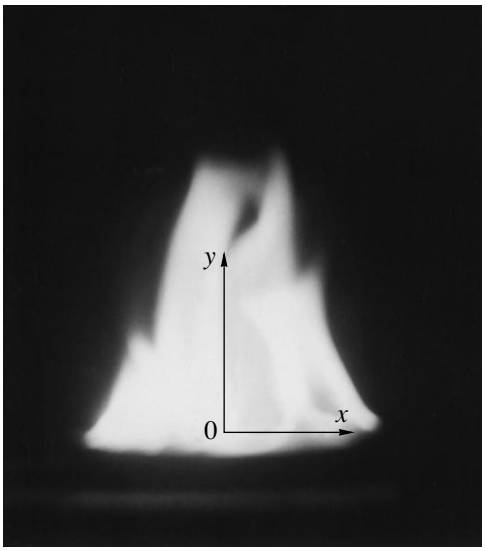

Fig. 1. Flame front formed by the oil-combustion products without the rotation of the column.

Tomsk State University,
pr. Lenina 36, Tomsk, 634050 Russia
e-mail: fire@fire.tsu.tomsk.su

1028-3358/04/4903-0191$26.00

Fig. 2. Firestorm, $\omega = 1.2$ rad/s.

that the heat-flux density depends only slightly on the fuel type and is higher than that from a free burning surface by 13% due to an increase in the convective component of the heat flux when forming the firestorm. Within an accuracy of 10%, the density of the convective heat flux in the direction of the vertical z axis at the flame height $z = h$ is determined by the formula

$$q = \frac{AmQ}{\tau_b S}, \quad (1)$$

where $Q = 46 \times 10^6$ J/kg is the thermal effect of the oil-combustion reaction, S is the burning-surface area, τ_b is the burning time, and A is the matching factor.

The results of calculations are given in Table 2. It is easily seen that the density of the heat fluxes generated by the firestorms under laboratory conditions agree with the calculations.

The measurements of gas velocities show that there is a firestorm at a height of 8–10 cm, where the tangential velocity is approximately constant and the vertical velocity component increases. This fact can be explained by the inflow of air mass from the vortex environment, which is corroborated by the measurements of the radial velocity of the gas by the hot-wire anemometer.

Burning combustible forest materials of the same mass in vortex-free and vortex flows, we investigated the effect of flow swirling on the burning rate. The burning time τ_b on the free surface was equal to 45.0, 43.0, 44.0, and 37.0 s in the vortex-free flow and 39.0, 42.0, and 38.0 s in the vortex flow (incomplete combustion on the substrate edges, prolonged local combustion). As is seen, the burning time in the vortex flow is less than that on the free surface by 10%. This can be explained by an increase in the burning rate due to the inflow of oxygen from the environment. Hence, air comes from the environment in the radial direction of the firestorm, and the burning mode in the firestorm is diffusive.

The necessary conditions of the physical similarity of a gas flow in the firestorm under laboratory and real conditions are identities of certain similarity criteria for

Table 1. Heat-flux densities

Experimental setup	Fuel	q, 10^5 W/m^2	Transducer coordinates, cm
Lower rotation	Oil	0.19	$x = 3$ $y = 8$
	Oil	2.4	$x = 0$ $y = 0.2$
	Large-scale fragments	0.34	$x = 3.5$ $y = 16.5$
	Small-scale fragments	1.91	$x = 0$ $y = 0.2$
Upper rotation	Oil	2.3	$x = 0$ $y = 0.2$
	Forest fuel	2.1	$x = 0$ $y = 0.2$
	Oil	2.0	$x = 0$ $y = 0.2$
Substrate in a horizontal air flow	Oil	2.0	$x = 0$ $y = 0.2$
	Forest fuel		$x = 0$ $y = 0.2$

the model and natural events:

$$\frac{V_* r_*}{t_*} = \mathrm{Sh} = \mathrm{idem}_1, \quad \mathrm{Gr} = \frac{1}{\nu}\left[\frac{g\beta(T_c - T_e)}{H_*^{-3}}\right] = \mathrm{idem}_2,$$
$$\frac{2r_*}{h_*} = \mathrm{idem}_3, \qquad (2)$$
$$\frac{m_1 s_2}{s_1 m_2} = 1 = \mathrm{idem}_4, \quad \mathrm{Fr} = \frac{\mu r_* V_*}{\rho \Gamma_*^2} = \mathrm{idem}_5.$$

Here, $V_* = \omega_* r_*$, where ω_* is the characteristic angular velocity of gas particles, is the characteristic linear velocity of their rotation; t_* is the characteristic time; g is the gravitational acceleration; β is the volumetric thermal expansion coefficient of the gas; T_c is the combustion temperature; T_e is the environmental temperature; idem means the identity of a similarity criterion for the model and natural events; r_* is the characteristic radius of the firestorm; μ and ρ are the absolute viscosity and the gas-phase density, respectively; H_* is the characteristic height of the firestorm; m is the mass of combustible materials in the natural event; s is the burning area; h is the flame height; the subscripts 1 and 2 correspond to the natural and model parameters, respectively; and q_1 and q_2 are the respective thermal effects of combustion.

Using data for the firestorms in Hamburg [1], we obtained Gr = 2.95 and 3.27 and Fr = 0.67 and 0.74 for the lower (substrate, base) and upper swirling, respectively. The closeness of these values indicates that, first, the formation of the firestorm is independent of the method of gas swirling and, second, the chosen parameters are similarity criteria for the problem under solution.

Analysis of the experimental results allows the following conclusions.

Table 2. Heat-flux density q in the firestorm from burning oil

m, g	τ_b, s	q, 10^5 W/m^2	A
18.3	278	1.9	0.67
31.7	473	2.4	0.70
32.0	406	2.3	0.65

Under laboratory conditions, firestorms were obtained by several independent methods. For all types of combustible substances, a firestorm turned out to consist of a combustion source, a convective column, and a mushroom-shaped cloud of gaseous and disperse combustion products. In addition, combustion in the firestorm was shown to be diffusive.

The characteristic attributes of the initiation of the firestorm are an abrupt increase in the flame height and the appearance of the spiral trajectories with a varying curvature radius along which heated combustion-product particles move over the fire source.

The formation of firestorms was shown to be independent of the method of their initiation and the type of combustible materials and to be determined by the heat-flux density, lift force, and angular momentum of the external vortex flow.

REFERENCES

1. G. F. Carrier, F. E. Fendell, and A. S. Feldman, Heat Transfer-Sov. Res. **107** (1), 16 (1985).
2. A. M. Grishin, *Mathematical Modeling of Forest Fires and New Methods of Fighting Them* (Nauka, Novosibirsk, 1992; Tomsk State Univ. Press, Tomsk, 1997).
3. *Intense Atmospheric Vortices*, Ed. by L. Bengtsson and S. Lighthill (Springer-Verlag, Heidelberg, 1982; Mir, Moscow, 1985).

Translated by V. Bukhanov

Doklady Physics, Vol. 49, No. 3, 2004, pp. 194–198. Translated from Doklady Akademii Nauk, Vol. 395, No. 3, 2004, pp. 343–347.

MECHANICS

Oscillatory Properties of the Frequencies and Shapes of the Natural Vibrations of Nonuniform Bars

L. D. Akulenko and S. V. Nesterov

Presented by Academician V.F. Zhuravlev November 4, 2003

Received November 6, 2003

A constructive numerical–analytical method is proposed for the analysis of free transverse vibrations of substantially nonuniform bars under various boundary conditions. To determine the frequencies and shapes of vibrations, an efficient procedure is developed for obtaining the eigenvalues and eigenfunctions of the corresponding self-adjoint fourth-order boundary value problems. New oscillatory properties are found, and statements equivalent to the oscillation theorem, Sturm comparison theorems, and their corollaries for second-order boundary value problems are formulated. The method is tested on model examples.

1. We analyze a bar with rigidly fastened ends (constraint). The self-adjoint boundary value problem for eigenvalues and eigenfunctions is described in terms of dimensionless variables by the relations [1–4]

$$(p(x)u'')'' = (\lambda r(x) - q(x))u, \quad 0 \le x \le l, \tag{1}$$

$$\begin{gathered} 0 < p^- \le p \le p^+ < \infty, \quad 0 < r^- \le r \le r^+ < \infty, \\ 0 \le q^- \le q \le q^+ < \infty; \\ u(0) = u'(0) = u(l) = u'(l) = 0. \end{gathered} \tag{2}$$

The unknown parameter $\lambda > 0$ and function $u(x)$ characterize the frequencies and shapes of the natural vibrations of the bar, respectively. The coefficient $p(x)$ is the bending stiffness, $r(x)$ is the linear density, and $q(x)$ is the external-medium elasticity. In contrast to the standard approaches, the bar length $l > 0$ is treated as a variable parameter when solving the problem specified by Eqs. (1) and (2).

It is necessary to find eigenvalues $\lambda = \lambda_n$ (frequencies $\omega_n = \sqrt{\lambda_n}$) and functions $u = u_n(x)$ (vibration shapes). The low vibration modes with $n = 1, 2, \ldots$ are of primary theoretical and applied interest. The boundary value problem specified by Eqs. (1) and (2) has a countable set of eigenvalues (discrete spectrum) and corresponding eigenfunctions (shapes) that form a basis orthonormal with the weight $r(x)$ [2, 3]:

$$\begin{gathered} \lambda \in \{\lambda_n\}, \quad 0 < \lambda_1 < \lambda_2 < \ldots < \lambda_n < \ldots, \quad \lambda_n \sim n^4, \\ u_n(x) = u(x, \lambda_n), \quad (u_n, u_m)_r = \|u_n\|_r^2 \delta_{nm}, \\ n, m = 1, 2, \ldots, \end{gathered} \tag{3}$$

where δ_{nm} is the Kronecker delta, $(\cdot, \cdot)_r$ is the scalar product, and $\|\cdot\|_r$ is the norm with the weight $r(x)$.

The problem specified by Eqs. (1) and (2) is formulated in terms of the isoperimetric variational problem [2, 3]

$$\begin{gathered} J[u] = \frac{1}{2}\int_0^l (p(x)u''^2 + q(x)u^2)dx \to \min, \\ I[u] = \|u\|_r^2 = \int_0^l r(x)u^2 dx = 1 \end{gathered} \tag{4}$$

in the presence of boundary conditions (2). Here, λ is the double Lagrange multiplier, λ_1 is the value corresponding to the (global) minimum of functional (4), and values $\lambda_2, \lambda_3, \ldots$ correspond to the local minima of the functional J under the orthogonality condition $(u, u_k)_r = 0$, $k = 1, 2, \ldots, n-1$.

The variational treatment is used to develop functional approaches for estimating the λ_n values and corresponding functions $u_n(x)$ [2, 3]. Computational algorithms make it possible to obtain effective upper bounds λ_n^+. It is considerably difficult to obtain lower bounds λ_n^- with high accuracy: the Weinstein–Aronszajn and Fichera's methods [2] are very algorithmically cumbersome and have low efficiency.

Institute for Problems in Mechanics,
Russian Academy of Sciences,
pr. Vernadskogo 101, Moscow, 119526 Russia
e-mail: kumak@ipmnet.ru

1028-3358/04/4903-0194$26.00

From Eqs. (2) and (4), it follows the rough two-sided bounds of eigenvalues:

$$\lambda_n^- \le \lambda_n \le \lambda_n^+, \quad \lambda_n^\pm = \left(\frac{\gamma_n}{l}\right)^4 \frac{p^\pm}{r^\mp} + \frac{q^\pm}{r^\mp},$$

$$\gamma_n = \arg(\cos\gamma\cosh\gamma - 1),$$
$$\gamma_1 = 4.7300, \quad \gamma_2 = 7.8532, \quad \gamma_3 = 10.9956, \ldots, \tag{5}$$
$$\gamma_n = \left(n + \frac{1}{2}\right)\pi + O(e^{-\pi n}), \quad n \gg 1.$$

Bounds $\lambda_n^\pm$ (5) are satisfactory if functions $p(x)$, $r(x)$, and $q(x)$ vary slightly. In this case, the solutions can be refined by the analytical perturbation method [5]. However, it is inefficient for numerical calculations. Bounds $\lambda_n^\pm$ (5) can be generally used to construct the initial approximation in recursive computational schemes (shooting method, successive approximations, fast-convergence methods, etc.) in combination with the procedures of continuation in the parameters of the system (parametric synthesis) or in the parameters artificially introduced for improving convergence [4]. The available methods and algorithms are insufficient for extensive routine calculations with high accuracy.

Equation (1) is inconvenient for numerical–analytical analysis. It is more natural to introduce the additional mechanical variables z and μ:

$$u' = \theta, \quad \theta' = -\frac{z}{p(x)}, \quad z' = \mu,$$
$$\mu' = -(\lambda r(x) - q(x))u;$$
$$u(0) = \theta(0) = u(l) = \theta(l) = 0, \tag{6}$$
$$u'' = -\frac{z}{p(x)}, \quad z'' = -(\lambda r(x) - q(x))u,$$

where z is the moment of the elastic forces and μ is the cutting force.

Besides the rigid attachment of ends specified by Eqs. (2) or (6), there are other conditions also leading to self-adjoint boundary value problems. Hinge attachment, i.e., $u = z = 0$; free ends, i.e., $z = \mu = 0$; and fixation of the tangent direction, i.e., $\theta = \mu = 0$, are among such conditions. The general form condition is elastic attachment with respect to the displacement and rotation of tangent at the bar ends:

$$[(1 - \kappa_x)\mu \mp \kappa_x u]_{x = 0, l} = 0,$$
$$[(1 - \sigma_x)z \mp \sigma_x\theta]_{x = 0, l} = 0, \quad 0 \le \kappa_{0, l}, \quad \sigma_{0, l} \le 1. \tag{7}$$

Normalized coefficients $\kappa_{0, l}$ and $\sigma_{0, l}$ in Eq. (7) determine the relative effect of the stiffness of the elastic attachment of the ends with respect to the displacement and rotation, respectively.

2. The eigenvalues and eigenfunctions of the problem specified by Eqs. (1) and (2) or Eqs. (6) and (7) are ordinarily found by constructing the general solution of the equations, which depends on the parameter λ, and satisfying the boundary conditions at $x = 0$ and l. The necessary and sufficient condition for the existence of a nontrivial solution is that the determinant of the fundamental-system matrix is equal to zero. This condition leads to the secular equation for the calculation of eigenvalues λ_n. According to general theory [2, 3], the determinant is an integer function of λ that admits a countable set of roots $\{\lambda_n\}$ in the real $\lambda > 0$ region, $\lambda_n \sim n^4$, and bounds are given by Eqs. (5).

The solution to the problem specified by Eqs. (6) is determined by the vector function $U = (u, \theta, z, \mu)$. It is necessary to construct two sets of solutions (λ is the parameter of the set) of the Cauchy problem for the following conditions at $x = 0$:

$$1)\ u(0) = \theta(0) = \mu(0) = 0, \quad z(0) = 1;$$
$$2)\ u(0) = \theta(0) = z(0) = 0, \quad \mu(0) = 1; \tag{8}$$
$$U = c_1U_1(x, \lambda) + c_2U_2(x, \lambda).$$

For the general boundary conditions given by Eqs. (7), it is necessary to construct four sets of solutions U_i:

$$1)\ u(0) = 1, \quad 2)\ \theta(0) = 1, \quad 3)\ z(0) = 1,$$
$$4)\ \mu(0) = 1; \quad U(x, \lambda) = \Sigma c_iU_i(x, \lambda). \tag{9}$$

The other components of the solution are set to zero [similarly to Eqs. (8)]. The summation in Eqs. (9) covers $i = 1$–4. The use of boundary conditions (7) leads to the following equations for λ and c_i:

$$(1 - \kappa_0)c_4 - \kappa_0c_1 = 0, \quad (1 - \sigma_0)c_3 - \sigma_0c_2 = 0,$$
$$\Sigma c_i[(1 - \kappa_l)\mu_i + \kappa_lu_i]_{x = l} = 0,$$
$$\Sigma c_i[(1 - \sigma_l)z_i + \sigma_l\theta_i]_{x = l} = 0.$$

3. The secular equation for the eigenvalues λ of problem (6) has the form

$$S(\lambda, l) = 0, \quad \lambda = \lambda_n(l),$$
$$S(\lambda, x) \equiv u_1(x, \lambda)\theta_2(x, \lambda) - u_2(x, \lambda)\theta_1(x, \lambda),$$
$$0 \le x \le l, \quad 0 < l < \infty, \quad \lambda > 0; \tag{10}$$
$$S(\lambda, x) > 0, \quad 0 < x \ll l, \quad \lambda \sim 1.$$

In the standard approaches, the parameter l is fixed ($l = 1$) and function S in Eqs. (10) is considered as dependent only on the unknown argument λ. Below, we report the methods and computational algorithms based on the introduced notion of the sagittary function $S(\lambda, x)$ of two arguments (the Latin word sagitta means arrow). The basic properties of the eigenvalues and eigenfunctions of the problem can be analyzed by using this function.

The secular equation and sagittary function for boundary conditions (7) are determined similarly to Eqs. (10):

$$\begin{gathered} S(\lambda, l) = 0, \quad \lambda = \lambda_n(l); \\ S(\lambda, x) \equiv \kappa_0(\sigma_0 d_{34} + (1-\sigma_0)d_{24}) \\ -(1-\kappa_0)(\sigma_0 d_{13} + (1-\sigma_0)d_{12}), \\ d_{ij} = d_{ij}(\lambda, x) = M_i Z_j - M_j Z_i, \\ M_i = (1-\kappa_l)\mu_i + \kappa_l u_i, \\ Z_i = (1-\sigma_l)z_i + \sigma_l \theta_i; \quad i, j = 1, \ldots, 4. \end{gathered} \tag{11}$$

Representation (11) for the sagittary function $S(\lambda, x)$ is considerably simplified by constructing two sets of the solutions

$$\begin{gathered} 1)\ u(0) = 1-\kappa_0, \quad \theta(0) = 0, \quad z(0) = 0, \\ \mu(0) = \kappa_0, \quad 0 < \kappa_0 < 1; \\ 2)\ u(0) = 0, \quad \theta(0) = 1-\sigma_0, \quad z(0) = \sigma_0, \\ \mu(0) = 0, \quad 0 < \sigma_0 < 1; \\ u = c_1 u_1 + c_2 u_2, \quad \theta = c_1\theta_1 + c_2\theta_2, \\ z = c_1 z_1 + c_2 z_2, \quad \mu = c_1\mu_1 + c_2\mu_2. \end{gathered} \tag{12}$$

Solution (12) with arbitrary λ, c_1, and c_2 automatically satisfies boundary condition (7) at $x = 0$. The secular equation and sagittary function have the form

$$\begin{gathered} S(\lambda, l) = 0, \quad \lambda = \lambda_n(l); \\ S(\lambda, x) \equiv ((1-\kappa_l)\mu_1(x, \lambda) + \kappa_l u_1(x, \lambda)) \\ \times ((1-\sigma_l)z_2(x, \lambda) + \sigma_l\theta_2(x, \lambda)) \\ -((1-\kappa_l)\mu_2(x, \lambda) + \kappa_l u_2(x, \lambda)) \\ \times ((1-\sigma_l)z_1(x, \lambda) + \sigma_l\theta_1(x, \lambda)). \end{gathered} \tag{13}$$

Any convenient form of a solution may be used in calculations. In particular, the construction of the fundamental system of solutions for the first case specified by Eqs. (9) is independent of the parameters κ_0 and σ_0, which are disregarded at the next stages of determining the sagittary function and secular equation according to Eqs. (11). In the second case specified by Eqs. (12), the linearly independent solutions are constructed with inclusion of κ_0 and σ_0. However, the number of integrable Cauchy problems is halved.

Thus, the sagittary function $S(\lambda, x)$ is considered below as known. It can be constructed either analytically (very rarely) or numerically by integrating Cauchy problems. In this case, it is necessary either to successively calculate the functions u_i, θ_i, z_i, and μ_i for fixed λ values with further storage or to jointly integrate (two or four) Cauchy problems and calculation of $S(\lambda, x)$ by finite formulas. The sagittary function S can be determined as the solution of the aforementioned set of Cauchy problems and nonlinear equation. For conditions (6), sagittary function S (10) satisfies the equation

$$\begin{gathered} S' = \frac{z_1 u_2 - z_2 u_1}{p(x)}, \quad S(\lambda, 0) \equiv 0, \quad 0 \le x \le l; \\ S(\lambda, x) = O(x^4), \quad S > 0, \quad 0 < x \ll l, \quad \lambda \sim 1. \end{gathered} \tag{14}$$

Relations obtained for the sagittary function under other boundary conditions indicated above are similar to Eqs. (14).

4. Analyzing the sagittary function $S(\lambda, x)$, one can determine the basic properties of the solution of the initial problem as well as formulate statements similar to the Sturm oscillation theorem and Sturm comparison theorems and their corollaries that have been previously obtained for second-order equations [2, 3, 7, 8].

Theorem 1. *For a fixed value $x = l > 0$, the sagittary function $S(\lambda, l)$ is an oscillating function of λ for $\lambda > 0$. For a sufficiently large value $\lambda = \lambda(l) > 0$, $S(\lambda, x)$ is an oscillating function of x in the range $0 \le x \le l$ and has an infinite number of zeros.*

For $\frac{r}{p} \ge c > 0$ and $x > 0$, the sagittary function $S(\lambda, x)$ is an oscillating function of x independently of $\lambda > 0$. This is also the case for $\frac{r}{p} \to 0$ and $x \to \infty$ if $\frac{r}{p} \sim x^{-\gamma}$, where $\gamma \le 4$. We note that both solutions $(u_1(x, \lambda), \theta_1(x, \lambda))$ and $(u_2(x, \lambda), \theta_2(x, \lambda))$ of the system specified by Eqs. (6) and (8) are not oscillating in the above sense.

For a fixed value $l > 0$, let a value $\lambda > 0$ exist such that $S(\lambda, l) = 0$ and the sagittary function $S(\lambda, x)$ has no intermediate zeros as a function of x. Then, the corresponding value $\lambda = \lambda_1(l)$ is the first eigenvalue of problem (6). If there are $n - 1 \ge 1$ intermediate zeros, $\lambda = \lambda_n(l)$ is the nth eigenvalue such that $0 < \lambda_1 < \lambda_2 < \ldots < \lambda_n$. Analyzing the properties of $S(\lambda, x)$, one arrives at statements useful for an approximate numerical solution.

Theorem 2. *Let the sagittary function $S(\lambda^*, x)$ have n intermediate zeros ($n = 1, 2, \ldots$) in the range $0 < x \le l$. Then, the sagittary function $S(\lambda^{**}, x)$, where $\lambda^{**} > \lambda^*$, has no fewer than n zeros in the same range.*

Moreover, the number of zeros in the given range $0 \le x \le l$ increases infinitely with an infinite increase in λ.

Theorem 3. *Let $S(\lambda^*, x) = 0$ for $x = x_1$ and x_2, where $0 \le x_1 < x_2 \le l$. Then, for a certain value $\lambda^{**} > \lambda^*$, there is a point x_3 such that $x_1 < x_3 < x_2$ and $S(\lambda^{**}, x_3) = 0$.*

The following statement concerning the position of the zeros of the sagittary function $S(\lambda, x)$ for $\lambda = \lambda^*$ and λ^{**} is constructive for determining the eigenvalues and eigenfunctions of problem (6).

Theorem 4. *Let x_0 be a common zero of the sagittary functions $S(\lambda^*, x)$ and $S(\lambda^{**}, x)$ and $\lambda^{**} > \lambda^*$. Then,*

the next zeros x_1 and x_2 of $S(\lambda^*, x)$ and $S(\lambda^{**}, x)$, respectively, satisfy the condition $x_2 < x_1$.

Therefore, all zeros $x_i > 0$ of the sagittary function $S(\lambda, x)$ are shifted to the left and right when λ increases and decreases, respectively. This property determining the local relation between the desired parameter λ and the interval length l can be used in calculations. It enables one to obtain upper λ_n^+ and lower λ_n^- bounds of eigenvalues λ_n, which is very important for determining the real accuracy of approximate solutions. In particular, there is the following theorem concerning the bounds $\lambda_1^\pm$ of the first eigenvalue $\lambda_1(l)$ and the corresponding zeros $x = \xi_1^\pm$ of the sagittary function $S(\lambda_1^\pm, x)$.

Theorem 5. *Let λ_1^+ be an upper bound of the first eigenvalue; i.e., $\lambda_1^+ \geq \lambda_1(l)$. Then, $S(\lambda_1^+, \xi^+) = 0$, where $\xi^+ \leq l$. Similarly, $S(\lambda_1^-, \xi^-) = 0$ for the lower bound $\lambda_1^- \leq \lambda_1(l)$, where $\xi^- \geq l$ [for $\xi^- > l$, the functions $p(x)$ and $r(x)$ are considered as smooth continuations to the interval (l, ξ^-)]. If $\lambda^\pm$ are close enough to each other, l and $\xi^\pm$ are also close to each other. In addition, $S(\lambda_1^+, l) < 0$ and $S(\lambda_1^-, l) > 0$.*

The property $S(\lambda_1^-, x) > 0$ for $0 < x < l$ follows from the simple estimates of the functions $u_{1,2}(x, \lambda_1^-)$ and $\theta_{1,2}(x, \lambda_1^-)$ according to Eqs. (8) and (14) [for problem (6)]. For $n \geq 2$, the sagittary function $S(\lambda_n^-, x)$ can naturally undergo up to $n-1$ changes of sign, whereas the sagittary function $S(\lambda_n^+, x)$ undergoes no fewer than n changes of sign. The general determination of the sign of the sagittary function S for $0 < x \ll l$ and its change for $0 < x < l$ requires cumbersome estimates. It is more convenient to obtain these estimates by numerically integrating the above Cauchy problems.

It is natural to use the "separating" property of the sagittary function S in computational methods associated with the iterative refinement of the desired solution including the shooting method, method of sequential approximations, Newton fast-convergence method, etc. This is why we call the function S a sagittary function.

5. First, we illustrate theory by a model example [4] that allows the analytical integration of Eq. (1). Let the ends of the bar be fastened [conditions (2)], $q \equiv 0$, and

$$p(x) = p_0(b + ax)^2, \quad r(x) = r_0(b + ax)^{-2}, \quad b + ax \neq 0. \tag{15}$$

We arrive at the Euler equation [4, 7, 8] whose solution is sought in the form of a power function $(b + ax)^k$, where k is the complex parameter determined from the algebraic equation $k^2(k-1)^2 = \frac{\lambda}{a^4}$, which is solvable in radicals. The general solution has an unwieldy form and is expressed in terms of power, trigonometric, and logarithmic functions. It is difficult to determine the roots of secular equation (10), but they can be obtained numerically.

Without loss of generality, two of the three parameters a, b, and l, as well as constants p_0 and r_0 in Eqs. (15), can be set to unity. For definiteness, we assume that $ab > 0$. In this case, we can set $a = b = 1$ and $l > 0$. Solution (8) for $\lambda > \frac{1}{16}$ ($u \equiv 0$ for $\lambda \leq \frac{1}{16}$) takes the form

$$u = c_1u_1 + c_2u_2 = \sqrt{1+x}(c_1w_1(x, \lambda) + c_2w_2(x, \lambda)),$$
$$\theta = u',$$
$$w_1 = \sin(f^-h) - \frac{f^-}{f^+}\sinh(f^+h), \quad h = \ln(1+x), \tag{16}$$
$$0 \leq x \leq l,$$
$$w_2 = \cos(f^-h) - \cosh(f^+h), \quad f^\pm = \left(\sqrt{\lambda} \pm \frac{1}{4}\right)^{1/2}.$$

The hyperbolic functions are reduced to the power functions $(1+x)^{\pm f^\pm}$. Formulas (16) show that the functions $u_{1,2}$ and $\theta_{1,2}$ are not oscillating. However, the sagittary function $S(\lambda, x)$ is an oscillating function of both x and λ. Indeed,

$$S(\lambda, x) = 2f^-\left(\cos(f^-h)\cosh(f^+h) - \frac{1}{4}(f^+f^-)^{-1} \times \sin(f^-h)\sinh(f^+h) - 1\right). \tag{17}$$

The secular equation for any $x = l > 0$ admits the countable set of roots $\lambda_n(l)$, which can be found numerically. In particular, for $l = 1$, the "exact" λ_1 value and bounds λ_n have the form

$$\lambda_1 = 2181.355,$$
$$\sqrt{\lambda_n} = \left(\frac{\pi}{\ln 2}\right)^2\left(n + \frac{1}{2}\right)^2 - \frac{1}{4} + O\left(\frac{1}{n}\right), \quad n \gg 1. \tag{18}$$

Then, we calculate λ_1 by the shooting numerical algorithm. The two-coordinate (trigonometric) approximation according to the Rayleigh–Ritz method provides an upper bound of $\lambda_1^+ = 2338.442$, which differs significantly from the exact value given in Eqs. (18). The sagittary function method based on Theorem 5 provides the abscissa $\xi^+ = 0.9770$. Using this value, we obtain the lower bound $\lambda^- = (\xi^+)^4\lambda^+ = 2131.2312$ according to the previously described approach [4].

Seven shooting-method iterations provide the bounds (with a relative accuracy of 10^{-5})

$$\lambda_1^+ = 2181.4093, \quad \lambda_1^- = 2181.3478,$$
$$\lambda_1 = 2181.3785,$$

which is very close to the exact λ_1 value given in Eqs. (18). Approximate expressions for λ_n with $n \geq 2$ and for other $l > 0$ are similarly calculated with the necessary accuracy.

For the hinge attachment of the bar ends ($u = z = 0$ at $x = 0, 1$), we similarly obtain the bounds

$$\lambda_1^+ = 432.3410, \quad \lambda_1^- = 432.2820, \quad \lambda_1 = 432.3150,$$
$$\frac{\Delta\lambda_1}{\lambda_1} \sim 10^{-4}.$$

The above model example illustrates the basic theoretical statements. Moreover, it is shown that numerical methods are required even in the cases of analytical integrability (usually in terms of special functions). Thus, the numerical–analytical method based on the sagittary function is preferable.

To compare different approaches under the condition of the hinge attachment, we consider Eq. (1) with $p(x) = 1 + 2\sin^2\pi x$ and $r(x) = 1$. This problem was solved approximately with the Weinstein–Aronszajn method [2] for $n = 1$ and 3. The values $\lambda_1 = 2.36388\pi^4$ and $\lambda_3 = 149.6520\pi^4$ were obtained with a relative accuracy of $\frac{\Delta\lambda}{\lambda} \sim 10^{-6}$. Several iterations in the sagittary-function algorithm provides the bounds

$$2.36387\pi^4 \leq \lambda_1 \leq 2.36389\pi^4,$$
$$149.6517\pi^4 \leq \lambda_3 \leq 149.6531\pi^4.$$

The sagittary-function method provides the bounds $29.671\pi^4 \leq \lambda_2 \leq 29.689\pi^4$ for the value λ_2 missing in [2].

We emphasize that the Weinstein–Aronszajn method is very cumbersome and complicated for efficient calculations. The above calculations show that the sagittary-function method has substantial advantages for the above class of the problems for eigenvalues and functions that is described by fourth-order ordinary differential equations.

ACKNOWLEDGMENTS

This work was supported by the Russian Foundation for Basic Research, project nos. 02-01-00252 and 02-01-00157.

REFERENCES

1. S. P. Timoshenko, *Vibration Problems in Engineering* (Nauka, Moscow, 1967; Nostrand, Toronto, 1959).
2. S. Gould, *Variational Methods for Eigenvalue Problems* (Oxford Univ. Press, Oxford, 1966; Mir, Moscow, 1970).
3. L. Collatz, *Eigenwertaufgaben mit Technischen Anwendungen* (Akad. Verlag, Leipzig, 1963; Nauka, Moscow, 1968).
4. L. D. Akulenko, G. V. Kostin, and S. V. Nesterov, Izv. Akad. Nauk, Mekh. Tverd. Tela, No. 5, 180 (1995).
5. L. D. Akulenko and G. V. Kostin, Prikl. Mat. Mekh. **56**, 452 (1992).
6. Yu. A. Mitropol'skii and B. I. Moseenkov, *Asymptotic Solutions of Partial Differential Equations* (Vishcha Shkola, Kiev, 1976).
7. Ph. Hartman, *Ordinary Differential Equations* (Wiley, New York, 1964; Mir, Moscow, 1970).
8. E. Kamke, *Differentionalgleichungen Lösungsmethoden und Lösungen (Handbook of Ordinary Differential Equations)* (Geest and Portig, Leipzig, 1959; Nauka, Moscow, 1971).

Translated by R. Tyapaev

Doklady Physics, Vol. 49, No. 3, 2004, pp. 199–203. Translated from Doklady Akademii Nauk, Vol. 395, No. 3, 2004, pp. 348–352.

MECHANICS

Cumulative Effect Accompanying Large Deformations of a Shell under One-Sided Pressure

A. N. Golubyatnikov*, S. I. Zonenko, and Academician G. G. Chernyĭ****

Received December 19, 2003

The behavior of a perturbed flat layer of a deformable material under pressure difference is associated with the Rayleigh–Taylor instability (see, e.g., [1]). As was shown in [2], the development of instability can lead to the formation of regular fingerlike structures, where the energy and momentum of a thrown layer are cumulated. This effect can be studied separately as well as provide a number of applications. It is somewhat similar to the appearance or special creation of a cumulative jet when throwing a thin layer with the shape of an angle or cone and in other more complicated cases [3].

A model of a thin dust shell which is free of internal stresses, is subjected to one-sided pressure, and whose particles undergo inelastic collisions in the case of self-intersections was used in [2] to effectively describe cumulation. In this work, this model is used to construct two exact solutions of the throwing problem that concern the optimization of focusing the shell to one moving material point or, in the flat case, rod. A number of general properties of the equations of motion of the shell, as well as the method for constructing the solution of the Cauchy problem with zero initial velocity, are discussed. Two sufficiently wide classes of exact solutions allowing the separation of variables are presented.

EQUATIONS OF MOTION OF THE DUST SHELL

A model of a material surface that is free of stresses and moves under a given pressure p_0 applied to one side (pressure to the other side is negligibly low) is the simplest model for describing the motion of a thin plate or shell thrown by a strong explosion [2]. An exact hydrodynamic solution of the one-dimensional problem of the acceleration of a flat piston by one-sided pressure from an initially stationary uniform gas was found by Hugoniót. According to this solution, for one to consider p_0 as constant neglecting an expansion wave formed in the gas, it is necessary to satisfy the inequality $2c_0 \gg (\gamma - 1)v_n$, where c_0 is the speed of sound in the stationary gas, γ is the adiabatic index, and v_n is the normal component of the shell velocity. Thus, pressure p_0 can be considered as constant at least at the initial stage of motion.

The equations of motion of the shell consisting of noninteracting material particles have the form

$$\sigma \mathbf{r}_{tt} = p_0 \mathbf{n}, \tag{1}$$

where σ is the surface density of the shell, $\mathbf{r}$ is the radius vector of shell particles with the Eulerian components x^i, and $\mathbf{n}$ is the unit normal vector directed along the pressure. The subscript t denotes the time derivative for constant Lagrangian coordinates ξ^α, α = 1 and 2.

Let $a_{\alpha\beta}$ be components of the metric tensor of the shell surface,

$$a_{\alpha\beta} = \delta_{ij} x^i_\alpha x^j_\beta, \text{ and } x^i_\alpha = \frac{\partial x^i}{\partial \xi^\alpha} \tag{2}$$

be the components of the vectors tangential to the surface $\mathbf{r}_\alpha$ such that $\mathbf{n} = \dfrac{\mathbf{r}_1 \times \mathbf{r}_2}{|\mathbf{r}_1 \times \mathbf{r}_2|}$, where $|\mathbf{r}_1 \times \mathbf{r}_2| = \sqrt{\det a_{\alpha b}} \equiv \sqrt{a}$. In view of the mass conservation law, we have the Lagrange formula

$$\sigma = \sigma_0 \sqrt{\frac{a_0}{a}}. \tag{3}$$

Zero means the initial quantities—functions ξ^α. Using Eqs. (1) and (3), we arrive at the vector equation

$$\sigma_0 \sqrt{a_0} \mathbf{r}_{tt} = p_0 \mathbf{r}_1 \times \mathbf{r}_2. \tag{4}$$

One of the Lagrangian coordinates can always be taken so that $\sigma_0 \sqrt{a_0} = p_0$; i.e., the "mass variable" m =

* *Faculty of Mechanics and Mathematics, Moscow State University, Vorob'evy gory, Moscow, 119992 Russia*

** *Institute of Mechanics, Moscow State University, Michurinskiĭ pr. 1, Moscow, 119192 Russia*

1028-3358/04/4903-0199$26.00 © 2004 MAIK "Nauka/Interperiodica"

$\frac{1}{p_0}\int \sigma_0\sqrt{a_0}\,d\xi^1$ can be used. This manipulation transforms system (4) to the homogeneous form. If motion of the shell is flat (in this case, $x^3 = \xi^2$), system (4) is linear and reduced to the homogeneous form by using the mass variable [2].

Equation (4) can be obtained from the holonomic variational equation with the Lagrangian

$$\Lambda = \sigma_0\sqrt{a_0}\frac{|\mathbf{r}_t|^2}{2} + \frac{p_0}{3}\mathbf{r}\cdot(\mathbf{r}_1\times\mathbf{r}_2), \tag{5}$$

by varying the law of motion $x^i(\xi^\alpha, t)$. Starting from this formulation, one can develop approximate numerical methods for solving problems and deriving conservation laws.

Contracting Eq. (4) with $\mathbf{r}_\alpha$, we obtain the relations

$$x^i_{tt}x_{i,\alpha} \equiv (x^i_t x_{i,\alpha})_t - \left(\frac{|\mathbf{r}_t|^2}{2}\right)_\alpha = 0, \tag{6}$$

which lead to the conservation law for vorticity of the tangential velocity (for general theory, see [4]). Indeed, taking the exterior derivative with respect to ξ^β, we arrive at the relation

$$(x^i_{t,1}x_{i,2} - x^i_{t,2}x_{i,1})_t = 0. \tag{7}$$

In particular, if the initial velocity of the shell is equal to zero, the tangential velocity component is potential in further motion.

Contracting Eq. (4) with $\mathbf{r}_t$, we obtain the following equation for the kinetic energy of the shell:

$$\left(\sigma_0\sqrt{a_0}\frac{|\mathbf{r}_t|^2}{2} - \frac{p_0}{3}\mathbf{r}\cdot(\mathbf{r}_1\times\mathbf{r}_2)\right)_t - \frac{p_0}{3}[(\mathbf{r}\cdot(\mathbf{r}_t\times\mathbf{r}_1))_2 - (\mathbf{r}\cdot(\mathbf{r}_t\times\mathbf{r}_2))_1] = 0. \tag{8}$$

Similarly, Eq. (4) for the angular momentum can also be represented in divergence form.

For the shell with an edge, to prevent the possibility of leaking to the leading surface of the shell and thereby to exclude the necessity of analyzing hydrodynamic processes accompanying such a leakage, the shell must be considered as placed into a channel of the corresponding shape, i.e., as a deformable piston.

The model of perfectly inelastic collisions is used to describe the intersections of the trajectories of shell particles. This model corresponds to the summation of the momenta of colliding material points. In this case, new surfaces, as well as compact elements such as rods or balls, can be formed depending on the geometry of collisions.

FOCUSING TO A POINT

We discuss the problem of focusing of an initially stationary uniform spherical segment with mass M to a point by constant external pressure p_0. In this case, Eq. (4) yields the equation

$$\ddot{r} = -\frac{p_0 r^2}{\sigma_0 r_0^2}, \quad \sigma = \frac{\sigma_0 t_0^2}{r^2} \tag{9}$$

for the sphere radius $r(t)$ with the initial conditions $\dot{r}(0) = 0$ and $r(0) = r_0$, where r_0 and σ_0 are the initial radius and density of the shell, respectively.

Equation (9) has the energy integral

$$\frac{\dot{r}^2}{2} + \frac{p_0}{3\sigma_0 r_0^2}(r^3 - r_0^3) = 0, \tag{10}$$

which can be used to represent the solution in the quadrature $t(r)$. Moreover, this integral enables one to determine the final radial velocity of the shell particles at $r = 0$ in the form

$$\dot{r}_* = -\left(\frac{2p_0 r_0}{3\sigma_0}\right)^{1/2}. \tag{11}$$

The collapse time is determined by the expression

$$t_* = \left(\frac{3\sigma_0 r_0}{2p_0}\right)^{1/2}\int_0^1 \frac{d\rho}{\sqrt{1-\rho^3}} \approx 1.717\left(\frac{\sigma_0 r_0}{p_0}\right)^{1/2}. \tag{12}$$

Then, according to the model of perfectly inelastic collisions, one material point of mass M moves rectilinearly with constant velocity, because the pressure force is absent due to the zero area of the layer surface. The initial area of the segment is equal to $S_0 = 4\pi r_0^2\sin^2\left(\frac{\theta_0}{2}\right) = \frac{M}{\sigma_0}$, where θ_0 is the half-angle of the segment. Due to the axial symmetry, the total momentum is determined by the axial velocity component $\dot{r}_*\cos\theta$ of moving material points, where θ is the angle between the symmetry axis and radius vector of a given particle of the shell. The absolute value of the momentum is given by the expression

$$P = \pi\sin^2\theta_0\left(\frac{2p_0 r_0^5\sigma_0}{3}\right)^{1/2} = \pi\frac{\sin^2\theta_0}{\sin(\theta_0/2)}\left(\frac{p_0 r_0^3 M}{6\pi}\right)^{1/2}. \tag{13}$$

For the angle $\theta_0 = 70°32'$ corresponding to $\cos\theta_0 = \frac{1}{3}$, final momentum (13) of the material point formed from the shell with a given mass has the maximum value

$$\max P = \frac{4}{9}\sqrt{2\pi p_0 r_0^3 M}. \quad (14)$$

It is of interest to calculate the efficiency η associated with energy expense. It is defined as

$$\eta = \frac{P^2}{2MA}, \quad (15)$$

where $A = p_0 V$ is the work done by the pressure forces and V is the volume covered by the shell. Using Eq. (13), we obtain $\eta = \cos^4\frac{\theta_0}{2}$. For the optimum angle, $\eta = \frac{4}{9} \approx 0.444$.

The solution of Eq. (9) that is locally spherically symmetric can be used as a test for the development of various approximation methods.

For a similar problem of transverse compression of a homogeneous dust shell in the form of a cylinder segment with radius r_0 and half-angle θ_0, the law of motion of shell particles has the form

$$r = r_0\cos\left(t\sqrt{\frac{p_0}{\sigma_0 r_0}}\right),$$

$$t \in [0; t_*], \quad t_* = \frac{\pi}{2}\left(\frac{\sigma_0 r_0}{p_0}\right)^{1/2};$$

and the total momentum per unit length of the cylinder generator is given by the expression

$$P = 2\sqrt{p_0\sigma_0 r_0^3}\sin\theta_0 = \sqrt{2p_0 r_0^2 M}\frac{\sin\theta_0}{\sqrt{\theta_0}},$$

where $M = 2r_0\theta_0\sigma_0$ is the mass per unit length. The density is determined as $\sigma = \sigma_0\frac{r_0}{r}$.

The formulation of the optimum problem leads to the transcendental equation $2\theta_0 = \tan\theta_0$, whose solution is $\theta_0 = 66°47'$ and, correspondingly,

$$\max P = 0.852\sqrt{2p_0 r_0^2 M}.$$

At $t = t_*$, a rod (filament) is formed and moves with velocity $\frac{P}{M}$ direction perpendicular to its length in the symmetry plane. The efficiency for the compression of the cylinder segment is equal to $\eta = \frac{\sin^2\theta_0}{\theta_0^2}$. For the optimum angle, $\eta = 0.623$.

CONSTRUCTION OF THE GENERAL SOLUTION

Let us seek the solution of the Cauchy problem for Eq. (4) with zero initial velocity $\mathbf{r}_t = 0$ and given initial radius vector $\mathbf{r}_0(\xi^\alpha)$ in the form of the Taylor series in time t. Since Eq. (4) involves only even-order time derivatives and the initial condition has the above form, the solution of this problem is expressed in terms of t^2 powers. Thus,

$$\mathbf{r} = \sum_{n=0}^{\infty}\mathbf{R}_n(\xi^\alpha)t^{2n}. \quad (16)$$

Using a mass variable, e.g., ξ^1, for the determination of coefficients $\mathbf{R}_n$, we arrive at the recurrence relations

$$2n(2n-1)\mathbf{R}_n = \sum_{k=0}^{n-1}\mathbf{R}_{k,1}\times\mathbf{R}_{n-1-k,2}. \quad (17)$$

Using Eq. (17), one can easily calculate any term of the Taylor series by differentiating the initial conditions with respect to the Lagrangian variables ξ^1 and ξ^2. We estimate the convergence rate of this series by making all its variables dimensionless.

Let all derivatives of $\mathbf{r}_0$ be limited by one constant $C = 1$. Then, it is easy to show that the coefficients of the first terms of the series (beginning with $\mathbf{R}_1$) do not exceed the respective numbers

$$\frac{1}{2}, \quad \frac{1}{2^2\cdot 3} < \frac{1}{2^3}, \quad \frac{1}{2^3\cdot 3^2} < \frac{1}{2^6}, \quad \frac{1}{2^3\cdot 3^2\cdot 7} < \frac{1}{2^8}, \quad \frac{5}{2^5\cdot 3^4\cdot 7} < \frac{1}{2^{11}}, \quad \frac{1}{2\cdot 3^5\cdot 7\cdot 11} < \frac{1}{2^{15}}. \quad (18)$$

Beginning with $n = 3$, these numbers do not exceed $\frac{1}{2^{2n}}$. Then, applying the principle of mathematical induction, we assume that $|\mathbf{R}_{n-1}| < \frac{1}{2^{2(n-1)}}$ for $n > 6$. Using Eqs. (17) and (18), we arrive at the estimate

$$|\mathbf{R}_n| < (n\cdot 2^{2n})^{-1}, \quad (19)$$

which is even stronger than the initial estimate (it is valid beginning with $n = 6$). Thus, estimate (19) can characterize the convergence rate of series (16) for a

fixed value of t. In this case, series (16) converges absolutely better than a geometric sequence with the denominator $\left(\frac{t}{2}\right)^2$, which is sufficient for at least the local existence of the solution for $t < 2$.

An example of the expansion of the spherical shell shows that it is generally impossible to substantially improve time t for which series (16) converges. When the shell expands, the derivatives of the function $r(t)$ entering into Eq. (9) and integral (10) change their signs. In this case, the solution tends to infinity with the asymptotic behavior $(t - t_\infty)^{-2}$, where

$$t_\infty = \left(\frac{3\sigma_0 r_0}{2p_0}\right)^{1/2}\int_1^\infty \frac{d\rho}{\sqrt{\rho^3 - 1}} \approx 3.013\left(\frac{\sigma_0 r_0}{p_0}\right)^{1/2}.$$

We emphasize that the convergence of special classes of solutions may be much better. In particular, series (16) for plane motion converges as $\frac{t^{2n}}{(2n)!}$ (see solutions in [2]).

In addition, we consider series (17) for the spherical-shell compression specified by Eq. (9). In this case,

$$\frac{r}{r_0} = 1 - \frac{\tau^2}{2} + \frac{\tau^4}{12} - \frac{\tau^6}{144} + \frac{\tau^8}{576} - \frac{\tau^{10}}{5184} + \ldots, \qquad (20)$$

where $\tau = \left(\frac{p_0}{\sigma_0 r_0}\right)^{1/2} t$ is the dimensionless time. It is clear that series (20) is inconvenient for determining the focusing time t_* when $r = 0$. To this end, we propose a method for constructing a polynomial approximating the solution in the segment $[0, t_*]$. Its minor and major terms are determined by the asymptotic behaviors for $t \to 0$ and $t \to t_*$, respectively. We note that derivatives $r^{(n)}$ of all orders $n = 2, 3, 5, 6, 7, 9, \ldots$, along with r, vanish at $t = t_*$.

We consider only the sixth-order polynomial

$$\frac{r}{r_0} \approx 1 - \frac{\tau^2}{2} + C_1\tau^4 + C_2\tau^6.$$

The relations $r = r^{(2)} = r^{(3)} = 0$ determine the constants $C_1 = \frac{1}{6}$, $C_2 = -\frac{11}{900}$, and $\tau_* = \sqrt{\frac{30}{11}} \approx 1.651$, which differs by less than 4% from the exact value $\tau_* = 1.717$ (12).

This method can be applied in the general case if the thrown shell is initially smooth. Focusing begins when the equality $\mathbf{r}_1 \times \mathbf{r}_2 = 0$ is reached.

We also note that the solution is simplest if the normal coordinates y^i related to the initial position of the shell as $x^i = x_0^i(y^\alpha) + n_0^i(y^\alpha)y^3$, where x^i are the Cartesian coordinates, are used as the Eulerian coordinates. In this case, the time dependence of the coordinates y^3 and y^α begins with t^2 and t^4, respectively.

SPECIAL CLASSES OF SOLUTIONS

We present two sufficiently wide classes of solutions of Eq. (4) that allow the separation of the Lagrangian variables and time as well as describe fundamentally three-dimensional flows. We leave aside a detailed analysis of the general solution of flat (linear) and axisymmetric problems. Let us use the mass variable.

The first class of solutions has the form

$$x^i = A^i_{\alpha\beta}(t)\xi^\alpha\xi^\beta + B^i_\alpha(t)\xi^\alpha + C^i(t).$$

These solutions are not invariant under group transformations, but they belong to certain tensor representations of the SL_2 group of linear transformations of variables ξ^α conserving area. From this viewpoint, the class of flows of an ideal fluid, where velocity depends linearly on the radius vector, is similar [5, 6]. The coefficients of polynomials (21) satisfy the systems of equations

$$\ddot{A}^i_{\alpha\beta} = 2\epsilon^i_{jk}(A^j_{\alpha1}A^k_{\beta2} + A^j_{\beta1}A^k_{\alpha2}),$$

$$\ddot{B}^i_\alpha = 2\epsilon^i_{jk}(A^j_{\alpha1}B^k_2 + B^j_1A^k_{\alpha2}), \quad \ddot{C}^i = \epsilon^i_{jk}B^j_1B^k_2.$$

The second class, which obviously overlaps with the first class, consists of solutions in the form

$$x^i = A^i_p(t)x^p_0(\xi^\alpha) + B^i(t),$$

which are generalized the aforementioned solutions with uniform deformation [5, 6]. In particular, this class includes spherically symmetric solution (9) having the ball matrix A. Substitution into Eq. (4) yields

$$\mathbf{M}\cdot\mathbf{r}_0 + \mathbf{N} = \mathbf{r}_{0,1}\times\mathbf{r}_{0,2}, \quad M_{pq} = \frac{\delta_{ij}A^i_p\ddot{A}^j_q}{|A|},$$

$$N_p = \frac{\delta_{ij}A^i_p\ddot{B}^j}{|A|},$$

where $|A| = \det(A^j_p)$. In this case, one must deal more carefully with the separation of variables taking into

account the functional dependence of the variables $x_0^p(\xi^\alpha)$.

ACKNOWLEDGMENTS

This work was supported by the Council of the President of the Russian Federation for Support of Young Russian Scientists and Leading Scientific Schools (project nos. MK-1904.2003.01, NSh-1481.2003.1, NSh-1635.2003.1) and the Russian Foundation for Basic Research (project no. 02-01-00109).

REFERENCES

1. D. Joseph, *Stability of Fluid Motions* (Springer, New York, 1976; Mir, Moscow, 1982).
2. S. I. Zonenko and G. G. Chernyĭ, Dokl. Akad. Nauk **390**, 46 (2003) [Dokl. Phys. **48**, 239 (2003)].
3. M. A. Lavrent'ev and B. V. Shabat, *Problems of Hydrodynamics and Their Mathematical Models* (Nauka, Moscow, 1973) [in Russian].
4. A. N. Golubyatnikov, Aéromekh. Gaz. Din., No. 4, 14 (2002).
5. L. I. Sedov, *Similarity and Dimensional Methods in Mechanics*, 10th ed. (Nauka, Moscow, 1987; Academic, New York, 1959).
6. L. V. Ovsyannikov, Dokl. Akad. Nauk SSSR **111**, 47 (1956).

Translated by R. Tyapaev